Low-temperature characterization of dielectric loss at microwave frequencies in aluminum oxide

by

Martin R. Otto

A thesis
presented to the University of Waterloo
in fulfillment of the
thesis requirement for the degree of
Master of Science
in
Physics - Nanotechnology

Waterloo, Ontario, Canada, 2015

I hereby declare that I am the sole author of this thesis. This is a true copy of the thesis, including any required final revisions, as accepted by my examiners.

I understand that my thesis may be made electronically available to the public.

Abstract

Superconducting quantum devices have gained increasing interest over the past 15 years because of their role as promising candidates for implementing a large-scale quantum computer and as ultra-sensitive detectors. Superconducting resonators are one type of superconducting device which are used in a variety of applications including quantum computing and radioastronomy. They can achieve large quality factors which are important for these applications and a variety of others. Specific examples of these applications include the readout and coupling of superconducting qubits and also microwave kinetic inductance detector arrays for sub-mm wavelength astronomical measurements. High quality factors also enable the study of very subtle features in the electromagnetic response of the resonator. This feature in turn offers provides a method to characterize loss mechanisms which affect the performance of superconducting qubits, by measuring the quality factor of a resonator. Dielectric loss is an example of such a loss mechanism, and is considered to be one of, if not *the* major obstacle to overcome in order to construct scalable quantum technologies based on superconducting devices. This type of loss arises from the coupling of the electric field in the device to spurious degrees of freedom which arise naturally the dielectric environment of the device. The fast-growing interest in the physics and applications of superconducting resonators has renewed interest in an improving our fundamental understanding of dielectric loss. This interest involves the study of a much bigger and older question in condensed matter physics; namely, what is the microscopic physics which governs the behaviour and of an amorphous material at low-temperatures?

In this thesis, we present a systematic study of dielectric loss in amorphous aluminum oxide using superconducting microwave resonators. Measurements of the intrinsic loss tangent over a large temperature range of 40 mK to 1 K are presented and analyzed in detail. Some aspects of the data are well understood in terms of the standard tunnelling two-level system model, while others require a deeper analysis of the electrodynamics of the resonator and insights from more advanced theories. We employ a consistent approach using numerical simulations of the resonator to understand loss mechanisms arising from both an inhomogeneous electric field and multiple dielectric layers. We measure saturation effects which provide insight into coherent properties of two-level system ensembles and the mutual interaction between them. Excellent agreement with the two-level system model is found for intrinsic losses, however the strong dependence on temperature which we observe for saturation effects is not predicted in the standard form of the model. We find that this dependence can be understood in terms of the theory of spectral diffusion

which is consistent with a strong mutual interaction between two-level systems contributes to broadening of their spectral linewidths.

Acknowledgements

I started working as a graduate student in the superconducting quantum devices group at the Institute for Quantum Computing in the January 2013. During my time, I could not have hoped for a more complete and transformative research experience. I quickly came to appreciate that a passion for detail and a willingness to continually refine ones view of nature are the foundations of a sound scientific method. My view of science changed from one consisting not simply of a repository of known truths, but a network of ideas, possibilities and facts established by an honest eye and scrutiny.

It is essential to acknowledge the guidance and support which was always available to me during my graduate studies at the University of Waterloo. The entire superconducting quantum devices group and its teamwork-based scientific policy maximized my learning environment. The ever-present council from my supervisor, friend and mentor Dr. Adrian Lupascu, helped me immensely in furthering my research during both the rewarding and challenging experiences. A special acknowledgement to Ph.D student Chunqing Deng, who worked extensively with me on related projects and the work presented in chapters 3, 4 and 6. Jean-Luc Orgiazzi, you were always available to share knowledge and experiences in microwave simulation, low-temperature techniques and nano-fabrication. Your assistance and patience provided me with a solid foundation for much of the work presented in this thesis. Former post-doctoral fellows, Florian Ong and Mustafa Bal, never once refused to assist me in even the most basic endeavours in fabrication, low-temperature methods and device design. Post-doctoral fellow Pol Forn-Diaz, your strong belief in kinship among scientists taught me that a productive work environment extends beyond the laboratory and the details of ones research.

I am truly fortunate to have had such a gratifying and educational experience in the superconducting quantum devices group. My time at the University of Waterloo equipped me with a clear outlook and broad skill-set upon which I called in deciding how to move forward in life, both personally and academically. I reflect upon my experiences with a true sense of fulfillment and renewed subscription to a philosophy in which hard work is the guarantor of accomplishment.

Dedication

This thesis is dedicated to my parents, Patrick and Jennifer, and my partner Alison for their enduring love and support.

Table of Contents

List of Tables

List of Figures

Chapter 1

Introduction

The discovery of superconductivity in 1911 by Heike Kammerlingh Onnes is among the most important events in the history of physics. An explanation of the mechanism of superconductivity was a monumental theoretical challenge, and it was not until nearly fifty years later that a microscopic quantum mechanical theory was developed by Bardeen, Cooper and Schrieffer [6]. This time interval alone warrants perspective. Historians unanimously refer to the 20th century as one which demonstrated rapid scientific, technological and social progress. In 1911 the Titanic sank, telecommunications was embryonic and the Universe was thought to consist of a single galaxy. In 1957, nuclear power was emerging, medical science was thriving, and transistors were becoming mainstream technology. Despite the rapid global progress of humanity, the task of understanding superconductivity proved to be simply *enormous.* It took the full arsenal of quantum mechanics and the work of some of the greatest physicists of the era to explain how electrons become attracted to each other at sufficiently low temperatures and coalesce into a state which exhibits zero DC resistance. It is important not to exclude the contributions made towards phenomenological descriptions from Landau [46], London [51] and others in describing some of the macroscopic features of superconductivity, but it was clear a microscopic theory was needed to provide a complete account of superconductivity. Once this understanding was established, however, superconductivity started to pay dividends. This thesis is an account of one of them.

1.1 Superconducting quantum devices

In the second half of the 20th century, superconductors were integrated into electronic devices which harnessed their unique quantum properties. Most of the devices were implemented as sensors and detectors, the most well known of which is the superconducting quantum interference device (SQUID) [38]. The operation of a SQUID relies on the unique properties of a *Josephson junction*, a discontinuity in the superconductor across which pairs of electrons may tunnel without dissipation [41]. These properties include the interference between the phases of the superconducting wavefunction. By taking advantage of this effect, SQUID devices provided new ways to detect very small magnetic signals and are among the most sensitive magnetic detectors ever produced. Further studies using SQUIDs fabricated from different materials led to improvements in our understanding of the physical mechanism which binds electrons together and produces superconductivity. This led to advances in the field of material science, driven by the prospect of realizing a room temperature superconductor. Over the years, the quantum properties of SQUIDs were applied to create devices possessing distinct, addressable quantum states which can be used as processors for quantum information. These devices, now referred to as superconducting qubits, are at the forefront of modern quantum technologies [20].

1.1.1 Superconducting microwave resonators

Superconducting microwave resonators are popular micro-fabricated circuits which have been used since the 1960's and offer a wide range of applications [88]. The versatility and wide-range of applications of these devices have refined them into reliable scientific tools for probing a variety of physical phenomena. The most appealing feature of superconducting resonators is undoubtedly their ability to achieve very high quality factors. They differ from normal microwave resonators only in the sense that they are obviously made of a superconductor, and thus operate at cryogenic temperatures. A normal metal has conduction losses which limit the quality factor to be on the order of 10^2. Furthermore, the *skin effect* produces loss which scales with frequency as a result of the crowding of the AC current density at the surface of the conductor. This effect is not present, at least nearly to the same degree, in a superconductor. Due to these advantages, high quality factors in superconducting resonators enables the study of very subtle effects in the microwave electromagnetic response and, in turn, the governing physics. Devices which incorporate these resonators have been used to probe the electrodynamics of thin film superconductors and to test

predictions of BCS theory [17]. Further applications include coupling to superconducting qubits for quantum computing applications [81], microwave kinetic inductance detectors (MKID) for astronomical measurements [74], simulation units for many-body physics experiments [75], and quantum limited parametric amplifiers [78].

The total quality factor of a resonator, Q_r is defined as the ratio of the energy stored in the resonator to the energy dissipated per cycle. In terms of the resonance frequency f_r and the power loss, we may generally write

$$Q_r = 2\pi f_r \times \frac{\text{Energy stored}}{\text{Power loss}}.$$

A freely oscillating resonator will lose energy internally via different and independent sources, each quantified by a loss factor $Q_{i,n}^{-1}$, and also by its coupling to an external circuit, Q_e^{-1}. The total quality factor of the resonator is given by

$$Q_r^{-1} = \sum_n Q_{i,n}^{-1} + Q_e^{-1}. \tag{1.1}$$

Quality factors of $Q_r \sim 10^{11}$ at large microwave power have been demonstrated [15] when particular attention to design details and fabrication is paid. In typical 2D planar geometries, with high-quality superconducting thin films and low-loss crystalline substrates, Q_i on the order of 10^6 or greater [54] are routinely obtained for microwave powers corresponding to a single microwave photon. There are a variety of physical effects which contribute to the loss of a superconducting resonator. One source of loss is non-equilibrium quasiparticles or un-paired electrons. Quasiparticles contribute to a finite complex conductivity for frequencies below the superconducting gap, which is $\Delta/\hbar \simeq 70$ GHz in aluminum [9] for example and on the order of a few hundred GHz for niobium [79]. The origin of the quasiparticles is suspected to arise in part from stray high-frequency radiation [7, 8]. At microwave powers corresponding a single photon the dominant source of loss is, however, totally unrelated to superconductivity. This loss mechanism is known as *dielectric loss* [73, 53] and will be introduced further in section 1.1.3.

1.1.2 Types of superconducting microwave resonators

Coplanar waveguide resonators

The most common type of a superconducting resonator is one consisting of a transmission line in a coplanar geometry [31] as shown in Fig. 1.1. Depending on geometry, a coplanar waveguide will support an electromagnetic quasi-TEM wave [68] of velocity

$$v_{\mathrm{ph}} = \frac{c}{\sqrt{\epsilon_{\mathrm{eff}}}} = \frac{1}{\sqrt{L_\ell C_\ell}}. \tag{1.2}$$

In equation (1.2), c is the speed of light in vacuum, ϵ_{eff} is the effective permittivity of the waveguide, and L_ℓ and C_ℓ are the inductance and capacitance per unit length, respectively. Since the size of the resonator is on the order of the wavelength, the electromagnetic properties vary along as a function of position. Because of this fact, the circuit is said to be distributed. To describe this type of resonator, it is typically considered as a series of infinitesimal inductive and capacitive elements. Terminating the transmission line of length ℓ at both ends with coupling capacitors C_k, (Fig. 1.1 a) allows for a standing electromagnetic wave of wavelength $\lambda = 2\ell$ and fundamental resonance frequency $f_1^{\lambda/2} = v_{ph}\,(2\ell)^{-1}$ to be excited. The coupling capacitances C_k must be sufficiently small to only allow transmission of microwave signals near resonance. Another type of coplanar resonator can be realized by coupling a coplanar waveguide feed line to a second waveguide which is open on the coupling end and grounded on the other (Fig. 1.1 b). This yields a fundamental mode $f_1^{\lambda/4} = v_{ph}\,(4\ell)^{-1}$ corresponding to a wavelength of $\lambda = 4\ell$. In both cases, n linear harmonics modes exist for odd values of n, given by $f_n \to n f_1$.

Coplanar waveguide resonators are attractive because only a single layer metallization step is typically necessary, making them robust and reproducible. Furthermore, high quality factors are readily obtained when low-loss crystalline substrates are used. Half-wavelength resonators yield transmission at the resonance frequency, therefore only a single resonator can be measured in a 2-port microwave setup. However, their design allows for asymmetric input and output capacitive coupling, a desirable feature for qubit measurement applications requiring improved readout signal. On the other hand, multiple quarter-wavelength resonators can be measured simultaneously when coupled to a single feed line, since they yield reflection at the resonance frequency. This benefit of *frequency multiplexing* is significant for large detector arrays where many different frequencies must be simultaneously read-out.

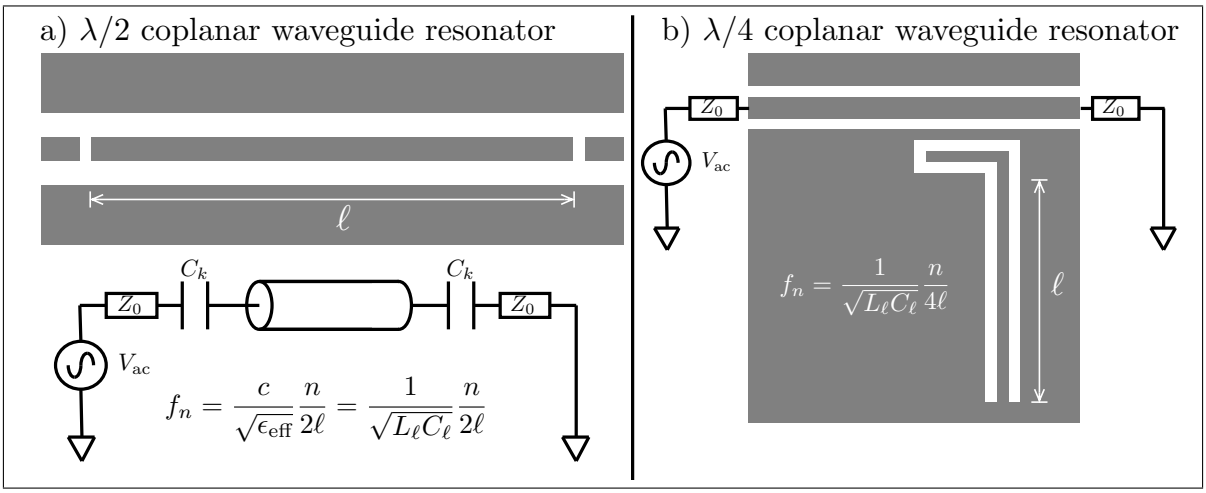

Figure 1.1: Two types of coplanar waveguide resonators coupled to an AC voltage drive V_{ac} of impedance Z_0. a) Half-wavelength ($\lambda/2$) Resonator: A transmission line of length ℓ, and effective permittivity $\epsilon_{\rm eff}$ is coupled capacitively on both ends by capacitors C_k. b) Quarter-wavelength ($\lambda/4$) Resonator: A transmission line of length ℓ is coupled to a coplanar feed line.

Lumped element LC resonators

A second type of superconducting resonator is one in which the inductor and capacitor elements are much smaller than the wavelength of the resonant mode. In this case, the circuit elements are said to be "lumped". Figure 1.2 shows a lumped element resonator consisting of a meander line inductor L and an interdigital capacitor C_0. In general, the circuit is coupled to a transmission line of inductance L_1 both by a capacitance C_c, and a mutual inductance $M = k\sqrt{LL_1}$, where k is a geometry dependent coupling factor. Contrary to coplanar resonators, energy storage in electric and magnetic fields is localized or "lumped" in specific circuit elements such as capacitors and inductors. The quality factor of an uncoupled LCR resonator is given by $Q = \omega_0 RC$. Similar to quarter-wavelength resonators, lumped element resonators have the advantage of operating in a frequency multiplexed configuration. Furthermore, they can also be miniaturized by the use of small parallel plate capacitors with relatively large capacitance [19, 18]. This usually comes at the price of significantly lowering quality factor by using a parallel plate dielectric capacitor which can be very lossy depending on the material. However, this increase in the resonator loss can be useful for studying and comparing dielectric loss with other types of resonators and also for applications requiring resonators where loss is less critical.

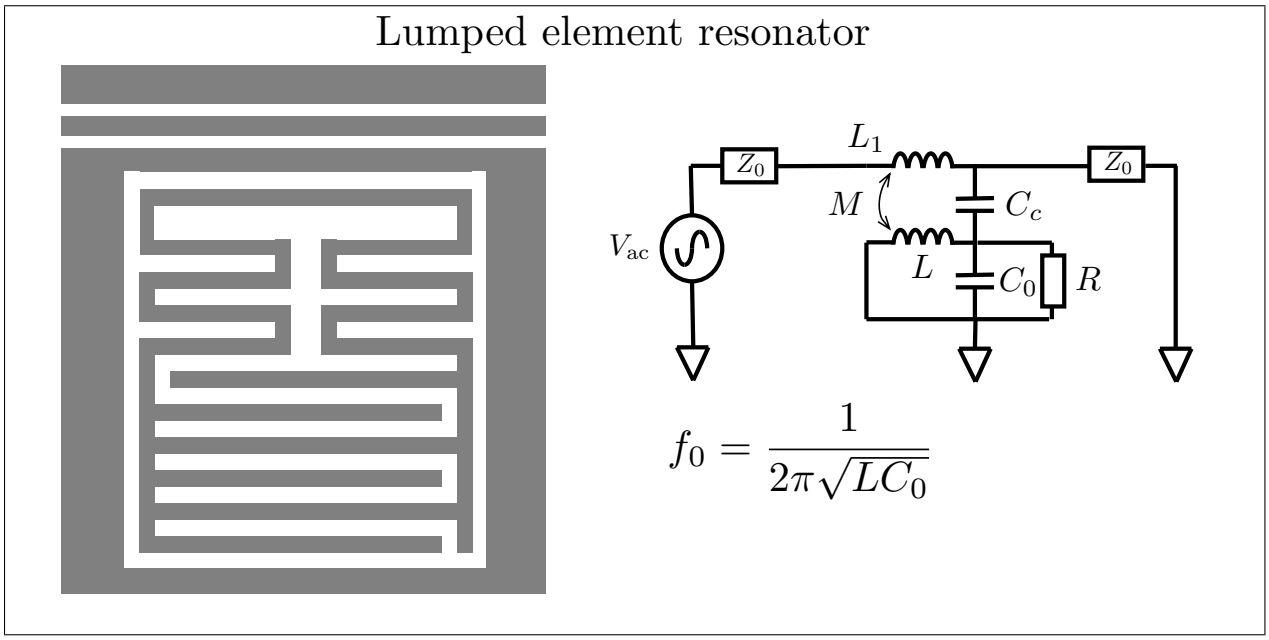

Figure 1.2: Left: Lumped element resonator consisting of an interdigital finger capacitor and meander-line inductor. Right: circuit diagram of a lumped element LC resonator consisting of an inductor L, capacitor C, and resistor R. The resonators has a resonance frequency of $f_0 = 1/2\pi\sqrt{LC}$ and is coupled capacitively by C_c and inductively by a mutual inductance M to a transmission line of impedance Z_0 and inductance L_1. The resonator is driven by an AC voltage source $V_{\rm ac}$.

3D cavity resonators

Microwave resonators can also be realized in a three dimensional architecture [60, 69], where the resonant mode is defined by the volume of the superconducting cavity. By using ultra-high quality superconducting material and careful surface treatment during fabrication, 3D cavities yield the highest quality factors at cryogenic temperatures and single-photon powers. The 3D spatial profile of the resonant mode results in further reduction of the electromagnetic energy density at the surface of the metal, and thus a lower contribution to dielectric loss. The main limitation of 3D cavity resonators is that coupling to other circuit elements such as qubits is more challenging due to the large spatial distribution of the electromagnetic mode. Furthermore they are much larger in size compared to 2D planar devices.

1.1.3 Application of superconducting microwave resonators to quantum information processing

Superconducting qubits are micro-fabricated microwave circuit structures consisting of one or more Josephson junctions. The field of quantum information processing with superconducting quantum bits has experienced significant progress over the past fifteen years. Over this time frame, the lifetimes of superconducting qubits have increased from nanoseconds to tens of microseconds, which has asserted their role as contenders in the race to construct scalable quantum technologies [20]. Much of this success is attributable to improvements in device design, material quality and reducing the effect of loss mechanisms. The Josephson junction is the key "quantum" ingredient of the circuit as it usually provides the necessary non-linearity to implement a qubit as a two-state system. The junction consists of two overlapping superconducting electrodes which are separated by a thin insulating oxide barrier. Tunnelling of Cooper pairs across the barrier is permitted and gives rise to a non-linear Josephson energy which depends on the difference in the phase of the superconducting wavefunction across the junction [41]. Various types of superconducting qubits can be realized, such as charge, flux, and phase qubits, depending on the parameters of the circuit. The common implementation of quantum information processing with superconducting qubits is in a *circuit quantum electrodynamics* (cQED) architecture [81, 12, 11] where the qubit is coupled to a superconducting microwave resonator. (Fig. 1.3 presents a setup similar to that implemented by our group here at the University of Waterloo.)

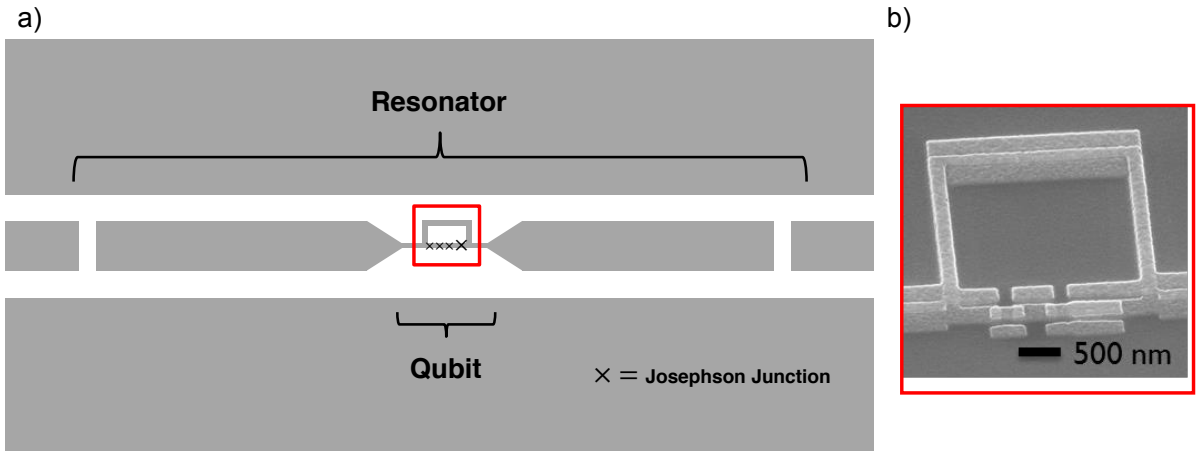

Figure 1.3: a) Schematic illustration of a circuit quantum electrodynamics device with a superconducting microwave resonator coupled to a flux qubit with four Josephson junctions. b) Scanning electron microscope image of a four-junction flux qubit fabricated using electron beam lithography.

An appropriate description of a superconducting resonator coupled to a qubit is one which is analogous to the interaction of an atom in an optical cavity. In the rotating wave approximation [39], the famous Jaynes-Cummings Hamiltonian, in the basis spanned by the non-interacting qubit-resonator states, reads

$$H_{JC} = \hbar\omega_r \left(\hat{a}^\dagger \hat{a} + \frac{1}{2}\right) + \frac{\hbar\omega_{qb}}{2}\hat{\sigma}_z + \hbar g \left(\hat{a}\hat{\sigma}_+ + \hat{a}^\dagger \hat{\sigma}_-\right), \tag{1.3}$$

where $\hat{a}$ ($\hat{a}^\dagger$), is the creation (annihilation) operator for a photon, ω_r is the bare frequency of the resonator, ω_{qb} is the qubit frequency and g is a coupling constant describing the strength of the cavity-qubit interaction. In such a system, the resonator can serve as a means to measure the state of the qubit by observing the effect of the qubit on the frequency of the resonator [81, 12, 11]. Equation (1.3), however, does not completely describe the behaviour of the resonator-qubit system. In reality there are additional dissipative terms which reflect the coupling of the qubit-resonator system to its environment. One can generally write the total Hamiltonian as

$$H_{\text{eff}} = H_{JC} + H_{\text{env}}, \tag{1.4}$$

where H_{env} is, in general, unknown and describes interactions with the environment. This coupling to the environment will describe the losses contributing to the quality factor of the resonator and therefore finite photon lifetime. Due to their mutual coupling, losses in the resonator will also couple to the qubit and cause decoherence. As mentioned above, progress in the field has been largely due to the development of a detailed understanding of the physics contributing to H_{env} and minimizing its impact on the performance of the device by improved fabrication methods and materials. As we will see in the next section, quality factor measurements of resonators provide a convenient method to probe such sources of loss.

1.1.4 Dielectric loss due to two-level systems

Developments in the field of superconducting quantum devices have revived interest in the field of amorphous materials [65]. It was mentioned in section 1.1.1 that the dominant source of loss in the quantum (single-photon) regime arises due to mechanisms totally unrelated to superconductivity. This source of loss, known as *dielectric loss,* arises from the fundamental behaviour of amorphous materials at low temperatures. We will introduce the essential features here with respect to the field of superconducting devices, and a more general discussion of the relevant physics will be presented in the following chapter.

Superconducting devices inevitably contain amorphous dielectric materials which are well-known to become very lossy at temperatures below 1 K [64]. These materials are not only present in the tunnel oxide barrier of the Josephson junction [77, 53, 76], but also as thin layers on the surfaces of the substrate and the superconductor [25, 54, 61]. In general, an amorphous material contains low energy levels which are typically viewed as tunnelling two-level systems (TLS). A TLS may undergo resonant transitions by absorption or emission of photons or phonons [37, 5]. The photon interaction contributes to the complex permittivity of the material defined as $\epsilon(\omega) = \epsilon'(\omega) - i\epsilon''(\omega)$. In the case of a superconducting resonator, the electric field of the resonator couples to a TLS and drives excitations. When expressed in terms of the *dielectric loss tangent,* $\tan\delta = \epsilon''/\epsilon'$, the contribution to the internal loss of the resonator, in the weak electric field limit and at frequencies for which $\hbar\omega_r > 2k_BT$, is given by

$$Q_i = p_m \tan\delta = p_m Q_0^{-1}, \tag{1.5}$$

where p_m is the participation ratio [84, 58] or filling factor of the dielectric and Q_i is the internal

quality factor of the resonator. The participation ratio is the electric field energy stored in the lossy amorphous material divided by the total electrical energy stored in the resonator:

$$p_m = \int_{\text{TLS}} d\mathbf{r}|\mathbf{E}(\mathbf{r})|^2\epsilon(\mathbf{r}) \Big/ \int_{\text{Total}} d\mathbf{r}|\mathbf{E}(\mathbf{r})|^2\epsilon(\mathbf{r}). \tag{1.6}$$

The factor Q_0^{-1} depends on intrinsic parameters of the material and the two-level systems and is given by

$$Q_0^{-1} = \frac{\pi p_0^2 P_0}{3\epsilon}, \tag{1.7}$$

where p_0 is the effective dipole moment of the two-level systems, P_0 is the density of two-level states, and ϵ is the magnitude of the dielectric constant of the material.

Equation (1.5) describes the unsaturated regime, valid for weak electric fields when the rate of TLS relaxation is greater than the rate of excitation. Crudely speaking, when the number of photons is small, a TLS which absorbs a photon will have time to relax back to thermal equilibrium through interaction with thermal phonons long before it is likely to be excited by a second photon. As the strength of the electric field is increased, the photon flux will reach a certain value at which the rate of TLS excitation is equal to the rate of relaxation. At this point the tunnelling systems become saturated due to their two-level character. This saturation leads to a decrease in $Q_i^{-1}(\omega, T)$ for an increasing electric field E since the TLS distribution may absorb only a fraction of the total photons in the material. Much of the relevant physics can be analogously understood in terms of the framework for two-state spin systems in magnetic resonance [34, 65]. This will be discussed further in the next chapter. To account for saturation and including a temperature dependent factor, equation (1.5) acquires a non-linear field dependent factor, and is re-cast in the following form:

$$Q_i^{-1}(\omega, T) = p_m Q_0^{-1} \tanh\left(\hbar\omega/2k_BT\right) \Big/ \sqrt{1 + \left(|E(\mathbf{r})|/E_c\right)^2}, \tag{1.8}$$

where E_c is the critical saturation field. Equation (1.8) presents some unfortunate consequences for qubits which require operation in the low-power quantum regime where $\hbar\omega > 2k_BT$ and $|E(\mathbf{r})| \ll E_c$. Clearly, in this regime, the loss from TLS is greatest.

Most high-quality superconducting resonators consist of a superconducting thin film patterned onto a high-purity crystalline substrate such as silicon or sapphire. Even when great care is taken during fabrication, the formation of amorphous oxide layers on the device is very challenging to

avoid. Under ambient conditions native oxide layers on the metal and substrates will form with thicknesses on the order of a few nanometers. On aluminum, for example, native AlO_x forms nearly instantaneously at atmospheric pressure with a thickness up to ∼5 nm. Similarly, NbO_x, native oxides of niobium, growth occurs over the course of a few hours. On the substrate, silicon for example, layers of ∼2-5 nm will also naturally form [55]. Each lossy amorphous layer in the sample contributes an amount to the loss proportional to its participation factor, p_m. The geometry of the resonator can be designed in such a way that the electric field energy density is minimized at lossy surfaces and the coupling to two-level systems is reduced [26, 43, 70]. On the other hand, lossy amorphous layers can be deposited or grown on the capacitor to increase p_m for the purposes of studying in detail the effects of the loss [42, 14, 52, 53]. This allows superconducting devices to be used as tools to probe the intrinsic properties of an amorphous material.

1.1.5 Loss in aluminum oxide

Aluminum oxide, Al_2O_3, or more generally AlO_x in the case of unknown stoichiometry, is one of the most important materials in microfabricated superconducting devices. This is because of its critical role in forming the tunnel oxide barrier in superconductor-insulator-superconductor (SIS) Josephson junctions. These films are typically amorphous and therefore contain two-level systems, which can couple strongly to qubits containing the junctions and induce decoherence channels. Recent research has demonstrated that TLS populations can be greatly reduced by using epitaxial junctions [56]. This approach imposes considerable fabrication constraints and improvements in qubit lifetimes have not been demonstrated. The performance and efficiency of superconducting qubits relies heavily on the quality of the AlO_x which forms the junction.

Qubits have been used in experiments to probe individual TLS [53, 50, 76] by bringing the qubit into resonance with the TLS and using it to excite transitions. This has the unique benefit of being able to characterize properties of single TLSs, but due to the small areas of typical junctions, which are typically much less than 1 μm^2, the broad character of the TLS distribution is not apparent nor is the role of any mutual interaction between them. In this thesis, we characterize loss in aluminum oxide grown by atomic layer deposition. This growth technique produces a material which is similar to that used for Josephson junctions, yet has some different properties in terms of specific stoichiometry and chemical impurity content. These differences could yield a different distribution of TLS parameters. The technique of atomic layer deposition

can be used to grow amorphous films of well defined thicknesses, which can be much thicker than what is achievable with standard plasma oxidation. This allows for thick layers to be deposited on the resonators, which allows for an accurate characterization of the loss.

1.1.6 Outline of the thesis

Chapter 2 will present the necessary physical description of an amorphous material at low temperatures. Chapter 3 describes the experimental methods involved in a systematic characterization of dielectric loss by measurements of superconducting resonators. Chapter 4 presents the characterization of the attenuation of the input coaxial microwave lines which is an important parameter in the accurate quantification of dielectric loss parameters. Chapter 5 addresses the issue of measuring dielectric loss in resonators for which the electric field is spatially inhomogeneous. Chapter 6 employs the methods of the previous chapters in a complete analysis of the temperature-dependent dielectric loss properties.

Chapter 2

Amorphous dielectrics: the tunnelling two-level system model

2.1 Historical perspective

In the early 1970's, measurements of thermodynamic properties of amorphous materials below 10 K demonstrated striking differences compared to crystals. A large contribution to the specific heat roughly linear in T was observed to dominate over the Debye T^3 phonon component [87]. The thermal conductivity was found to be not only much smaller than what is measured in crystals, but also varying as $\sim T^2$ and reaching a surprising "plateau" around 1 K. In the following years, further anomalies in the ultrasonic [28, 66] and dielectric behaviour [73] were reported. All of the observed phenomena suggested the existence of other degrees of freedom which contribute to the energy of the systems at low temperatures0. This fact came as a complete surprise since the prevailing scientific wisdom at the time was that amorphous systems should behave the same as crystals. This argument was accepted on the basis that the internal energy of the system at low-temperatures is due to long wavelength phonons of energy on the order of k_BT which are effectively immune to disorder at a scale far less than the wavelength. Thus, it was generally agreed upon that an amorphous material, as a crystal, could be treated as an elastic continuum. It had been suspected, however, that the microscopic disorder would produce other modes, but the strength with which these modes were observed to interact with phonons was unprecedented. As a result, amorphous materials quickly became a focal point in condensed matter physics. Important

progress was achieved throughout the 1970s and 80s, yet, there remained some questions of genuine scientific uncertainty concerning the nature of amorphous materials at low temperature.

In 1972, Phillips [63] and, independently, Anderson, Halperin and Varma [5] developed the tunnelling two-level system (TLS) model, which satisfactorily explained most observations. The TLS model considers the intrinsic disorder of an amorphous material to be such that some of the atoms (or groups of atoms) will have two metastable equilibrium configuration states. It is further proposed that, at sufficiently low temperatures, quantum tunnelling between the states is permitted (see Fig. 2.1). The two-level nature of the excitation is, of course, a radical simplification, but nonetheless one which provides a qualitative explanation of the measurements. The TLS model, in its original formulation, is an adaptation of the tunnelling model [21] developed to explain the physics related to defects in crystalline systems. The main difference lies in the choice of the distribution function describing the two-level systems in the material. In a crystal, the distribution is sharply peaked at a particular energy, typically unique to the tunnelling defect itself. Experiments on amorphous materials at different energy scales have shown the existence of "two-level systems". From this, it is generally agreed upon that the two-level systems have a *constant* density of states over typical energy scales of interest, which in turn implies that TLSs of varying energies are equally likely to occur.

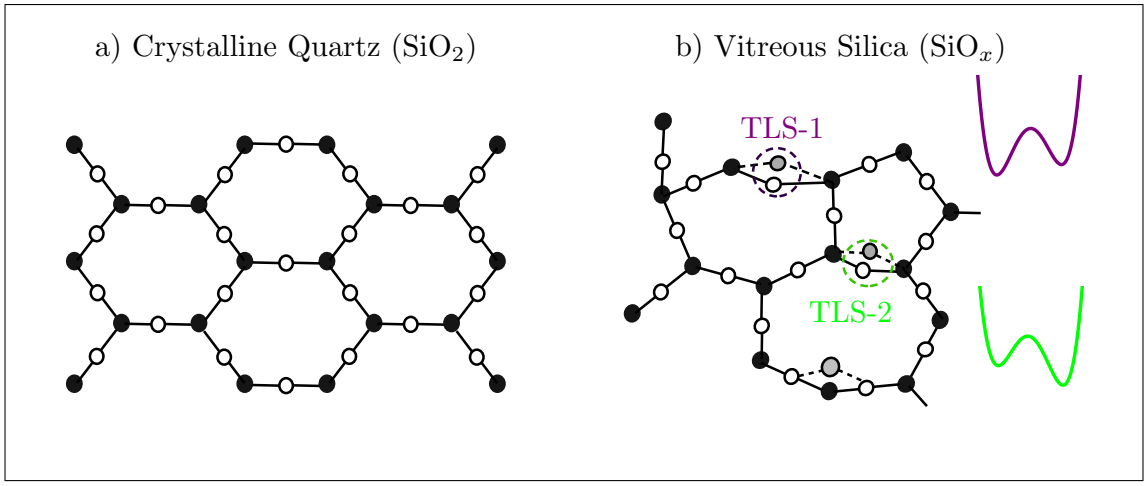

Figure 2.1: a) Diagram of crystalline Quartz. Black (white) circles represent Si (O). (adapted from Enss and Hunklinger, Low temperature physics, Ch. 9, Springer, 2004). b) Amorphous vitreous silica, illustrating the existence of two-level systems described by double well potentials. The purple and green two level systems depict two different double well potentials.

2.2 The tunnelling two-level system model

In the original TLS model, certain atoms or groups of atoms in an amorphous material have two nearby equilibrium positions. At sufficiently low temperatures, the tunnelling of the atoms between equilibrium positions becomes important. This can be modelled phenomenologically as a double well potential V formed by the overlap of two single well potentials, V_1 and V_2, as shown in Fig. 2.2. To calculate the energy levels, we begin with solutions to the single well problem, using basis states in the *localized* representation, $|\phi_1\rangle$ and $|\phi_2\rangle$, which are ground states of the Hamiltonians H_1 and H_2 respectively. The Hamiltonian of the double well can be written as

$$H = H_1 + (V - V_1) + H_2 + (V - V_2). \tag{2.1}$$

The eigenvalues of the double well can be found by solving the Schrödinger equation $H|\psi\rangle = E|\psi\rangle$ using the following state as an ansatz:

$$|\psi\rangle = a_1|\phi_1\rangle + a_2|\phi_2\rangle. \tag{2.2}$$

The energy eigenvalue E is thus given by [21]

$$E = \frac{\langle\psi|H|\psi\rangle}{\langle\psi|\psi\rangle} = \frac{a_1^2\langle\phi_1|H|\phi_1\rangle + a_2^2\langle\phi_2|H|\phi_2\rangle + 2a_2a_1\langle\phi_1|H|\phi_2\rangle}{a_1^2 + a_2^2 + 2a_1a_2\langle\phi_1|\phi_2\rangle} \tag{2.3}$$

We identify the following matrix elements:

$$H_{11} = \langle\phi_1|H|\phi_1\rangle = \langle\phi_1|H_1|\phi_1\rangle + \langle\phi_1|V - V_1|\phi_1\rangle, \tag{2.4}$$

$$H_{22} = \langle\phi_2|H|\phi_2\rangle = \langle\phi_2|H_2|\phi_2\rangle + \langle\phi_2|V - V_2|\phi_2\rangle, \tag{2.5}$$

$$H_{12} = H_{21} = \langle\phi_1|H|\phi_2\rangle \tag{2.6}$$

where $\langle\phi_1|H_1|\phi_1\rangle \equiv E_1$ and $\langle\phi_2|H_2|\phi_2\rangle \equiv E_2$ are the eigenenergies of the isolated wells, and $H_{12} = \langle\phi_1|H|\phi_2\rangle$ is the off-diagonal exchange energy due to the overlap of the localized wavefunctions. If extension of the individual well ground states into the barrier is small, to a good approximation, the terms $\langle\phi_i|V - V_i|\phi_i\rangle$ terms can be neglected in comparison to E_i. As the separation of the wells increases, H_{12} and $\langle\phi_1|\phi_2\rangle$ tend to zero. To find the different energies , we impose that E must be minimized with respect to the coefficients a_1 and a_2. By differentiating (2.3) with

respect to a_1 and a_2 we obtain the following characteristic equations:

$$\frac{\partial E}{\partial a_1} = 0 \rightarrow a_1 \left(H_{11} - E\right) + a_2 \left(H_{12} - E\langle\phi_1|\phi_2\rangle\right) = 0, \tag{2.7}$$

$$\frac{\partial E}{\partial a_2} = 0 \rightarrow a_1 \left(H_{12} - E\langle\phi_1|\phi_2\rangle\right) + a_2 \left(H_{22} - E\right) = 0. \tag{2.8}$$

By eliminating the coefficients a_1 and a_2, we obtain the following solution:

$$\left(H_{11} - E\right)\left(H_{22} - E\right) - \left(H_{12} - E\langle\phi_1|\phi_2\rangle\right) = 0. \tag{2.9}$$

We choose the zero point energy $\hbar\Omega \equiv \frac{1}{2}(E_1 + E_2)$ to be the average between those for the two isolated wells. It follows that the eigenenergies of each well can be expressed as

$$H_{11} = E_1 = \frac{1}{2}\left(\hbar\Omega + \Delta\right), \tag{2.10}$$

$$H_{22} = E_2 = \frac{1}{2}\left(\hbar\Omega - \Delta\right),$$

where $\Delta = |V_1 - V_2|$. The terms containing $\langle\phi_1|\phi_2\rangle$ in equation (2.9) can be ignored in the limit when the wavefunction overlap is weak. By combining equations (2.10) and (2.9) the eigenenergies of the double well are found to be

$$E_{\pm} = \frac{1}{2}\left(\hbar\Omega \pm \sqrt{\Delta^2 + 4H_{12}^2}\right), \tag{2.11}$$

and the level splitting of the ground state is

$$E = E_+ - E_- = \sqrt{\Delta^2 + \Delta_0^2}, \tag{2.12}$$

where $\Delta_0 = -2H_{12}$ is called the *tunnel splitting.* Δ_0 can be evaluated for specific forms of V by applying the WKB method. Since the true form of the microscopic potential is generally unknown, the commonly used result relating the tunneling splitting to the potential is

$$\Delta_0 \simeq \hbar\Omega \exp\left(-\lambda\right), \tag{2.13}$$

$$\lambda = \frac{d}{\hbar}\sqrt{2mV_0}, \tag{2.14}$$

where m is the mass of the tunnelling system, V_0 is the barrier height and d is the separation between the wells. The quantity λ is called the *tunnelling parameter.* In the local basis formed by ϕ_1 and ϕ_2, we can write the Hamiltonian as

$$H_l = \frac{1}{2}\begin{pmatrix} -\Delta & \Delta_0 \\ \Delta_0 & \Delta \end{pmatrix}. \tag{2.15}$$

Writing in the diagonal basis formed by ψ_1 and ψ_2 we obtain

$$H_d = \frac{1}{2}\begin{pmatrix} -E & 0 \\ 0 & E \end{pmatrix} = -\frac{1}{2}E\sigma_z, \tag{2.16}$$

where E is given by equation (2.12). It follows that the normalized eigenstates of the double well TLS potential are given by

$$|\psi_1\rangle = \cos\theta|\phi_1\rangle + \sin\theta|\phi_2\rangle, \tag{2.17}$$

$$|\psi_2\rangle = \sin\theta|\phi_1\rangle - \cos\theta|\phi_2\rangle, \tag{2.18}$$

where the eigenenergies of $|\psi_1\rangle$ and $\psi_2\rangle$ are E and $-E$ respectively and $\tan 2\theta = \Delta_0/\Delta$.

2.2.1 TLS dipole moment

The dipole moment of the tunnelling system can be easily calculated in the limit where the overlap of the localized wavefunctions ϕ_i is small. It is important to note the dual nature of the dipole moment. First, it may be considered as an electric dipole where each eigenstate of the system represents a different configuration of charge. Secondly, it may serve as an acoustic dipole [21, 35] where different configurations alter the mass density and local strain field in the material. This second feature further reflects the ability of the TLS to couple electromagnetically to photons and elastically to phonons. For the electric case, the expectation value of the dipole moment p_1 for the state $|\psi_1\rangle$ is the following:

$$\langle p_1\rangle = \langle\psi_1|qx|\psi_1\rangle, \tag{2.19}$$

where q is the charge of the two level system and x is the position operator. Inserting $|\psi_1\rangle$ given by equation (2.17) we obtain

$$\langle p_1 \rangle \quad = \quad q \int dx \left(\phi_1^* \cos\theta + \phi_2^* \sin\theta\right) x \left(\phi_1 \cos\theta + \phi_2 \sin\theta\right). \tag{2.20}$$

Expanding equation (2.20), ignoring the overlap terms $\int dx \phi_1^* \phi_2$ and $\int dx \phi_2^* \phi_1$ and making use of the identities $2\sin^2\theta = 1 - \cos 2\theta$ and $2\cos^2\theta = 1 + \cos 2\theta$, we find

$$p_1 = \frac{q}{2} \int dx \phi_1^* x \phi_1 (1 + \cos 2\theta) + \frac{q}{2} \int dx \phi_2^* x \phi_2 (1 - \cos 2\theta). \tag{2.21}$$

The dipole moment of the TLS in one of the localized wells p_0 is denoted as $q \int dx \phi_1^* x \phi_1 = -q \int dx \phi_2^* x \phi_2 \equiv p_0$. Using equation (2.12) and $\tan 2\theta = \Delta_0/\Delta$, it follows that

$$p_1 = \frac{p_0}{2}\left(1 + \frac{\Delta}{E}\right) - \frac{p_0}{2}\left(1 - \frac{\Delta}{E}\right) = p_0 \frac{\Delta}{E}. \tag{2.22}$$

Similarly, for p_2 we have

$$p_2 \quad = \quad -p_0 \frac{\Delta}{E} = -p_1. \tag{2.23}$$

The TLS dipole moment is the most physically relevant quantity in the description of dynamic effects which arise due to the coupling to external fields. This will be discussed later in section 2.3. Next, some necessary assumptions are made to describe a distribution of TLSs, a necessary entity for understanding measurements of bulk amorphous materials.

2.2.2 TLS distribution function

Most experiments measure bulk properties of an amorphous material, as opposed to the discrete nature of a TLS. In order to predict the effect of many TLSs, knowledge of the distribution of their parameters is required. In an amorphous material the existence of many nearly-identical tunnelling systems is generally agreed upon to be unlikely. This is due to the assumption that, contrary to defects in crystals, the random internal structure of an amorphous material likely produces a broad distribution of both the asymmetry energy Δ and the tunnelling parameter λ. Moreover, it is assumed that Δ and λ are independent microscopic parameters. Therefore, they

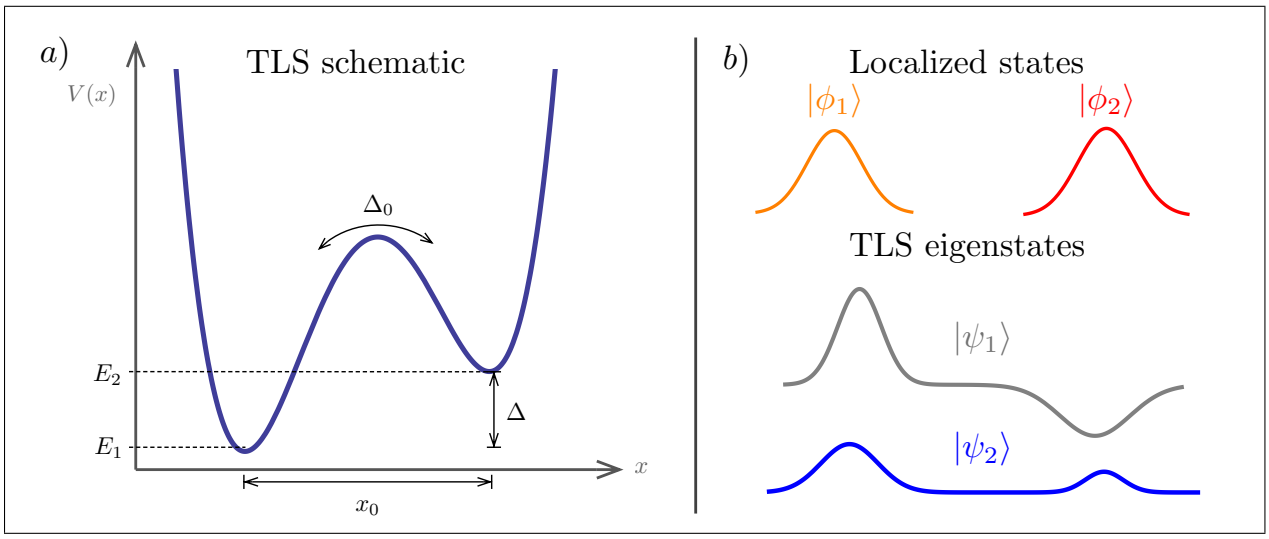

Figure 2.2: a) Schematic of a tunnelling two-level system. The overlap of two harmonic potentials of energy E_1 and E_2 and ground states ϕ_1 and ϕ_2 forms a double well potential with an asymmetry energy Δ and tunnelling energy Δ_0. The wells are separated by a distance x_0 along the dipole axis of the TLS which is typically on the order of $<$ 1nm. b) The eigenstates, assuming the overlap of ϕ_1 and ϕ_2 is small, are given by $\psi_1 = \cos\theta\phi_1 + \sin\theta\phi_2$ and $\psi_2 = \sin\theta\phi_1 - \cos\theta\phi_2$, where $\tan 2\theta = \Delta_0/\Delta$.

are uniformly distributed over the energy density element $d\Delta d\lambda$ and we can write the distribution function as [5, 21, 65]

$$P(\Delta,\lambda)d\Delta d\lambda = P_0 d\Delta d\lambda, \tag{2.24}$$

where P_0 is a constant. Given that $\Delta_0 = \hbar\Omega e^{-\lambda}$ and $|\frac{d\Delta_0}{d\lambda}| = \Delta_0$, an equivalent distribution can be expressed in terms of the tunnelling energy Δ_0. It is written as

$$\begin{aligned} P(\Delta,\Delta_0)d\Delta d\Delta_0 &= P(\Delta,\lambda)d\Delta\frac{d\Delta_0}{\Delta_0} && (2.25)\\ &= \frac{P_0}{\Delta_0}d\Delta d\Delta_0. && (2.26)\end{aligned}$$

Another useful representation of the distribution function is one in terms of total energy E and Δ_0. $P(E,\Delta_0)$ is determined from $P(\Delta,\lambda)$ by a Jacobian variable transformation, and the result is

$$\begin{aligned} P(E,\Delta_0)dEd\Delta_0 &= P(\Delta,\lambda)\begin{vmatrix} \frac{\partial\lambda}{\partial\Delta_0} & \frac{\partial\lambda}{\partial E} \\ \frac{\partial\Delta}{\partial\Delta_0} & \frac{\partial\Delta}{\partial E}\end{vmatrix} dEd\Delta_0 \\ &= P(\Delta,\lambda)\left|\frac{\partial\lambda}{\partial\Delta_0}\right|\left|\frac{\partial\Delta}{\partial E}\right| dEd\Delta_0 && (2.27)\\ &= \frac{P_0}{\Delta_0}\frac{E}{\sqrt{E^2-\Delta_0^2}}dEd\Delta_0. && (2.28)\end{aligned}$$

Integration over Δ_0 yields the density of states $\rho(E)$. To avoid an unphysical divergence in the integral, a minimum tunnelling energy $\Delta_0^{\min} \neq 0$ must be introduced. The density of states is then found to be

$$\begin{aligned} \rho(E) &= P_0\int_{\Delta_0^{\min}}^{E}\frac{E}{\Delta_0\sqrt{E^2-\Delta_0}}d\Delta_0 && (2.29)\\ &\simeq P_0\ln\left(\frac{E}{\Delta_0^{\min}}\right). && (2.30)\end{aligned}$$

The physical nature of $\Delta_0^{\min}$ is a consequence of the existence of $\lambda_{\max}$ corresponding to the maximum barrier height for which tunnelling is permitted. Equation (2.30) can then be used to calculate the internal energy due to TLSs and subsequently the specific heat. The form of equation (2.30) results in a linear temperature dependence in the specific heat. This provided

the first explanation of initial experiments [87]. The logarithmic factor which depends on energy is typically very slowly varying over experimental energy scales of interest, and is therefore commonly ignored and the density of states is treated as $\rho(E) \simeq$ constant.

2.3 Response to a weak external field

2.3.1 Dynamics

The time dependent behaviour of the two-level system is captured by the complex amplitudes $A_1(t)$ and $A_2(t)$ of the appropriate eigenstates ψ_1 and ψ_2. The general time dependent wavefunction can be written as

$$\Psi(t) = A_1(t)\psi_1(x)\exp(-iE_1t/\hbar) + A_2(t)\psi_2(x)\exp(-iE_2t/\hbar), \tag{2.31}$$

where E_1 and E_2 are the eigenenergies. Two quantities of interest are the difference in probabilities of finding the TLS in either of the two states $A_2^*A_2 - A_1^*A_1$, and $A_1^*A_2$, which quantifies the phase difference between ψ_1 and ψ_2. These two quantities are necessary in a full dynamical description. The average value of time-dependent dipole can now be calculated using the state given by equation (2.31).

$$\begin{aligned} \langle p(t)\rangle &= \langle\Psi(t)|qx|\Psi(t)\rangle \\ &= p_1\left(A_1^*A_1 - A_2^*A_2\right) + p_{12}\left(A_1^*A_2e^{i\omega_0t} + A_2^*A_1e^{-i\omega_0t}\right). \end{aligned} \tag{2.32}$$

In equation (2.32) we have introduced $\hbar\omega_0 \equiv E_2 - E_1$ as the difference in energy of the stationary states, and used the following static diagonal (p_1 and p_2) and off-diagonal (p_{12} and p_{21}) dipole moments:

$$p_1 = q\langle\psi_1|x|\psi_1\rangle = -p_2 = -q\langle\psi_2|x|\psi_2\rangle, \tag{2.33}$$

$$p_{12} = p_{21} = q\langle\psi_2|x|\psi_1\rangle. \tag{2.34}$$

$A_1(t)$ and $A_2(t)$ are determined by the time-dependent Schrödinger equation $i\hbar\frac{\partial}{\partial t}\Psi = H(t)\Psi$. When the external field is weak, the time evolution of the TLS may be treated using perturbation theory. In this case the TLS excitation rate induced by the perturbation field is not enough to

significantly alter the thermal equilibrium distribution of ψ_1 and ψ_2, and the terms describing the phase coherence $A_1^* A_2$ can be neglected. For strong fields, the phase coherence plays an important role and will be addressed in section 2.2.3.

Experimental evidence confirms the significant contribution of two-level systems to the thermal properties of amorphous materials. For $T < 1$ K, this means energies less than 20 GHz are necessary to drive resonant transitions. For electromagnetic and elastic acoustic waves this corresponds to wavelengths on the order of 10 mm and 100 nm or less respectively. The spatial extent of a TLS will vary between materials, but it is generally found to be less than 1 nm. Therefore, the magnitude of the field is roughly homogeneous from the perspective of the TLS and the coupling can be treated as dipolar. In this regime, the dominant effect of the field is to modulate the asymmetry energy Δ. This perturbation is therefore diagonal in the basis of the localized states ϕ_i. Transforming to the diagonal basis formed by ψ_i, the interaction Hamiltonian for the *tunnelling model* reads

$$H_{\text{int}} = \left| \frac{\Delta}{E}\sigma_z + \frac{\Delta_0}{E}\sigma_x \right| \left(\mathbf{p}_0 \cdot \boldsymbol{\xi}(t) + \boldsymbol{\gamma} \cdot \boldsymbol{e}(t) \right), \tag{2.35}$$

where $\mathbf{p}_0 = \left(\frac{1}{2}\frac{\partial \Delta}{\partial \xi}, \frac{1}{2}\frac{\partial \Delta_0}{\partial \xi}, 0 \right)$ is the dipole coupling of the TLS to an electric field $\boldsymbol{\xi}$ and, equivalently, γ is the coupling to the tensorial strain field $\boldsymbol{e}$. The interaction Hamiltonian includes interactions with both electric and elastic strain fields reflecting the fact that they have the same effect on the TLS. An important point must be made concerning equation (2.35). Clearly, the σ_z terms will change the relative energies of of ψ_1 and ψ_2, while the σ_x terms will drive transitions between them. There is a relationship between the diagonal and off-diagonal terms, since they both depend on the TLS energy, E. A simpler interpretation can be made in terms of an interaction Hamiltonian which ignores this relationship and considers independent diagonal and off-diagonal electric dipole moments μ and $\tilde{\mu}$ and acoustic dipole moments D and M. In this representation, the energy difference between the two states is described completely by E alone, and the interaction Hamiltonian for the *two-level system* model reads

$$H_{\text{int}} = \left(\frac{1}{2}\mu\sigma_x + \tilde{\mu}\sigma_z \right) \xi(t) + \left(\frac{1}{2} D\sigma_x + M\sigma_z \right) e(t), \tag{2.36}$$

for coupling to both electric and elastic fields.

2.3.2 TLS relaxation

A TLS in an amorphous material will interact with a random strain field produced thermal phonons. This phonon field can be treated as a superposition of different phonon modes. The heat bath drives the TLS towards thermal equilibrium, at which point the occupation probabilities $P_1 = A_1^* A_1 = P_1^{\text{eq}}$ and $P_2 = A_2^* A_2 = P_2^{\text{eq}}$ are independent of time. In this steady state regime [64] we have

$$P_1^{\text{eq}} \Omega_{12} = P_2^{\text{eq}} \Omega_{21}, \tag{2.37}$$

where Ω_{12} and Ω_{21} are the transition rates from $\psi_1 \to \psi_2$ (resonant absorption) and $\psi_2 \to \psi_1$ (stimulated emission), respectively. Away from equilibrium, the rate equations for P_1 and P_2 are given by

$$\frac{dP_1}{dt} = -P_1 \Omega_{12} + P_2 \Omega_{21}, \tag{2.38}$$

$$\frac{dP_2}{dt} = P_1 \Omega_{12} - P_2 \Omega_{21}. \tag{2.39}$$

Writing (2.38) in terms of P_1 only we obtain

$$\frac{dP_1}{dt} = -P_1 \left(\Omega_{12} + \Omega_{21} \right) + \Omega_{21}. \tag{2.40}$$

The relative population and rate is given simply by the Boltzmann factor

$$\frac{P_1^0}{P_2^0} = \frac{\Omega_{21}}{\Omega_{12}} = e^{-E/k_B T}. \tag{2.41}$$

Introducing a relaxation rate T_1^{-1} as the sum of two transition rates, we have

$$T_1^{-1} = \Omega_{12} + \Omega_{21} = \Omega_{12} \left(1 + e^{E/k_B T} \right). \tag{2.42}$$

The transition rate Ω_{12} is calculated using the Golden Rule, where the density of final states is given by the phonon field. From this, we obtain

$$\Omega_{12} = \frac{2\pi}{\hbar} \sum_{\alpha} \left| \langle \psi_1 | H_{\text{int},\alpha} | \psi_2 \rangle \right|^2 g(E) f_B(E), \tag{2.43}$$

where $g(E)$ is the Debye density of phonon states which define thermal equilibrium, $f_B(E)$ is the Bose-Einstein distribution, and the sum is over phonon polarizations α. Thermal equilibrium is achieved through interaction with the phonon strain field $\boldsymbol{e}$. The amplitude of an acoustic phonon wave $2e_0 \cos\omega t$ can be written as $\sqrt{\hbar/2\rho\omega}\,(\omega/v_\alpha)$, where v_α is the phonon wave-speed and ω is the angular phonon frequency. Applying this to $H_{\mathrm{int},\alpha}$ given by (2.35), the matrix element in (2.43) becomes

$$\langle\psi_1|H_{\mathrm{int},\alpha}|\psi_2\rangle = \gamma_\alpha\sqrt{\frac{\hbar\omega}{2\rho v_\alpha^2}}\left(\frac{\Delta}{E}\int dx\psi_1^*\sigma_z\psi_2 + \frac{\Delta_0}{E}\int dx\psi_1^*\sigma_x\psi_2\right). \tag{2.44}$$

We note that ψ_1 and ψ_2 are eigenstates of σ_z and that $\sigma_x\psi_2 = \psi_1$. Therefore, the first term in (2.44) vanishes and we obtain

$$\langle\psi_1|H_{\mathrm{int},\alpha}|\psi_2\rangle = \gamma_\alpha\sqrt{\frac{\hbar\omega}{2\rho v_\alpha^2}}\frac{\Delta_0}{E}, \tag{2.45}$$

and the transition rate Ω_{12} becomes

$$\Omega_{12} \;=\; \sum_\alpha \frac{\gamma_\alpha^2}{v_\alpha^5}\frac{\Delta_0^2 E}{2\pi\rho\hbar^4}\frac{1}{e^{E/k_BT}-1}, \tag{2.46}$$

where we have used the phonon energy $E \equiv \hbar\omega$. The relaxation rate T_1^{-1} is then given by

$$T_1^{-1} = \sum_\alpha \frac{\gamma_\alpha^2}{v_\alpha^5}\frac{\Delta_0^2 E}{2\pi\rho\hbar^4}\coth(E/2k_BT). \tag{2.47}$$

Equation (2.49) is the relaxation rate for a *tunnelling system* which depends on both the total energy E and the tunnelling energy Δ_0. The equivalent expression for the *two-level system*, according to $H_{\mathrm{int},\alpha}$ given instead by (2.36), is obtained by setting $\Delta_0 \to E$. In this case, the existence of many different relaxation rates for all allowed values of Δ_0 is ignored. It is also important to note that since the relaxation time for the two-level case occurs for $E = \Delta_0$, $\Delta = 0$. This defines a minimum relaxation time $T_{1,m}$, so T_1 for the tunnelling case can be conveniently expressed as

$$T_1(E,\Delta_0) = \frac{E^2}{\Delta_0^2}T_{1,m}(E). \tag{2.48}$$

By differentiating with respect to Δ_0 we obtain

$$\frac{d\Delta_0}{\Delta_0} = -\frac{1}{2}\frac{dT_1\Delta_0^2}{T_{1,m}(E)E^2} = -\frac{1}{2}\frac{dT_1}{T_1} \tag{2.49}$$

Using (2.48) and (2.49), (2.28) can be alternatively written in terms of E and T_1 as the following [37],

$$P(E,\Delta_0)dEd\Delta_0 \rightarrow P(E,T_1)dEdT_1 = \frac{P_0 dEdT_1}{2T_1\sqrt{1-T_{1,m}(E)/T_1}}. \tag{2.50}$$

Equation (2.50) describes the range of T_1 allowed by the distribution of Δ_0 (eq. 2.26). The nature of (2.50) presents measurable consequences depending on the experimental timescale. For example, measurements of specific heat demonstrated a time dependence which can be understood in terms of an effective density of states ρ_{eff} including only states which relax within the duration of the experiment, t_{exp}, calculated as

$$\rho_{\text{eff}}(E) = \int_{T_{1,m}}^{t_{\text{exp}}} P(E,T_1)dT_1 = \frac{P_0}{2}\ln\left(\frac{4t_{\text{exp}}}{T_{1,m}}\right). \tag{2.51}$$

2.3.3 Weak fields

The interaction of phonons or photons with two-level systems is the dominant source of scattering below 1 K. In the weak field limit, a rate equation approach similar to that used in the calculation of T_1^{-1} can be applied to determine the lifetime of the phonon or photon. In the case of an electric field, by taking into account the detailed balance between the energy lost by a photon and the energy absorbed by a TLS, the scattering or absorption rate can be written as

$$\tau_{ph}^{-1} = \frac{2\pi}{\hbar}|\langle\psi_1|H_{\text{int}}|\psi_2\rangle|^2\tanh(E/2k_BT), \tag{2.52}$$

where the $\tanh(E/2k_BT)$ factor is the difference in TLS state population in thermal equilibrium [65, 37]. In next section, we will see how this result is obtained in the weak field limit. It can be seen that if the thermal distribution of TLSs is one in which mostly the lower energy states are populated, absorption by TLSs will be maximal. To calculate τ_{ph}^{-1} for a photon, we used the amplitude of the electric field $\sqrt{\hbar\omega/2\epsilon}$, and the matrix element in equation (2.52) is

$$\langle\psi_1|H_{\text{int}}|\psi_2\rangle = p_0\sqrt{\frac{\hbar\omega}{2\epsilon}}\frac{\Delta_0}{E}. \tag{2.53}$$

It follows that the absorption rate becomes

$$\tau_{ph}^{-1}(\omega) = \frac{\pi p_0^2 \omega}{\epsilon} \frac{\Delta_0^2}{E^2} \tanh(E/2k_BT). \tag{2.54}$$

The total scattering at an energy $E = \hbar\omega$ is given by

$$\begin{aligned} T_{ph}^{-1}(E = \hbar\omega) &= \int_{-\infty}^{+\infty} d\Delta \int_{\Delta_0^{\min}}^{E=\hbar\omega} \frac{P_0}{\Delta_0} d\Delta_0 \tau_{ph}^{-1} \\ &= \frac{\pi p_0^2 \omega}{\epsilon} P_0 \tanh(\hbar\omega/2k_BT), \end{aligned} \tag{2.55}$$

where we have considered both positive and negative values of the asymmetry energy Δ, and $\Delta_0^{\min}$ can be set to zero since the integrand does not diverge. The inverse mean free path of the photon and the dimensionless Q-factor are defined as

$$l^{-1}(\omega) = \frac{T_{ph}^{-1}}{c} = \frac{\omega}{c} Q_{\text{TLS}}^{-1}. \tag{2.56}$$

From this definiton we recover equation (1.2)

$$Q_{\text{TLS}}^{-1}(\omega, T) = Q_0^{-1} \tanh(\hbar\omega/2k_BT) \tag{2.57}$$

where $Q_0^{-1} = \pi p_0^2 P_0/3\epsilon$ is the intrinsic dielectric loss tangent $\tan\delta_0$. The factor of 3 arises from averaging over all possible dipole orientations in an isotropic material.

2.4 Strong fields: The Bloch equations

The dynamics of a TLS in strong fields depends on the coherence between the two eigenfunctions ψ_1 and ψ_2. The time evolution of the occupation coefficients deduced from the time-dependent Schrödinger equation are

$$\dot{A}_1(t) = \frac{1}{i\hbar} \left[\langle\psi_1|H_{\text{int}}(t)|\psi_1\rangle A_1 + \langle\psi_1|H_{\text{int}}(t)|\psi_2\rangle A_2 e^{-i\omega_0 t} \right], \tag{2.58}$$

$$\dot{A}_2(t) = \frac{1}{i\hbar} \left[\langle\psi_2|H_{\text{int}}(t)|\psi_2\rangle A_2 + \langle\psi_2|H_{\text{int}}(t)|\psi_1\rangle A_1 e^{i\omega_0 t} \right]. \tag{2.59}$$

The dynamics can be naturally understood by recalling the spin-$\frac{1}{2}$ analogy for a TLS [24]. The full Hamiltonian reads

$$H = \frac{1}{2}E\sigma_z + \left|\frac{\Delta}{E}\sigma_z + \frac{\Delta_0}{E}\sigma_x\right| \boldsymbol{p}_0 \cdot \boldsymbol{\xi}(t). \tag{2.60}$$

By setting $\frac{1}{2}\boldsymbol{\sigma} \rightarrow \boldsymbol{S}$, and for the purpose of illustrating the analogy of a spin-$\frac{1}{2}$ in a magnetic field $\boldsymbol{B}$, we write the Hamiltonian as

$$H = -\hbar\eta \boldsymbol{B} \cdot \boldsymbol{S} = -\hbar\eta \boldsymbol{B}_0 \cdot \boldsymbol{S} - \hbar\eta \boldsymbol{B}(t) \cdot \boldsymbol{S}, \tag{2.61}$$

where $\boldsymbol{B}_0$ and $\boldsymbol{B}(t)$ are the static and oscillating components. Writing them explicitly in terms of the unperturbed TLS paramters and the components of the perturbing electric field gives

$$-\hbar\eta \boldsymbol{B}_0 = (0, 0, E), \tag{2.62}$$

$$-\hbar\eta \boldsymbol{B}(t) = 2\left(\frac{\Delta_0}{E}\boldsymbol{p}_0 \cdot \boldsymbol{\xi}(t), 0, \frac{\Delta}{E}\boldsymbol{p}_0 \cdot \boldsymbol{\xi}(t)\right) = (\boldsymbol{p}_x, 0, \boldsymbol{p}_z) \cdot \boldsymbol{\xi}(t). \tag{2.63}$$

The time evolution, ignoring relaxation and decoherence, is that of free spin precession,

$$\frac{d}{dt}\boldsymbol{S}(t) = \eta \boldsymbol{S}(t) \times \boldsymbol{B}. \tag{2.64}$$

In a physical ensemble there will be processes which give rise to longitudinal (T_1) and transverse (T_2) relaxation times. Accounting for this, we have the following set of coupled equations for the ensemble average of $\langle \boldsymbol{S}(t) \rangle$

$$\begin{aligned}
\frac{d}{dt}\langle S_x \rangle &= \eta\left(B_z\langle S_y\rangle - B_y\langle S_z\rangle\right) - \frac{\langle S_x\rangle}{T_2}, \\
\frac{d}{dt}\langle S_y \rangle &= \eta\left(B_x\langle S_z\rangle - B_z\langle S_x\rangle\right) - \frac{\langle S_y\rangle}{T_2}, \\
\frac{d}{dt}\langle S_z \rangle &= \eta\left(B_y\langle S_x\rangle - B_x\langle S_y\rangle\right) - \frac{\langle S_z\rangle - \langle S_z^{eq}\rangle}{T_1}.
\end{aligned} \tag{2.65}$$

These are the Bloch Equations of nuclear magnetic resonance [13]. In steady state, where variations in the field are slow compared to transitions rates, S_z^{eq}, the instantaneous equilibrium of a TLS, and is given by

$$S_z^{eq}(B_z(t)) = \frac{1}{2}\tanh(\hbar\eta B_z(t)/2k_BT). \tag{2.66}$$

Equation (2.66) reflects the effect of the field B_z on the thermal equilibrium distribution of the TLSs. Writing the static and time dependent fields together, we have

$$\boldsymbol{B} = \boldsymbol{B}_0 + 2\boldsymbol{B}' \cos(\omega t) = B_0\hat{\boldsymbol{z}} + (B_x\hat{\boldsymbol{x}} + B_z\hat{\boldsymbol{z}})\left(e^{i\omega t} + e^{-i\omega t}\right). \tag{2.67}$$

In the previous section, the field was sufficiently weak such that the TLS effectively remained in its unperturbed thermal equilibrium state. The steady state solutions ($\frac{d}{dt}\boldsymbol{S} = 0$) to (2.65) reflect the new thermal equilibrium of the ensemble under continuous driving due to $\boldsymbol{B}$. The Bloch equations can be solved analytically by assuming small departures from thermal equilibrium, i.e, linearizing (2.66), and using the Fourier series expansion solution

$$\langle \boldsymbol{S}(t) \rangle = \sum_{m=-\infty}^{\infty} \boldsymbol{S}_m e^{i\omega_m t}, \tag{2.68}$$

where $\omega_m = m\omega$. It can be shown that only $m = -1, 0, 1$ are required [34] to describe the behaviour near resonance. The system of equations is solved by introducing It is then found that the two components of the Fourier series needed to describe the system are

$$S_x(\omega) = -\frac{S_z^0}{2\hbar}\left(\frac{1}{\omega_0 - \omega + iT_2^{-1}} + \frac{1}{\omega_0 + \omega - iT_2^{-1}}\right)\hbar\eta B_x \equiv \chi_x(\omega)\hbar\eta B_x, \tag{2.69}$$

$$S_z(\omega) = \frac{dS_z^0}{d\,(\hbar\eta B_0)}\frac{1 - i\omega T_1}{1 + \omega^2 T_1^2}\hbar\eta B_x \equiv \chi_z(\omega)\hbar\eta B_z, \tag{2.70}$$

and

$$S_z^0(\omega) = \frac{1 + (\omega_0 - \omega)^2 T_2^2}{1 + (\eta B_x)^2 T_1 T_2 + (\omega_0 - \omega)^2 T_2^2} S_z^{eq}(B_0), \tag{2.71}$$

where we have defined the frequency-dependent susceptibility components χ_x and χ_z, and $\omega_0 = \eta B_0$. Equations (2.69) - (2.71) can mapped to our problem by applying the relation of (2.62) and (2.63). The response of a TLS to an external field is reflected in the dielectric susceptibility $\bar{\bar{\chi}}$, which has tensorial character in general. According to χ_x and χ_z, this happens in two ways. χ_x describes a resonant process which dominates in the regime where $\omega T_1 \gg 1$, and χ_z describes a relaxation process which only contributes for $\omega T_1 \leq 1$. We can define the components of $\bar{\bar{\chi}}$ in terms of their contributions to the permanent and transition dipole moments from (2.63), $\boldsymbol{p_z}$ and $\boldsymbol{p_x}$. As a result of the electric field $\boldsymbol{\xi}$, the average dipole moments are given by the

following [24, 34]:

$$\langle \boldsymbol{p}_x \rangle = \bar{\bar{\chi}}_x(\omega) \cdot \boldsymbol{\xi}, \tag{2.72}$$

$$\langle \boldsymbol{p}_z \rangle = \bar{\bar{\chi}}_z(\omega) \cdot \boldsymbol{\xi}, \tag{2.73}$$

where $\bar{\bar{\chi}}_x$ and $\bar{\bar{\chi}}_x$ are found from (2.69) - (2.71) to be

$$\bar{\bar{\chi}}_x(\omega) = -\frac{\sigma_z^0}{\hbar}\left(\frac{1}{\omega_0 - \omega + iT_2^{-1}} + \frac{1}{\omega_0 + \omega - iT_2^{-1}}\right)\boldsymbol{p}_x\boldsymbol{p}_x, \tag{2.74}$$

$$\bar{\bar{\chi}}_z(\omega) = -\frac{d\sigma_z^0}{dE}\left(\frac{1 - i\omega T_1}{1 + \omega^2 T_1^2}\right)\boldsymbol{p}_z\boldsymbol{p}_z, \tag{2.75}$$

where

$$\sigma_z^0(E) = \frac{1 + (\omega_0 - \omega)^2 T_2^2}{1 + \Omega_R^2 T_1 T_2 + (\omega_0 - \omega)^2 T_2^2}\sigma_z^{eq}(E), \text{with} \tag{2.76}$$

$$\sigma_z^{eq}(E) = -\tanh(E/2k_B T). \tag{2.77}$$

We have introduced the $\Omega_R = 2\boldsymbol{p}_x \cdot \boldsymbol{\xi}/\hbar$ as the Rabi frequency of the TLS. In terms of the Bloch model, T_1 and T_2 are typically taken as phenomenological relaxation times. In our case, T_1 is the same as that discussed in section 2.2.2, and is due to coupling to the phonon bath. The origin of T_2 is more complicated as it depends on the mutual interaction between TLSs, and will be discussed in a later section.

2.4.1 Complex dielectric permitivitty

When considering measurements of dielectric loss using superconducting resonators, frequencies on the order of 10^9 GHz and temperatures $T < 1$ K are typical. In this regime, the effect of the TLS on the dielectric constant is entirely due to resonant absorption, $\bar{\bar{\chi}}_x(\omega)$. The relaxation regime, where $\omega < T_1^{-1}$ presents interesting physics [37], but the analytical treatment is beyond the context of this thesis and need not be considered to understand our measurements (see chapter 6). The contribution to the complex dielectric constant due to $\bar{\bar{\chi}}_x(\omega)$ is found by integrating over the TLS parameters. We have [24, 62]

$$\epsilon_{\text{TLS}}(\omega) = \epsilon'(\omega) - i\epsilon''(\omega) = \iiint d\Delta d\Delta_0 d\hat{\boldsymbol{p}} \frac{P_0}{\Delta_0}\hat{\boldsymbol{p}} \cdot \bar{\bar{\chi}}_x(\omega) \cdot \hat{\boldsymbol{p}}, \tag{2.78}$$

where $\int d\hat{\boldsymbol{p}}$ is over dipole orientations. This expression can be simplified by making the variable substitution $x = \Delta_0/E$ where $E^2 = \Delta^2 + \Delta_0^2$. It follows that [24]

$$\int_0^{\Delta_{\max}} \int_{\Delta_{0,\min}}^{\Delta_{0,\max}} \frac{P_0}{\Delta_0} d\Delta_0 d\Delta \to P_0 \int_0^{E_{\max}} \int_{x_{\min}}^{1} \frac{x}{\sqrt{1-x^2}} dx dE. \tag{2.79}$$

Including the angular component of the dipole orientation, the integral becomes

$$\epsilon_{\text{TLS}}(\omega) = P_0 p_0^2 \int_0^{E_{\max}} dE \int_{x_{\min}}^{1} \frac{x}{\sqrt{1-x^2}} dx \int_0^{\pi/2} \cos^2\theta \sin\theta d\theta \tag{2.80}$$

$$\times \left[\tanh\left(\frac{E}{2k_B T}\right) \frac{1 + (E/\hbar - \omega)^2 T_2^2}{1 + \Omega_R^2 T_1 T_2 + (E/\hbar - \omega)^2 T_2^2} \mathcal{G}(E) \right] \tag{2.81}$$

By observing that

$$\Omega_R^2 T_1 = \left(\frac{2p_0 |\boldsymbol{\xi}| \cos\theta}{\hbar} \frac{\Delta_0}{E} \right)^2 \times T_{1,m} \left(\frac{E}{\Delta_0} \right)^2 = 4 p_0^2 |\boldsymbol{\xi}|^2 \cos^2\theta T_{1,m}/\hbar^2, \tag{2.82}$$

has a dependence on θ but not x, the integral over x is approximately $\int_{x_{\min}}^{1} \frac{x}{\sqrt{1-x^2}} dx \simeq 1$. The integral over θ is of the form $\int_0^1 \frac{z^2}{a^2 z^2 + 1} dz = \frac{a - \arctan(a)}{a^3} \sim \frac{1}{3} \frac{1}{a^2/3+1}$, where $a = \hbar^{-2} 2 p_0^2 \xi^2 T_{1,m}(E)/(1 + (E/\hbar - \omega)^2 T_2^2)$. Using these results the integral over E is

$$\epsilon_{\text{TLS}}(\omega) = \frac{P_0 p_0^2}{3} \int_0^{E_{\max}} dE \tanh(E/2k_B T) \mathcal{L}(E, \tilde{\Omega}_R(\xi)) \mathcal{G}(E), \tag{2.83}$$

where

$$\mathcal{L}(E, \tilde{\Omega}_R(\xi)) = \frac{\sigma_z^0(E, \tilde{\Omega}_R(\xi))}{\sigma_z^{eq}(E)} = \frac{1 + (E/\hbar - \omega)^2 T_2^2}{1 + \tilde{\Omega}_R^2(\xi) T_1 T_2 + (E/\hbar - \omega)^2 T_2^2}, \tag{2.84}$$

$$\mathcal{G}(E) = \mathcal{G}_-(E) + \mathcal{G}_+(E) = \frac{1}{E/\hbar - \omega + jT_2^{-1}} + \frac{1}{E/\hbar + \omega - jT_2^{-1}}. \tag{2.85}$$

Above, $\tilde{\Omega}_R$ is the effective Rabi frequency given by

$$\tilde{\Omega}_R(\xi) = \frac{2p_0 \xi}{\sqrt{3}\hbar} \frac{\Delta_0}{E}, \tag{2.86}$$

where the factor of $\sqrt{3}$ arises from the integral over dipole configurations. In the weak field limit, $\mathcal{L}(E, \tilde{\Omega}_R(\xi \to 0)) \to 1$, the dielectric constant as a function of temperature is given by: [65]

$$\epsilon_{\mathrm{TLS}}(\omega) = -\frac{2P_0 p_0^2}{3}\left(\mathcal{D}\left(\frac{1}{2} - \frac{\hbar\omega - j\hbar T_2^{-1}}{2\pi j k_B T}\right) - \ln\left(\frac{E_{\max}}{2\pi k_B T}\right)\right), \tag{2.87}$$

where $\mathcal{D}$ is the complex digamma function. Furthermore, it follows in a similar manner that the relative shift in the dielectric constant as a function of temperature is

$$\mathrm{Re}\frac{\epsilon_{\mathrm{TLS}}(T)}{\epsilon_{\mathrm{TLS}}(T_0)} = 1 + \frac{2\pi P_0 p_0^2}{3\epsilon}\left(\mathrm{Re}\mathcal{D}\left(\frac{1}{2} - \frac{\hbar\omega}{2\pi j k_B T}\right) - \ln\left(\frac{\hbar\omega}{2\pi k_B T}\right)\right), \tag{2.88}$$

where $\epsilon_{\mathrm{TLS}}(T_0)$ is a reference value at temperature T_0. The loss tangent can be found by noting that the main contribution to the imaginary part of the integral in (2.81) is due to the resonant absorption from TLS. Therefore the second term in $\mathcal{G}(E)$ can be ignored and the loss tangent becomes

$$\begin{aligned}
\frac{\mathrm{Im}[\epsilon_{\mathrm{TLS}}(\omega)]}{\epsilon} &= \frac{P_0 p_0^2}{3\epsilon}\int_0^{E_{\max}} dE \tanh(E/2k_B T)\mathrm{Im}[\mathcal{G}_-(E)] \\
&= \frac{P_0 p_0^2}{3\epsilon}\int_0^{E_{\max}} dE \tanh(E/2k_B T)\frac{-T_2^{-1}}{(E/\hbar - \omega)^2 + \left(T_2^{-1}\right)^2} \\
&\simeq -\frac{P_0 p_0^2}{3\epsilon}\int_0^{E_{\max}} dE \tanh(E/2k_B T)\pi\delta(E - \hbar\omega)
\end{aligned} \tag{2.89}$$

where we have assumed the linewidth of the Lorenztian to be sharply peaked at $E/\hbar$. This is generally believed to be valid in the resonant regime since $\omega \gg T_2^{-1}$. It then follows that we recover equation (2.57)

$$Q_{\mathrm{TLS}}^{-1}(\omega, T) = Q_0^{-1}\tanh(\hbar\omega/2k_B T). \tag{2.90}$$

For the case of a strong electric field, again we can neglect $\mathcal{G}_+(E)$ in the integral, since it describes a relaxation-like process the contribution from which is small. The imaginary part of ϵ takes the

form

$$\begin{aligned}\frac{\mathrm{Im}[\epsilon_{\mathrm{TLS}}(\omega)]}{\epsilon} &= \frac{P_0 p_0^2}{3\epsilon}\int_0^{E_{\max}} dE\tanh(E/2k_BT)\mathcal{L}(E,\tilde{\Omega}_R(\xi))\mathrm{Im}[\mathcal{G}_-(E)], \\ &= \frac{P_0 p_0^2}{3\epsilon}\int_0^{E_{\max}} dE\tanh(E/2k_BT)\frac{-T_2^{-1}}{(E/\hbar-\omega)^2+\left(T_2^{-1}\sqrt{1+\tilde{\Omega}_R^2(\xi)T_1T_2}\right)^2},\end{aligned} \tag{2.91}$$

which is similar to (2.89) but now the width of the Lorentzian is $T_2^{-1}\sqrt{1+\tilde{\Omega}_R^2(\xi)T_1T_2}$ and the integral is, to a good approximation, given by

$$\frac{\mathrm{Im}[\epsilon_{\mathrm{TLS}}(\omega)]}{\epsilon} \simeq -\frac{\pi P_0 p_0^2}{3\epsilon}\frac{\tanh(\hbar\omega/2k_BT)}{\sqrt{1+\tilde{\Omega}_R^2(\xi)T_1T_2}}. \tag{2.92}$$

This is one of the central results of the TLS model. It reflects the non-linear dependence of the loss tangent on the strength of the applied electric field ξ. Expressing in terms of the inverse Q-factor, we have

$$Q_{\mathrm{TLS}}^{-1}(\omega,T,\xi) = Q_0^{-1}\frac{\tanh(\hbar\omega/2k_BT)}{\sqrt{1+(\xi/\xi_c)^2}}, \tag{2.93}$$

where ξ_c is the critical saturation field given by

$$\xi_c = \frac{\sqrt{3}\hbar}{2p_0}\frac{\Delta_0}{\hbar\omega}\frac{1}{\sqrt{T_1T_2}} = \frac{\sqrt{3}\hbar}{2p_0\sqrt{T_{1,m}T_2}}. \tag{2.94}$$

The effect of saturation was one of the first indications of the existence of two-level systems [36]. It was observed both in acoustic and electric cases but was difficult to probe reliably over large temperature ranges and required very small fields to detect. Measuring the critical saturation field over a large temperature range would provide an indirect measure of the ensemble T_1 and T_2. Many experiments [29, 30, 66] were conducted in the 1970's and 80's using acoustic pulses to measure T_1 and T_2. In many cases the steady state solutions to the Bloch equations were are not valid since the duration of the pulse was less than T_1 and T_2. Experimental evidence strongly supports the assumption that T_1 is due primarily to phonon relaxation [65], as outlined in section 2.2.2. T_2, however, was found to be much less than T_1. Therefore, T_2^{-1} was not limited by relaxation and suggested the existence of other sources of dephasing [40, 10] . In general, T_2

can be written as [65]

$$T_2^{-1} = \tfrac{1}{2}T_1^{-1} + T_\phi^{-1}, \tag{2.95}$$

where T_ϕ^{-1} is due to contributions from sources of pure dephasing.

2.4.2 TLS-TLS interactions

The small value of T_2 is a result of broadening of the TLS spectral line width [10, 33, 45]. Recalling the spin-$\frac{1}{2}$ picture [34], the Hamiltonian of the non-interacting TLS ensemble is

$$H = -\sum_i E_i S_z^i - \sum_i \left(\mu_i \xi_i S_x^i + \tilde{\mu}_i \xi_i S_z^i + D_i e_i S_x^i + B_i e_i S_z^i\right), \tag{2.96}$$

where a TLS of energy $E_i = \sqrt{\Delta_i^2 + \Delta_{0,i}^2}$ experiences an electric field ξ_i and a strain field e_i. The prefactors $\tilde{\mu}_i, \mu_i, D_i$ and B_i are coupling constants. The interaction between TLSs is a difficult problem to address since in an amorphous material there is no simple relationship between the axes of phase space (S_x^i, S_z^i) and real space. One can write down a Hamiltonian which takes a form analogous to a spin-spin Hamiltonian. It is given by

$$H_{\text{TLS-TLS}} = \sum_{i>j} J_{ij} S_z^i S_z^j, \tag{2.97}$$

$$J_{ij} = \frac{C_{ij}}{r_{ij}^3} \frac{\Delta_i}{E_i} \frac{\Delta_j}{E_j}, \tag{2.98}$$

where C_{ij} is a coupling tensor. Forms of C_{ij} can be worked out for the case of an isotropic material [10, 40]. The effect of the mutual interaction can be illustrated in the following way [10]: Consider a subset of the TLS ensemble which is resonant with the applied field (r-TLS), and also a subset which is undergoing random thermal transitions as a result of the interaction with the phonon field (t-TLS). The effect of the random transitions of a t-TLS will be to cause fluctuations in the phonon field, which are in turn felt by the r-TLS. This effect leads to broadening of the spectral profile of the r-TLS. The theory of *spectral diffusion* predicts a temperature dependence of T_ϕ^{-1} which varies as $\sim T^2$, and explains much of the experimental data. It is unclear to what extent spectral diffusion plays a role in the steady-state regime and at higher temperatures towards 1 K as it lacks experimental support. The general belief is that the relaxation rate due to phonons grows quickly and dominates over processes which contribute to T_ϕ^{-1}, but this has

not been clearly observed in experiments.

2.5 Limitations of the TLS model

The tunnelling two-level system model provides an adequate description of the experimental data on the low temperature properties of amorphous dielectrics. The assumptions concerning the distribution of TLSs and their energy level structure are necessary insofar as they yield a relatively straightforward set of predictions. Despite the success of the model, there remain some open problems. The obvious first problem is specifically the nature of the microscopic entity which assumes the role of the TLS. There are clear instances where the microscopic TLS is known, but in general it remains a phenomenological construct. Moreover, given the broad range of materials to which the model is applied, from basic amorphous oxides to complex polymer solutions, a clear microscopic picture remains ambiguous. This ties into the second main issue with the model. There is a striking universality in the acoustic version of the intrinsic inverse Q-factor, $Q_0^{-1} = \pi\gamma_0^2 P_0/2\rho v^2$. Q_0^{-1} reflects the ratio of the phonon wavelength λ to its mean free path l, as seen in equation (2.56). This dimensionless number tends towards a value of $\sim 3 \times 10^{-4}$ in nearly all amorphous dielectrics, and is very difficult to explain within the framework of the TLS model. It is *possible* that the factors in the definition of Q_0^{-1} can be such that this number is obtained, however, they are believed to be independent of each other and unique to a particular material. Thus, it is very difficult to account for this universality in terms of the TLS model without the invocation of a truly extraordinary degree of coincidence. In the case of an electric field, such a universality in Q_0^{-1} for a *photon* has not been observed. This could be due to the different propagation characteristics of electromagnetic waves compared to ultrasonic waves. Electromagnetic waves at GHz frequencies have wavelengths on the order of mm, but for an ultrasonic wave this is only $\sim$ 100 nm. Many have suggested that the nature of the universality can only arise from long range interactions which scale as r^{-3}. The theory of spectral diffusion explains qualitatively the temperature dependence of the coherent properties of TLSs, but a complete treatment of the mutual interaction remains an open problem. Some works have considered a particular type of mutual interaction in terms of virtual phonon exchange [80, 40] induced by the driving field itself. This is quite challenging and depends on both wavelength and the convergence of a many-body Hamiltonian normalization procedure. Therefore, a first principle theory concerning amorphous solids that remains general at the microscopic level, remains unconquered ground in condensed

matter physics.

It has been suggested [48] that a "smoking-gun" validation of the TLS model lies in an extensive measurement of the temperature dependence of the intrinsic loss tangent $Q_i^{-1}(\omega, T) = Q_0^{-1} \tanh(\hbar\omega/2k_BT)$ which explores its full functional range. Furthermore, ensemble measurements of relaxation and dephasing over a large temperature range using electric fields have not been performed using superconducting resonators. The first measurement probes the TLS density of states and specifically its two-level character in thermal equilibrium. The second measures coherent effects of the TLS, namely, phonon relaxation and dephasing mechanisms induced by mutually interacting TLSs, the origin of which is not well understood as $T \to 1$ K.

Chapter 3

Experimental methods

3.1 Circuit model of a lumped element resonator

The remainder of the work presented in this section is a summary of the work in reference [18]. Extraction of the internal Q-factor of a superconducting resonator depends on the details of how it is coupled to microwave signals. A resonator will lose energy both by internal losses, Q_i^{-1}, and its coupling to an external circuit, described by the quality factor Q_e^{-1}. The inverse of the total Q-factor is given generally by

$$Q^{-1} = Q_i^{-1} + Q_e^{-1}. \tag{3.1}$$

The internal quality factor, Q_i^{-1}, is the quantity of interest in terms of dielectric loss, and this chapter will outline a robust method for the extraction of Q_i^{-1} from transmission measurements of a lumped element resonator [18]. Lumped element resonators were the focus of this work because their parameters can be easily varied to achieve different device designs, all of which can be understood in terms of our model.

In our devices, the resonator is formed by a capacitor C_0 and an inductor L, as illustrated in Fig. 3.1a). The resonator is coupled to a coplanar waveguide of characteristic impedance Z_0 by a mutual inductance M and a capacitance C_c. The mutual inductance is $M = k\sqrt{LL_1}$ where L_1 is the inductance of the line which coupled to the resonator and k is a coupling factor which can be no greater than unity. A resistance R is necessary for the definition of the internal Q-factor for a lumped element resonator, $Q_i = \omega_0 RC_0$ [68], where ω_0 is the resonance frequency. Figure 3.1

b) shows an equivalent network circuit for the case where we have perfect impedance matching ($Z = 50\ \Omega$) between the coaxial lines coming from the voltage source and the coplanar waveguide on the device.

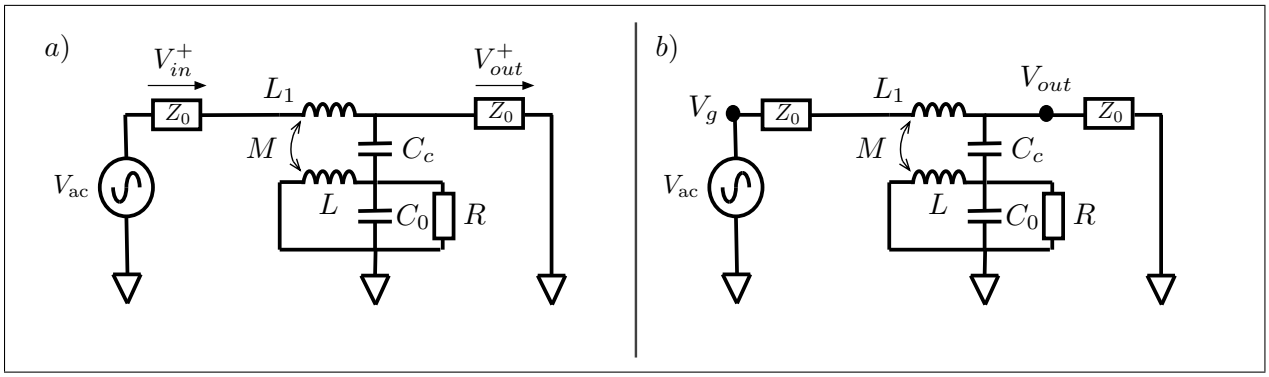

Figure 3.1: a) Lumped element circuit model for a resonator of inductance L and capacitance C_0 coupled to a transmission line of impedance Z_0. The input voltage from the experimental setup is V_{in}^+ and the measured output voltage is V_{out}^+ b) An equivalent network model for the circuit in a) where $V_g = 2V_{in}^+$, $V_{out} = V_{out}^+$ and V is the voltage on the capacitor.

The microwave response function of the resonator $S_{21}(\omega) = V_{out}^+/V_{in}^+$ is the central quantity of interest. It is also known as a scattering parameter for a 2-port microwave network. By applying Kirchoff's laws to the circuit in Fig. 3.1, we obtain

$$S_{21}(\omega) = \frac{2 + \frac{V}{V_{in}^+}\left(j\omega C_c Z_{in}^+ + M/L\right)}{1 + Z'_{in}/Z_0 + j\omega C_c Z'_{in}}, \tag{3.2}$$

where V/V_{in}^+, a quantity which will be of interest later when interpreting electric field dependent quantities, is given by

$$\frac{V}{V_{in}^+} = -2\frac{M/L - j\omega C_c Z'_{out}}{Z'_{out} + Z'_{in}} \Bigg/ \left(\frac{1}{j\omega L} + \frac{1}{Z_C} + \frac{j\omega C_c}{j\omega C_c Z_0 + 1} + \frac{(M/L - j\omega C_c Z'_{out})^2}{Z'_{out} + Z'_{in}}\right). \tag{3.3}$$

In equations (3.2) and (3.3) we have simplified the expression by using the following impedance

definitions:

$$Z'_{in} = Z_0 + j\omega L_1 - j\omega M^2/L, \tag{3.4}$$

$$Z'_{out} = \frac{Z_0}{1 + j\omega C_c Z_0}, \tag{3.5}$$

$$Z_C = \frac{1}{j\omega C_0 + 1/R}. \tag{3.6}$$

The response function, $S_{21}(\omega)$ is a complicated complex expression which depends on all components of the circuit. Generally, we can assume the response is of the form

$$R(\omega) = R_0 \frac{\prod_{i=0}^{n-1}(\omega - z_i)}{\prod_{j=0}^{m-1}(\omega - p_j)} = \frac{N(\omega)}{D(\omega)}, \tag{3.7}$$

where R_0 is a constant factor and $N(\omega)$ and $D(\omega)$ are polynomial functions of order n and m with zeroes z_i and poles p_j respectively which depend on the details of the circuit. We are interested in the behaviour of S_{21} in the vicinity of the resonance ω'_0, where it will be approximately given by a Lorentzian, whose profile and asymmetry is governed primarily by the closest poles p_0 and zeroes z_0 from equation (3.7). We have

$$R(\omega) \simeq \frac{\tilde{N}(\omega)}{\tilde{D}(\omega)} \frac{\omega - z_0}{\omega - p_0}, \tag{3.8}$$

where $\tilde{N}(\omega)$ and $\tilde{D}(\omega)$ are polynomial functions with zeroes and poles $p_{j\neq 0}$ and $z_{i\neq 0}$ respectively. The closest pole p_0 and zero z_0 of the response function define the resonance, ω'_0. For a high-Q superconducting resonator, in the vicinity of resonance, $\omega'_0 - \delta\omega \leq \omega'_0 \leq \omega'_0 + \delta\omega$, where $\delta\omega = \omega'_0/Q$, $\tilde{N}(\omega)$ and $\tilde{D}(\omega)$ are well approximated by their on-resonance values. Therefore we can write the effective response function as

$$\tilde{R}(\omega) \simeq \frac{\tilde{N}(\omega'_0)}{\tilde{D}(\omega'_0)} \frac{\omega - z_0}{\omega - p_0}. \tag{3.9}$$

3.1.1 Reduction of transmission amplitude to linear fractional form

To connect the response function to a transmission measurement which is to be fit by a simple expression, we must approximate equation (3.2) in the form of equation (3.9). To aid this process,

it is natural and useful to define the following set of dimensionless parameters:

$$\begin{aligned} \alpha &= M/L, \quad \beta = L_1/L, \quad \gamma = C_c/C_0, \quad \xi = \sqrt{LC_0}/Z_0, \\ q &= Q_i^{-1} = 1/\omega_0' RC_0, \quad x = 2\omega_0' RC_0 = \tfrac{2}{q}\left(\tfrac{\omega}{\omega_0'} - 1\right). \end{aligned} \tag{3.10}$$

In equation (3.10), we have chosen $\omega_0' = 1/\sqrt{LC_0}$ as the resonant frequency of the *uncoupled* resonator. Straightforward factorization yields

$$S_{21} = \frac{f(qx)}{g(qx)} = \frac{\sum_{n=0} a_n (qx)^n}{\sum_{n=0} b_n (qx)^n}. \tag{3.11}$$

The choice of q in (3.10) ensures that qx is much smaller than the other dimensionless parameters and the coefficients a_n and b_n. Thus, to a very good approximation the reduced S_{21} response function is given by terms up to first order in qx

$$\tilde{S}_{21} = \frac{\tilde{f}(qx)}{\tilde{g}(qx)} = \frac{a_0 + a_1 qx}{b_0 + b_1 qx}, \tag{3.12}$$

where the coefficients a_0, a_1, b_0 and b_1 depend on the dimensionless circuit parameters and are independent of qx. This allows equation (3.12) to be rearranged and written as

$$\tilde{S}_{21} = |A_0| e^{j\phi} \frac{a + jx}{b + jx} = |A_0| e^{j\phi} \frac{A + j\frac{B}{q} + jx}{C + \frac{D}{q} + j\left(E + \frac{F}{q}\right) + jx}, \tag{3.13}$$

where $a = \frac{ja_0}{qa_1}$, $b = \frac{jb_0}{qb_1}$, $|A_0|e^{j\phi} = \frac{a_1}{b_1}$ and we use the imaginary unit $j = \sqrt{-1}$ which is conventional in electrical engineering. The factor $|A_0|e^{j\phi}$ is of order unity and doesn't affect the profile of $\tilde{S}_{21}$ other than by scaling its magnitude. This factor can be viewed as a magnitude factor which would be difficult to distinguish from attenuation and amplification factors in the experimental setup. Based on this, and the fact that we do not lose useful parameters, it is reasonable to ignore this term. Furthermore, based on the expansions of A, B, C, D, E and F in terms of the parameters in equation (3.10), it can be shown that the reduced $\tilde{S}_{21}$ expression is very well approximated by

$$\tilde{S}_{21} = \frac{1 + j\frac{B}{q} + jx}{1 + \frac{D}{q} + j\frac{F}{q} + jx}. \tag{3.14}$$

The actual resonance frequency, ω_0, is different than ω_0' of the uncoupled resonator due to the coupling to the external circuit. The true resonance, ω_0, is found by minimizing equation (3.14). It is easily found that $\omega_0 = \omega_0'(1 - B/2)$, with B given by

$$B = \frac{\gamma(1-\alpha)}{1+\gamma-\alpha\gamma}. \tag{3.15}$$

From the definition of the internal quality factor, it follows that

$$Q_i = \omega_0 R C_0 = \omega_0' \left(1 - B/2\right) R C_0. \tag{3.16}$$

For completeness we include the approximate expressions for D and F. Their respective series expansions are given by

$$D = \frac{2+\beta\xi^2+\beta^2\xi^2}{\xi\left(4+\beta^2\xi^2\right)}\gamma^2 + \frac{2\xi}{4+\beta^2\xi^2}\left(\alpha^2 - \beta\alpha\gamma\right) + \ldots \tag{3.17}$$

$$F = \gamma + \frac{-8+2\beta-\xi\beta^2\xi^2}{2\left(4+\beta^2\xi^2\right)}\gamma - \frac{4\gamma\alpha+\beta\xi^2\alpha^2}{4+\beta^2\xi^2} + \ldots \tag{3.18}$$

Re-writing equation (3.14) explicitly as a function of frequency in terms of the true resonance and internal quality factor yields

$$\tilde{S}_{21}(\omega) = \frac{1 + 2jQ_i\frac{\omega-\omega_0}{\omega_0}}{1 + \frac{Q_i}{Q_e} + j\frac{Q_i}{Q_\alpha} + 2jQ_i\frac{\omega-\omega_0}{\omega_0}}. \tag{3.19}$$

Equation (3.17) takes the form of a modified Lorentzian, where Q_e is a free parameter and Q_α is a parameter which partially describes the asymmetry of the response as a result of the coupling. They are given by

$$Q_e = \frac{1 - B/2}{D} \tag{3.20}$$

and

$$Q_\alpha = \frac{1 - B/2}{F - B}. \tag{3.21}$$

In the limit where Q_α is very large compared to Q_i and Q_e, the width of $\tilde{S}_{21}(\omega)$ is equal to

$\omega_0(Q_i^{-1} + Q_e^{-1})$ where Q_e is the external quality factor.

3.1.2 Determination of the AC capacitor voltage in dielectric loss measurements

The expression given by equation (3.3) is also a function of the form given by equation (3.7). Therefore, we can make a similar systematic approximation of the function by expanding in terms of qx and the reduced dimensionless parameters from (3.10). We introduce the reduced voltage function

$$\tilde{v} = \frac{\tilde{f}_v}{\tilde{g}_v} = \frac{V}{V_{in}^+} = \zeta \frac{\frac{K}{q} + j\frac{J}{q} + jx}{H + \frac{N}{q} + j\left(O + \frac{P}{q}\right) + jx}. \tag{3.22}$$

Conveniently, the parameters in equation (3.22) are related to those in equation (3.13). We have $H = C, N = D, O = E$ and $P = F$, which, in turn, allows for equation (3.22) to be expressed in terms of the parameters in equation (3.19), Q_i, Q_e, Q_α and ω_0. Since these parameters are extracted from the behaviour of the response near resonance, we can therefore determine the voltage at resonance by evaluating $v(\omega_0)$. This yields the following expression

$$\tilde{v}(\omega_0) \simeq \frac{\lambda}{Q_i^{-1} + Q_e^{-1} + jQ_\alpha^{-1}}, \tag{3.23}$$

where

$$\lambda = \zeta \frac{K + j(J - B)}{1 - B/2}. \tag{3.24}$$

By performing a series expansion of λ, equation (3.24) can expressed in terms of the physical circuit parameters approximately as

$$\lambda \simeq -\frac{M}{Z_0}\omega_0 + j\frac{C_c}{C_0}. \tag{3.25}$$

The circuit parameters in equation (3.25) must be estimated in order to complete the analysis. Z_0 is typically designed to be 50 Ω and ω_0 is determined directly from measurements. The remaining parameters M, C_0 and C_c must be estimated using numerical simulations. Estimation of these parameters will be discussed in section 3.2.1. The ability to reliably determine the capacitor voltage is important for the analysis of dielectric loss. As described in chapter 2, the loss depends on the strength of the electric field, and therefore also the capacitor voltage of the resonator.

Equation (3.23) reflects the fact that V, the capacitor voltage, depends on the input voltage, V_{in}^{+}, and $Q_i^{-1}(V)$, which is itself dependent on V. This means there's a non-linear dependence of V on V_{in}^{+} and Q_i^{-1}. This presents a complication in the interpretation of voltage dependent dielectric loss measurements. This complication is illustrated by recalling the form of equation (2.93). For a homogeneous electric field in a simple parallel plate capacitor, the voltage dependence of the loss at a constant temperature in the TLS model is given by

$$Q_{\mathrm{TLS}}^{-1}(V) = Q_i^{-1}(\omega, T) \Big/ \sqrt{1 + (V/V_c)^2}, \tag{3.26}$$

where V_c is now the critical voltage. A typical experiment will involve measurements of the resonator at various microwave powers. At each excitation voltage, the amplitude and phase of the microwave response is fit to equation (3.19) and the result will yield a data set (Q_i, V_{in}^{+}). Equations (3.23) and (3.25) are then used in the transformation $(Q_i, V_{in}^{+}) \rightarrow (Q_i, V)$. This transformation yields a data set for which a one-to-one comparison with equation (3.26) can be made. Specifically, this "correction" to loss as a function of voltage V transforms the data set to one for which the TLS model predicts exactly equation (3.26). Therefore, any disagreement would be suggestive of behaviour not predicted by the model. In the over-coupled limit, $Q_e \ll Q_i$ and the scaling between V_{in}^{+} and V is linear and the transformation doesn't significantly affect the quality of the fits. It is also important to note that this transformation ensures that the fit parameter V_c and, equivalently, the critical field E_c, is physically more meaningful with respect to its predicted behaviour according to the TLS model.

In Fig. 3.2, we show data from measurements of an interdigital resonator with a resonance frequency at 5.9545 GHz as an example to illustrate the voltage transformation and also the fitting of the microwave response. The device is fabricated from Aluminum and has 100 nm of ALD Al_2O_3 oxide deposited on the surface of the resonator. The mutual inductance for this resonator was computed to be ~ 12 pH.

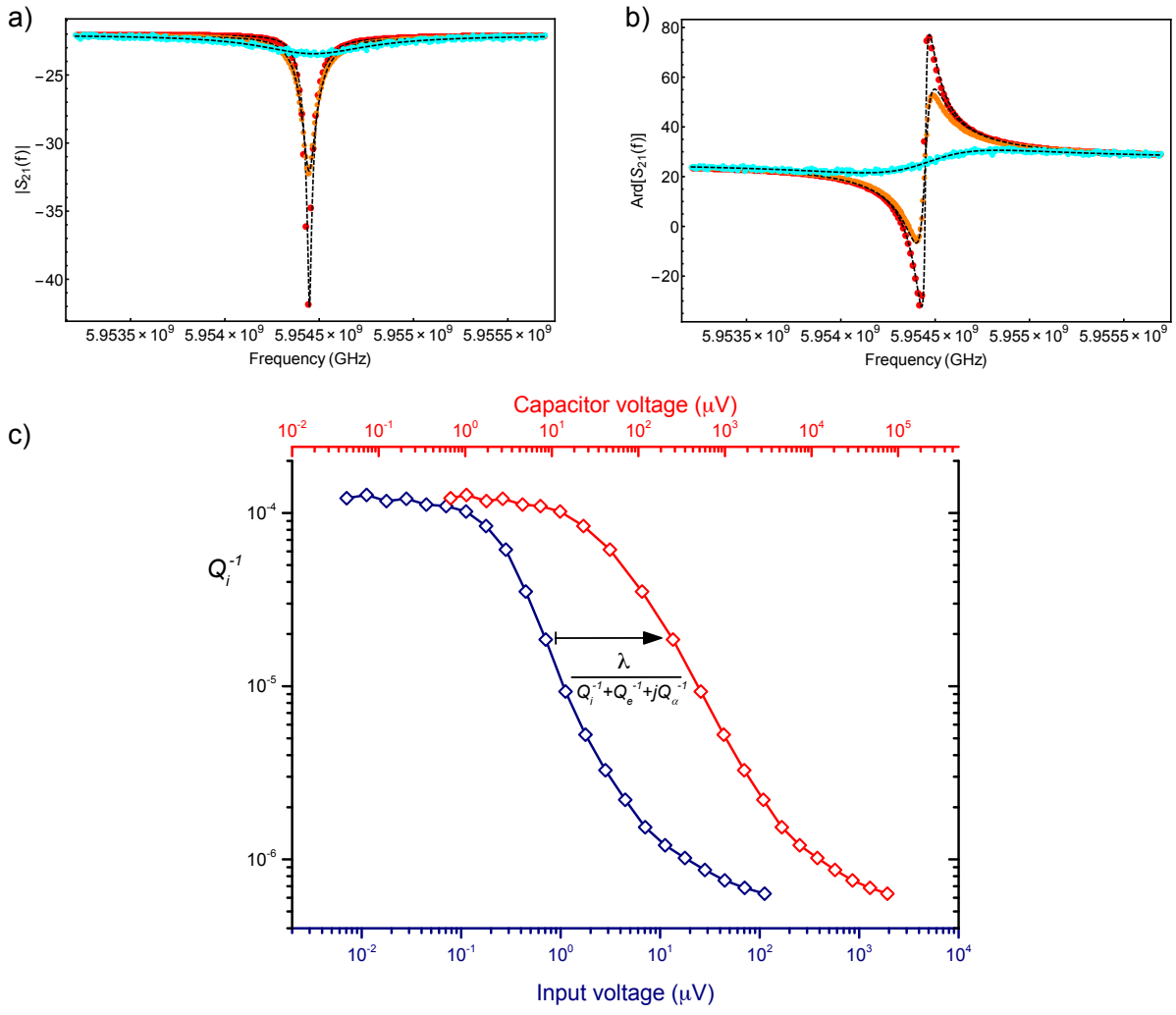

Figure 3.2: a) S_{21} magnitude and phase (b) of microwave response data acquired from a VNA at various powers illustrating the change in the internal quality factor as a function of power and the quality of the fits to equation (3.19). c) Example of microwave dielectric loss measurement at various input powers: Plot of loss versus input and capacitor voltage for an aluminum interdigital resonator with a resonance frequency of 5.9545 GHz. The blue data points are plotted as a function of the input voltage at the device, and the red points represent the transformed loss data as a function of the voltage on the capacitor.

3.2 Microwave simulation of a superconducting resonator

Prior to fabrication and measurement, prospective designs of the resonators are simulated using microwave simulation software packages. This step is important as it provides a reliable estimate of the resonance frequency and other circuit parameters which are needed in a complete analysis. Furthermore, it provides a reference when measuring a real device, and aids in the troubleshooting of faulty samples. A typical design of a superconducting resonator device involves the making of a technical CAD drawing which is to be used as a template during microfabrication. However, before converging on a design for fabrication, relevant circuit and microwave parameters need to be estimated and refined to meet the specific needs of the experiment. This steps involves making CAD designs which are simulated numerically to estimate the resonance frequency, external quality factor and specific circuit parameters. For the lumped element resonators measured in our experiments, the frequency was varied by changing the geometry of the inductive and capacitive circuit elements accordingly. In case of distributed half-wavelength or quarter-wavelength transmission line resonators, the frequency is adjusted simply by varying the length of the transmssion line, and the external quality factor is tuned by adjusting the length of the coupling arm which is coupled to the microwave feed line.

The software primarily used for microwave simulation is HFSS [2] from Ansys Electromagnetics. HFSS stands for high frequency structure simulator and it is a fully 3-dimensional finite element method (FEM) simulator that computes the solutions to Maxwell's equations subject to a set of boundary conditions. The solution is determined a points in space corresponding to a mesh, which consists of many tetrahedra elements. At each apex and edge of the tetrahedra, HFSS will solve for the electromagnetic quantities and also their gradients. From theses solutions, it computes the terminal S-matrix parameters for an n-port network in addition to many other useful quantities. A basic model design in HFSS will consist of boundaries and excitation ports to which the structure of interest is connected. The ports are necessary to compute the S-parameters which are equivalent to a VNA network measurement in a real experiment. The metal can be simply defined as a perfect electrical conductor, in which the conductivity is assigned the highest possible numerical allowed by the HFSS solver ($\sim 10^{30}$ siemens). A more complete picture is one which takes into account the complex nature of the conductivity of a superconductor at microwave frequencies. This subtle feature will affect the microwave properties, the electric field distribution and also the frequency of the resonator.

3.2.1 The surface impedance of a superconductor

At non-zero frequencies, a superconductor will develop a complex conductivity $\sigma(\omega) = \sigma_1(\omega) - j\sigma_2(\omega)$ which is explained qualitatively by the Mattis-Bardeen theory [88]. For microwave signals, this feature is best understood in terms of a complex *surface impedance* Z_s given by

$$Z_s = R_s + jX_s, \tag{3.27}$$

where R_s is resistance and X_s is the admittance. Equation (3.27) is related to $\sigma(\omega)$ by the following

$$Z_s = \sqrt{\frac{j\omega\mu_0}{\sigma(\omega)}}, \tag{3.28}$$

where μ_0 is the permeability of free space. The origin of equation (3.28) is because of the kinetic inductance of Cooper pairs. London [51] predicted that a superconductor will demonstrate a small amount of dissipation for frequencies up to the superconducting gap resulting from "broken" Cooper pairs, or "quasi-particles", which contribute to a finite admittance X_s. For a semi-infinite superconductor X_s is given by

$$X_s = \mu_0\omega\lambda_L(T) \tag{3.29}$$

where $\lambda_L(T) = \lambda(0)/\sqrt{1-(T/T_c)^4}$ is the effective penetration depth of the superconductor at temperature T where T_c is the transition temperature. Typically, X_s is much greater than R_s and can be considered as the dominant contributor to Z_s. For thin film devices, equation (3.28) is recast in the following form [86]

$$Z_s^{tf} = Z_s \coth\left(\sqrt{j\omega\mu_0\sigma}\cdot d\right), \tag{3.30}$$

where d is the thickness of the film. It can be shown that (3.28) then becomes

$$X_s^{tf} = \mu_0\omega\lambda_L(T)\coth(d/\lambda_L). \tag{3.31}$$

For completeness, we include the result for the resistance R_s [86], given by

$$R_s^{tf} = \frac{1}{2}\sigma_n\mu_0^2\omega^2\lambda_L^3(T)\left(\frac{T}{T_c}\right)^4\left(\coth(d/\lambda_L) + \frac{d}{\lambda_L}\mathrm{csch}^2(d/\lambda_L)\right), \tag{3.32}$$

where σ_n is the normal state conductivity. The surface impedance of the superconducting material is input numerically into HFSS as an intrinsic property of the material.

3.2.2 HFSS simulation environment

The basic elements of an HFSS model are excitation ports and boundaries. These elements connect and assign conditions to the structure which is to be simulated. There are many different types of boundaries that can be defined in HFSS to account for conduction and propagation characteristics of the system. The relevant types will be discussed here.

Boundary conditions

A *perfect electrical boundary* is a type boundary definition for perfect electrical conductors and outer boundaries where convergence of the solution requires vanishing of the electric field. By default, the perfect electrical boundaries assume the electric field is normal to the surface and the conductivity is infinite. An *impedance boundary* is used to model surfaces of known impedance Z_s, such as the surface impedance of a superconductor. This condition imposes the following relation on the tangential components of the electric field $\boldsymbol{E}$ and magnetic field $\boldsymbol{H}$:

$$\boldsymbol{E}_{tan} = Z_s \left(\hat{\boldsymbol{n}} \times \boldsymbol{H}_{tan} \right). \tag{3.33}$$

Wave ports

The outer perfect electric boundary defines an interface between the 3D objects in the model and the background through which no electromagnetic energy may enter or exit. A wave port defines a window on this interface which couples the 3D model to external microwave signals. A wave port is assumed to be a semi-infinite waveguide which is defined by the cross-sectional geometry at the surface of the port. HFSS assumes the device under simulation is excited by the modes associated with the 2D cross-sectional geometry of the waveguide. The definition of the port relies on specifying reference structures which are grounded and those through which the signal is excited. Figure 3.3 shows a 3D CAD model of the simulated device and also plots of the electric field profile at the wave ports.

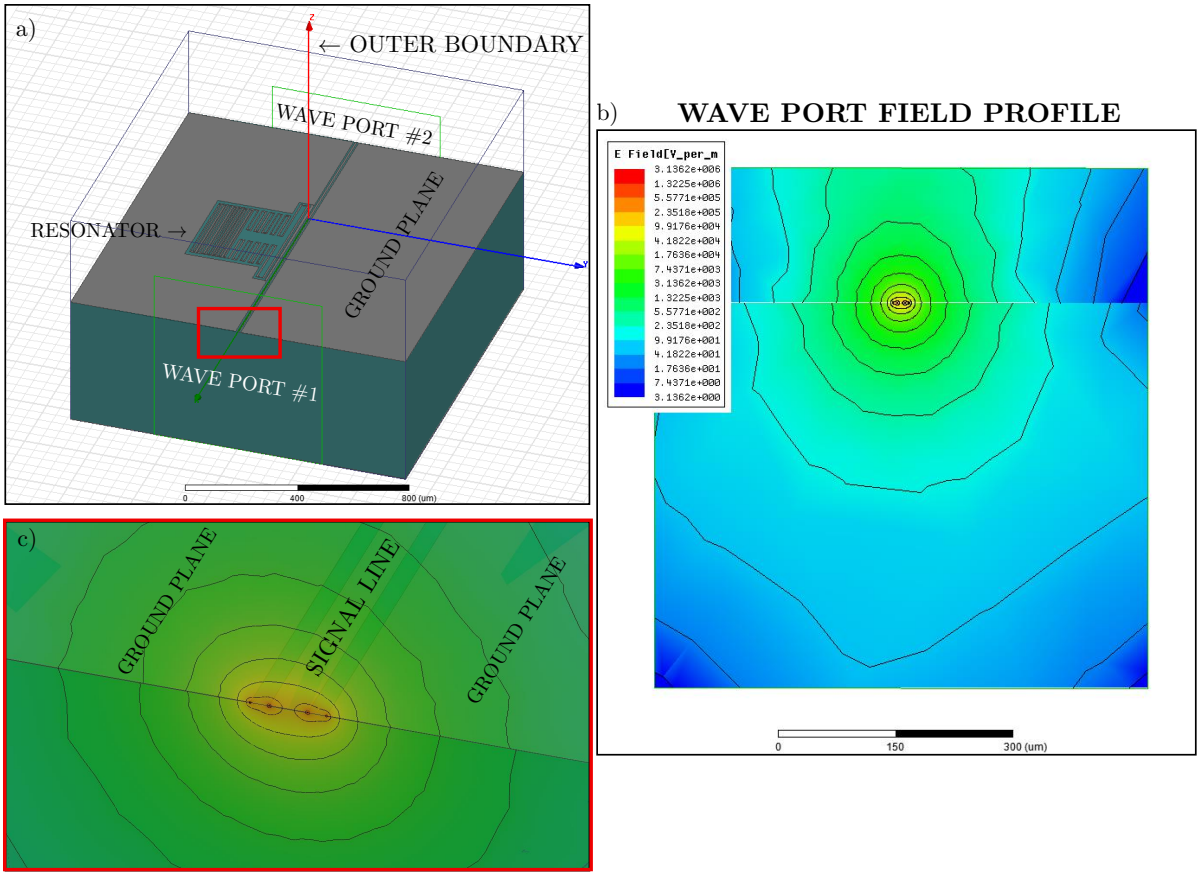

Figure 3.3: a) HFSS 3D model of a superconducting interdigital resonator on a silicon substrate connected to two microwave ports and an outer perfect electrical boundary. b) Electric field profile at the wave port. The 2D geometry of the port serves as an aperture for a rectangular waveguide of the same cross section. Electromagnetic waves supported by the rectangular geometry of the wave port are used to stimulate the device at different frequencies when performing a frequency sweep. c) Zoom of electric field profile on the wave port demonstrating the profile of the even TEM mode for a coplanar waveguide structure.

Modelling losses

Dielectric losses can be accounted for by simply defining the dielectric loss tangent to be non-zero. In typical high quality substrates used for superconducting microwave devices, such as Silicon or

Sapphire, the loss tangent is typically on the order of 10^{-6} or less, corresponding to an internal Q-factor on the order of 10^6. The loss due to thin, presumably amorphous, dielectric layers can be treated in two ways. The first is simply by including them geometrically in the 3D model. However, this makes the system much more complex to solve in computational terms, since now the 3D volume of the thin layer must be meshed and resolved in the solution. For a typical microwave structure, meshing at lengths scales of tens of microns is sufficient to yield accurate microwave parameters. With an additional layer on the order of 10 nm thick, HFSS will try to construct a mesh on the order of this length scale leading to the consumption of a large amount of computational resources. The second, more efficient, way to account for dielectric layers is by using a layered impedance boundary. Like the surface impedance boundary, this type of condition will modify the impedance over the length scale of the thickness and in turn the microwave and electromagnetic properties. HFSS calculates the impedance of the k^{th} layer, $Z_{input,k}$, in a multi-layer structure recursively using the formulation from transmission line theory [58, 2]

$$Z_{input,k} = Z_{w,k}\frac{Z_{input,k+1}\coth(\gamma_k d_k) + Z_{w,k}\sinh(\gamma_k d_k)}{Z_{input,k+1}\sinh(\gamma_k d_k) + Z_{w,k}\coth(\gamma_k d_k)}, \tag{3.34}$$

where $Z_{w,k} = \sqrt{\frac{\mu_0\mu_{r,k}}{\epsilon_0\epsilon_{r,k}}}$ is the impedance of layer k, $\gamma_k = \omega\sqrt{\epsilon_0\epsilon_{r,k}\mu_0\mu_{r,k}}$ is the propagation coefficient, d_k is the thickness of the layer, and $\epsilon_{r,k}$ and $\mu_{r,k}$ are the relative permittivity and permeability respectively. The permittivities and permeabilities are parameters specified by the user according to the following definitions

$$\epsilon_{r,k} = \epsilon_{r,k} - j\left(\frac{\sigma_k}{\omega\epsilon_0} + \epsilon_{r,k}\tan\delta_{\epsilon_{r,k}}\right), \tag{3.35}$$

$$\mu_{r,k} = \mu_{r,k} - j\left(\mu_{r,k}\tan\delta_{\mu_{r,k}}\right), \tag{3.36}$$

where σ_k is the conductivity, ω is the angular frequency and $\delta_{\epsilon_{r,k}}$ and $\delta_{\mu_{r,k}}$ and the dielectric and magnetic loss tangents respectively.

3.2.3 Simulation results for an interdigital resonator

Figure 3.4 shows a simulated transmission curve near resonance of the superconducting resonator shown in Fig. 3.3 a).

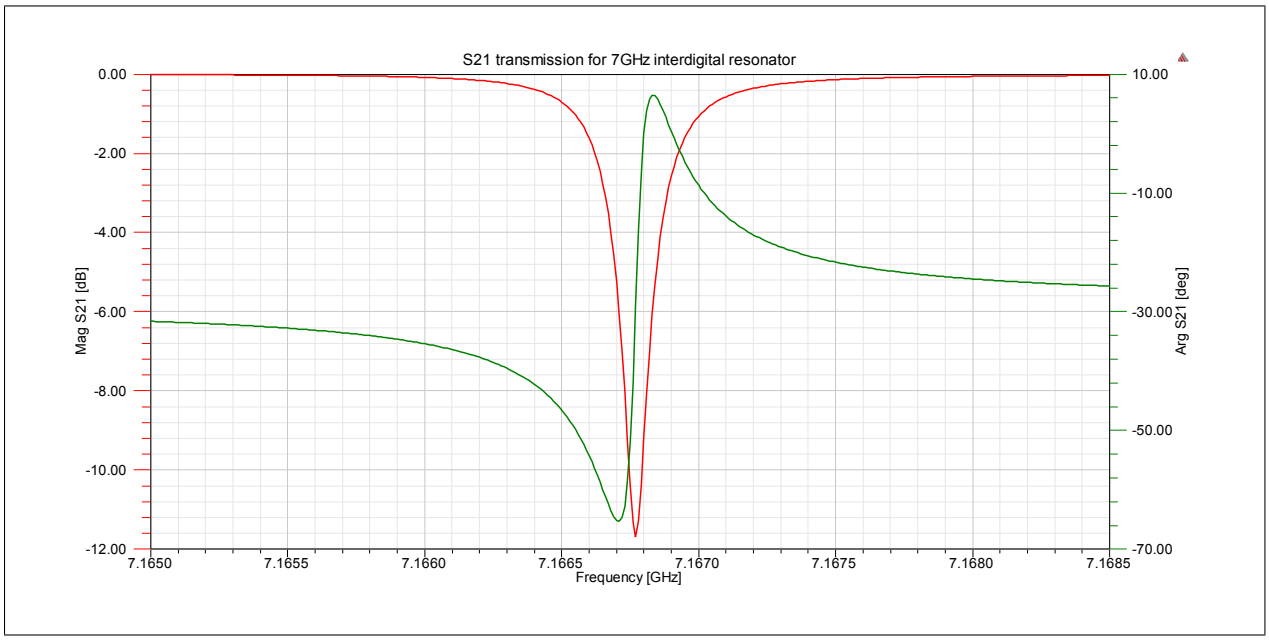

Figure 3.4: Transmission response of an interdigital resonator on silicon ($\tan\delta = 5 \times 10^{-6}$ to model baseline losses in the simulation). The thickness of the superconductor is 100 nm and no additional dielectric layers were incorporated.

The resonance frequency for this particular device was found to be within 10 MHz of the measured device. This deviation is partially due to imperfections in the fabricated device and also the presence of a dielectric layer.

3.2.4 Estimation of coupling factors

The mutual inductance M and coupling capacitance C_c are determined by fitting the simulated S_{21} from Fig. 3.4 to equation (3.19). This fitting procedure directly provides Q_e which is then equated to equation (3.20). This yields an equation in terms of the capacitance C_c, inductance L and mutual inductance M which can be solved numerically for these parameters. Furthermore, the definition of the resonance frequency (equation (3.16)) can be combined with its value to yield an approximate relationship between the geometric inductance and capacitance of the resonator. For the resonators considered in this work, it is found that only the first term, that containing M, in the expression for λ given by equation (3.25) is significant.

3.2.5 Calculation of dielectric participation ratios

As mentioned in the introduction, losses in the resonator are additive and are normalized with respect to the total energy stored in the device on resonance. Mathematically the total dielectric loss tangent is given as

$$W_E \tan\delta = \sum_n W_{E_n} \tan\delta_n, \tag{3.37}$$

where W_E is the total electric field energy of the resonator and W_{E_n} is the energy contained in the n^{th} dielectric layer. The total electrical energy is found by integrating the energy density over the volume of interest,

$$W_E = \frac{1}{2}\int_V \epsilon(\boldsymbol{r})|\boldsymbol{E}(\boldsymbol{r})|^2 d\boldsymbol{r}. \tag{3.38}$$

The measured loss, or inverse internal Q-factor, is then

$$\tan\delta = Q_i^{-1} = \sum_n p_n \tan\delta_n \tag{3.39}$$

where p_n is the participation ratio of the n^{th} dielectric layer and describes its relative weight. Mathematically it is simply

$$p_n = \int_{V_n} \epsilon(\boldsymbol{r})|\boldsymbol{E}(\boldsymbol{r})|^2 d\boldsymbol{r} \Big/ \int_V \epsilon(\boldsymbol{r})|\boldsymbol{E}(\boldsymbol{r})|^2 d\boldsymbol{r}. \tag{3.40}$$

The participation ratios for a given dielectric thickness can be determined from both HFSS [2] simulations at microwave frequencies and quasi-static electric field simulations using COMSOL Multiphysics [3] . The important requirement in obtaining a reliable estimate of p_n is to have a fine solution for the electric field in the region of the oxide layer. This is generally much easier to achieve in the quasi-static case since a 2D geometry need only be simulated and, as a result, a much finer mesh can be achieved than for the case of a full 3D model. The quasi-static case in COMSOL is valid since the characteristic geometry of the capacitor is on the scale of ~ 10 um, much less than the wavelength of the microwave signal used in experiments. Therefore, the quasi-static description of the field is equal to the time averaged AC field. This claim will be discussed further in chapter 5 when the effect of an inhomogeneous electric field is considered.

3.3 Device fabrication

Fabrication of samples was carried out in a class 1000 cleanroom facility. The samples must be kept as clean and contaminant free as possible throughout the fabrication process. Any foreign residues from photo-resists and moisture can unpredictably affect the quality of the device and the reliability of the experimental results. Devices are fabricated using standard lithography techniques on high-quality, high-resistivity crystalline Silicon substrates. Devices using both aluminum and niobium as the superconducting material were fabricated for experimental characterization. The aluminum films are deposited using an electron beam evaporat0or and the niobium films are grown using an RF-sputtering system. Both metals develop native oxides upon exposure to atmospheric conditions. Once the resonator is fabricated, an additional thick layer of Al_2O_3 is deposited on the surface of the device using atomic layer deposition (ALD). This layer is the material of interest in terms of understanding loss mechanisms in Aluminum oxide.

3.3.1 Fabrication of devices with aluminum resonators

Fabrication of aluminum based devices involves optical lithography followed by evaporation and lift-off of aluminum to define the resonator structures. The fabrication process used in this work is presented here and an image of the finished resonator is provided in Fig. 3.5.

1. Pre-cleaning of Si substrate
    a) Cleaning in PRS-3000 solvent
    b) Cleaning in acetone followed by isopropanol and de-ionized water
2. Surface treatment prior to photoresist application
    a) Dehydration bake followed by adhesion primer
3. Optical lithography
    a) Application of Ma-N 1400 negative tone photoresist followed by hotplate baking
    b) UV exposure
        ii) Exposure in constant power mode using Karl Suss mask aligner

4. Resist development
    a) Bath 1: Ma-N developer
    b) Bath 2: Ma-N developer
    c) Bath 1: DI water
    d) Bath 2: DI water
    e) Descum in YES pr-stripper
5. Evaporation of Aluminum
    a) Single layer 100nm evaporation of aluminum
6. Aluminum lift-off
    a) Bath 1: PRS-3000
    b) Bath 2: PG remover
    c) Bath 3: Acetone
    d) Bath 4: Isopropanol

3.3.2 Fabrication of Niobium devices

Niobium devices are fabricated using a positive optical lithography followed by reactive ion etching to define the resonator structures. A photograph of a completed resonator is provided in Fig. 3.6.

1. Pre-cleaning of Si substrate
    a) Cleaning in PRS-3000 solvent
    b) Cleaning in acetone followed by isopropanol and de-ionized water
2. Niobium sputtering of 100nm film using RF plasma
3. Optical Lithography
    a) Application of S1811 positive tone resist followed by baking on hotplate
    b) UV exposure
        i) Exposure in constant intensity mode using Karl Suss Mask aligner

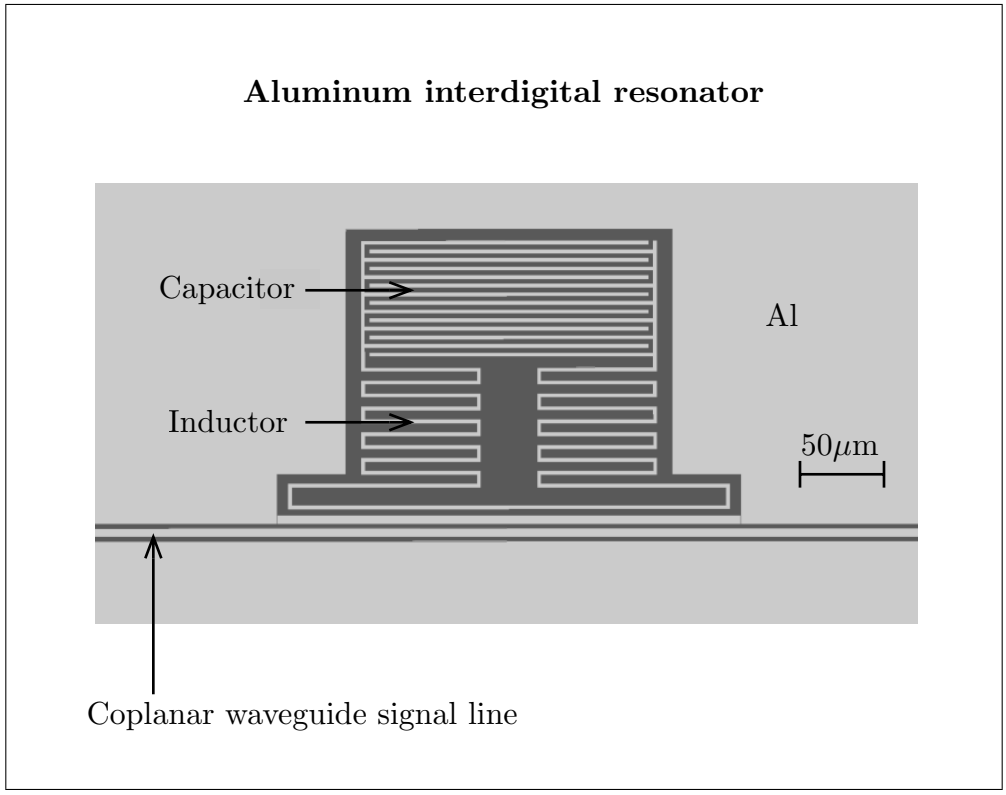

Figure 3.5: Photograph of Aluminum based interdigital resonator fabricated on Si by lift-off.

4. Resist development
    a) Bath 1: MF-319 developer
    b) Bath 2: MF-319 developer
    c) Bath 1: DI water
    d) Bath 2: DI water
5. Reactive Ion Etching using fluorine ions
6. Cleaning
    a) Cleaning in PRS-3000 solvent
    b) Cleaning in acetone
    c) Cleaning in isopropanol

3.3.3 Atomic layer deposition of Al_2O_3

The material which is the focus of this thesis was Al_2O_3 grown by ALD. ALD is a novel growth technique which offers precise thickness control and conformal high-quality films [27]. This deposition technique relies on a sequence of self limiting surface reactions. A highly reactive precursor, tri-methyl aluminum (TMA) in the case of Al_2O_3, is injected into the deposition chamber at a pressure of $< 10^{-6}$ Torr. TMA undergoes chemisorption at the surface of the substrate with active OH^- groups bound to the substrate and the metal surfaces. One of the methyl functional groups is replaced by an OH^- as the TMA bonds to the surface. After the chemisorption is saturated, the chamber is purged, removing excess precursor. An O_2 plasma source is then used to remove the remaining methyl groups and bind Al_2OH^-. This completes one cycle and results in a layer 1 Å in thickness. A diagram of the process is shown above in Fig. 3.7. This process is repeated as necessary to achieve the desired thickness. For many cycles the stoichiometry of the resulting oxide film is $Al_2O_{3.05}$. Using O_2 plasma as the oxidizing agent eliminates the need for H_2O, which results in lower deposition temperatures and impurity content. Furthermore, O_2 plasma serves as a way to clean the sample in-situ prior to deposition. We note that this will inevitably oxidize the surface, but only by forming a thin layer of either AlO_x or NbO_x on the metal and SiO_x on the substrate, which would have been present anyway in the form of a native

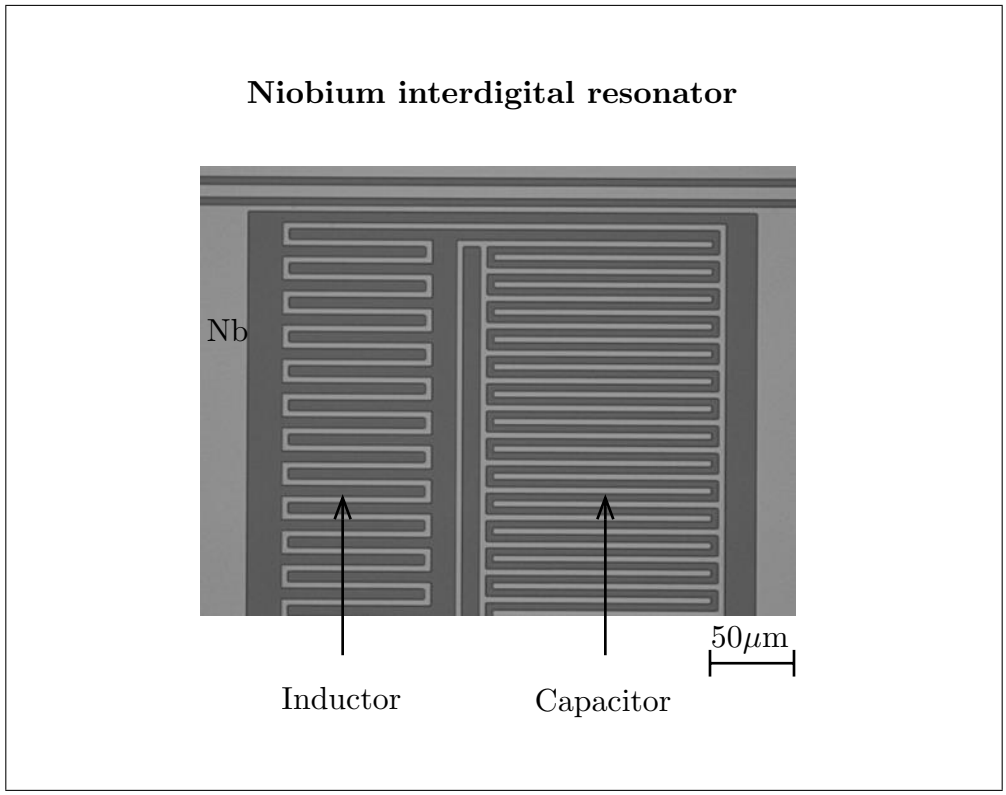

Figure 3.6: Photograph of Niobium based interdigital resonator fabricated on Si by reactive ion etching.

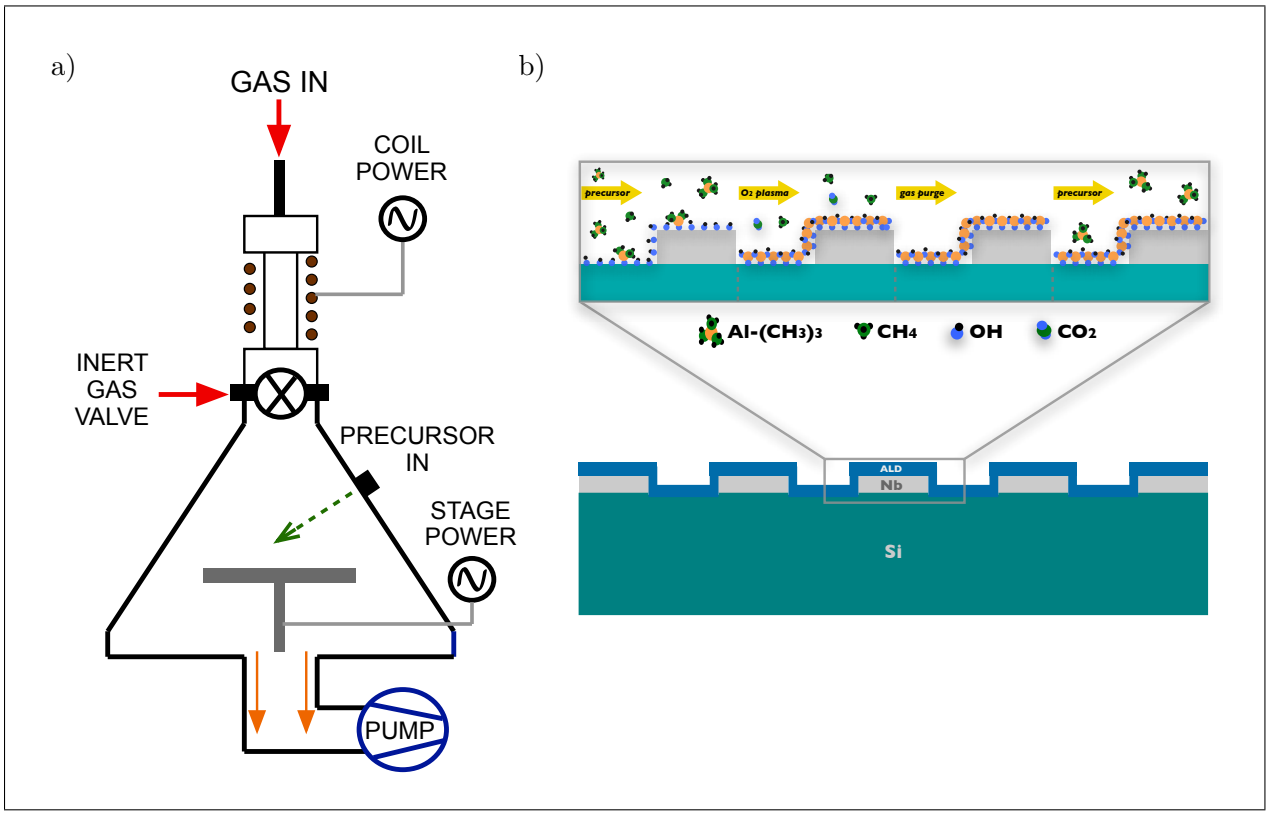

Figure 3.7: a) Schematic illustration of the ALD deposition chamber adapted from [1]. The b) Diagram of ALD deposition steps for the growth of Al_2O_3.

oxide. The merit is that this plasma cleaning step will remove any resist residues which may have been left over from earlier fabrication steps, which can be detrimental on device performance.

3.3.4 Electron beam lithography of multilayer capacitor structures

Some resonator designs feature a parallel plate capacitor structure, where the oxide layer is sandwiched between the plates. The fabrication of these devices involves a second layer lithography and metallization step. Patterning of the top metal plates is achieved by electron beam lithography. This process involves a double layer resist profile which results in an undercut profile of the resist after exposure and development. The undercut profile aids the lift-off process and yields clean metal structures. This process is the same as that used for Josephson junction fabrication. A photograph of the device is provided in Fig. 3.8.

1. Resist application
    a) Layer 1: PMGI SF7 followed by hotplate baking
    b) Layer 2: PMMA A3 followed by hotplate baking
2. E-beam exposure at 25 kV
3. Resist development
    a) PMMA development
        i) Bath 1: MIBK:Isopropanol 1:3
        ii) Bath 2: Isopropanol
    b) PMGI development
        i) Bath 1: MicroDev concentrate
        ii) Bath 2: DI water
4. Aluminum evaporation
    a) Double angle evaporation of Aluminum, total thickness of 100nm
5. Aluminum lift-off
    a) Bath 1: PRS-3000

b) Bath 2: Acetone

d) Bath 3: Isopropanol

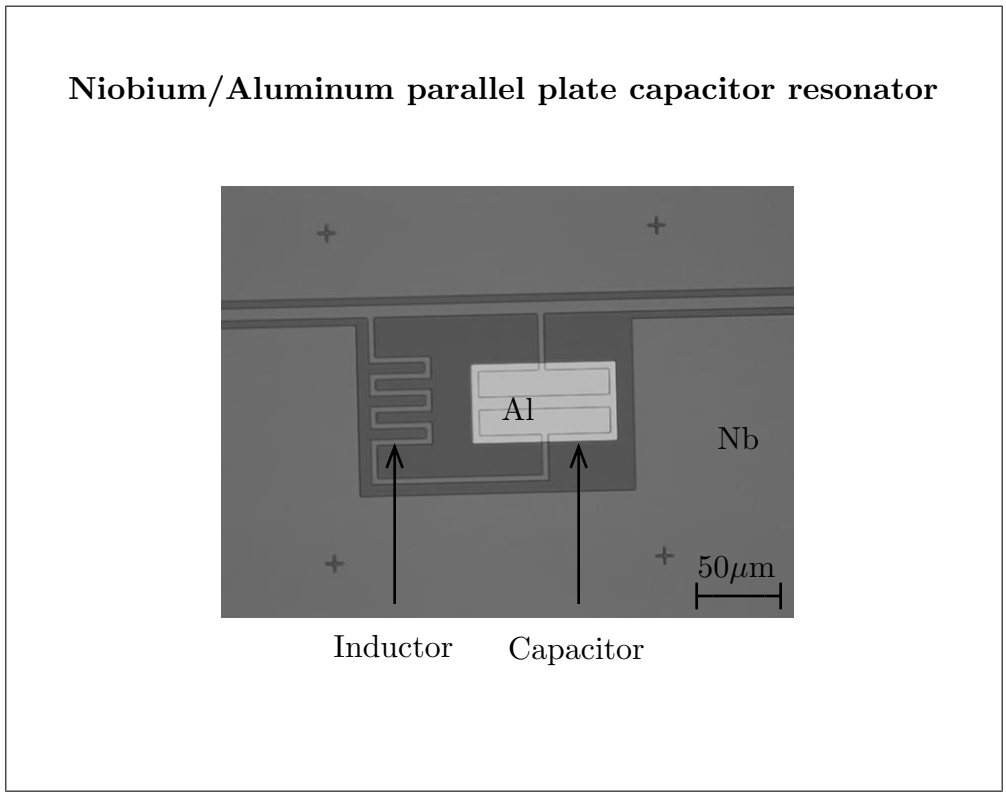

Figure 3.8: Photograph of Niobium/Aluminum device where the top capacitor plate is patterned by electron beam lithography.

3.3.5 Sample dicing

Fabrication of samples is done in large quantities to give a good sample yield. 4" Silicon wafers consisting of twenty 17 mm $\times$ 17 mm chips are fabricated in bulk. Each chip contains ten devices 3 mm $\times$ 7 mm in size. A typical wafer is diced using a diamond saw which has resolution on the order of 100 μm. Prior to dicing, samples are coated with a thick layer of protective resist which helps reduce dust and debris produced by the saw. Following dicing, samples are cleaned thoroughly and can then be packaged for low-temperature characterization.

3.4 Low-temperature setup

3.4.1 Dilution refrigeration

Measurements are performed in a 3He/4He dilution refrigerator. Dilution refrigeration [21] is the only method to achieve continuous cooling below 300 mK. This remarkable scientific tool works according to the special low temperature properties of liquid helium mixtures. The mechanism is very closely related to the idea of evaporative cooling, and relies on a natural phase separation occurring at sufficiently low temperatures. 3He, the natural isotope of more common 4He, is more strongly bound to 4He because 4He has larger mass and therefore a lower zero-point energy. 3He obeys Fermi statistics and therefore the kinetic energy increases with increasing number density. At a 3He concentration of 6.5% in a 3He/4He mixture, the effective binding energy becomes 0 as $T \to 0$, and therefore no more 3He atoms may be dissolved into 4He. At this point, it becomes energetically more favourable for two different liquid phases to exist. One phase, the *light* phase, is 3He rich and a second, the *heavy* phase, is a superfluid of mostly 4He. 3He atoms in the light phase have lower entropy than those in the heavy phase. This difference allows for a cooling process to be driven by transferring 3He atoms from the rich phase to the dilute heavy phase. The analogy with evaporative cooling is that 3He atoms are "evaporated" into a "quasi-vacuum" of 4He. For continuous operation, one must remove 3He from the dilute phase and then feed it back into the rich phase.

The dilution circuit which supports the circulation of the helium mixture, consists of the mixing chamber, the still and heat exchangers between them as illustrated in Fig. 3.9. Circulation is driven by pumping on the still usually with large turbo molecular pumps, which offer high pumping speeds. As a result of its higher vapour pressure, 3He is predominantly evaporated from the dilute phase in the still. This volume of 3He is circulated outside the cryostat, cleaned using traps immersed in liquid nitrogen, and fed back into the cryostat where it re-condenses at the mixing chamber. This condensation relies on the concentration of 3He gas to be sufficiently high. The return line of the circuit starts below the phase boundary immersed in the 4He rich superfluid phase. As it returns to the still, the cold mixture pre-cools the incoming 3He. Pumping the still results in a 3He concentration gradient in the dilute phase and, in turn, an osmotic pressure which promotes the flow of 3He to the mixing chamber. The cooling process overall relies on the ability of 3He atoms to cross the phase boundary. The rate at which they can cross determines the cooling power of the system. Temperatures as low as 1.5 mK [16] have been obtained in

continuous operation using dilution refrigerators.

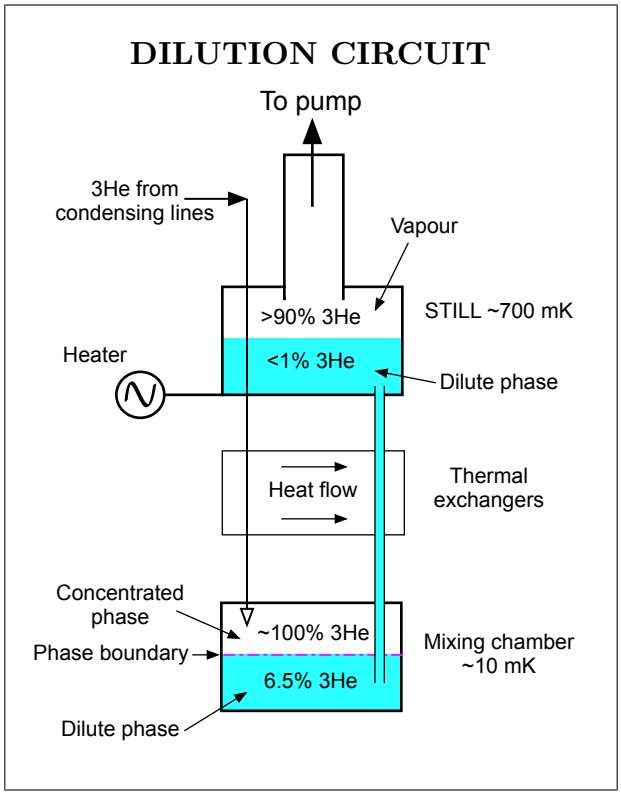

Figure 3.9: Schematic of the dilution circuit, adapted from Enss and Hunklinger, Low temperature physics, Ch. 11, Springer (2004) [21].

3.4.2 Sample packaging

Devices are wire-bound with Aluminum wire to a custom made microwave printed circuit board (PCB). The PCB is made from a Rogers^{TM} TMM 10i panel and gold plated in a non-magnetic process with a thickness of 1 μm. The sample fits into a window cut-out in the center of the circular PCB and fastened to a bottom copper plate with cryogenic varnish. The PCB is fastened to the copper plate. A photograph of the sample mounted to the PCB is provided in Fig. 3.10. The PCB has coplanar traces with a 500 μm center trace width and a 250 μm gap and has a characteristic impedance of 50 Ω. The traces are soldered to SMP connectors which mate with SMP bullets embedded the top copper package. The complete package is then mounted to an

insertable probe which will be discussed next.

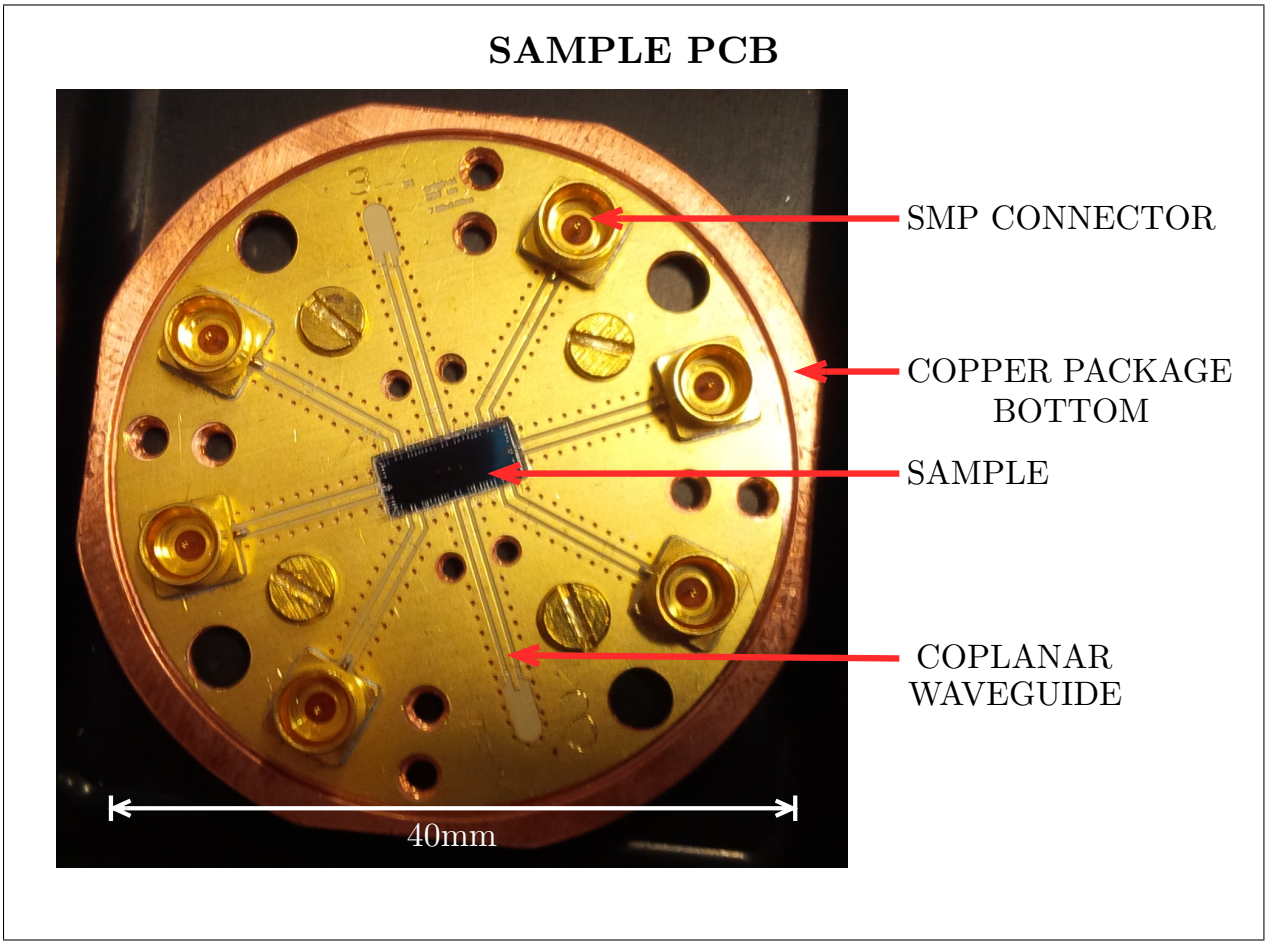

Figure 3.10: Photograph of sample PCB mounted to the bottom copper plate of the microwave package. The sample is wire-bonded to the gold-plated PCB consisting of coplanar signal traces connected to microwave SMP connectors.

3.4.3 Insertable RF-probe

A convenient feature of our experimental setup is the short turn-around time of the experiments. This is made possible by the use of an insertable RF probe, previously developed by our group in collaboration with Leiden Cryogenics [57]. The sample package is fastened to the probe in a manner which is depicted in Fig. 3.11.

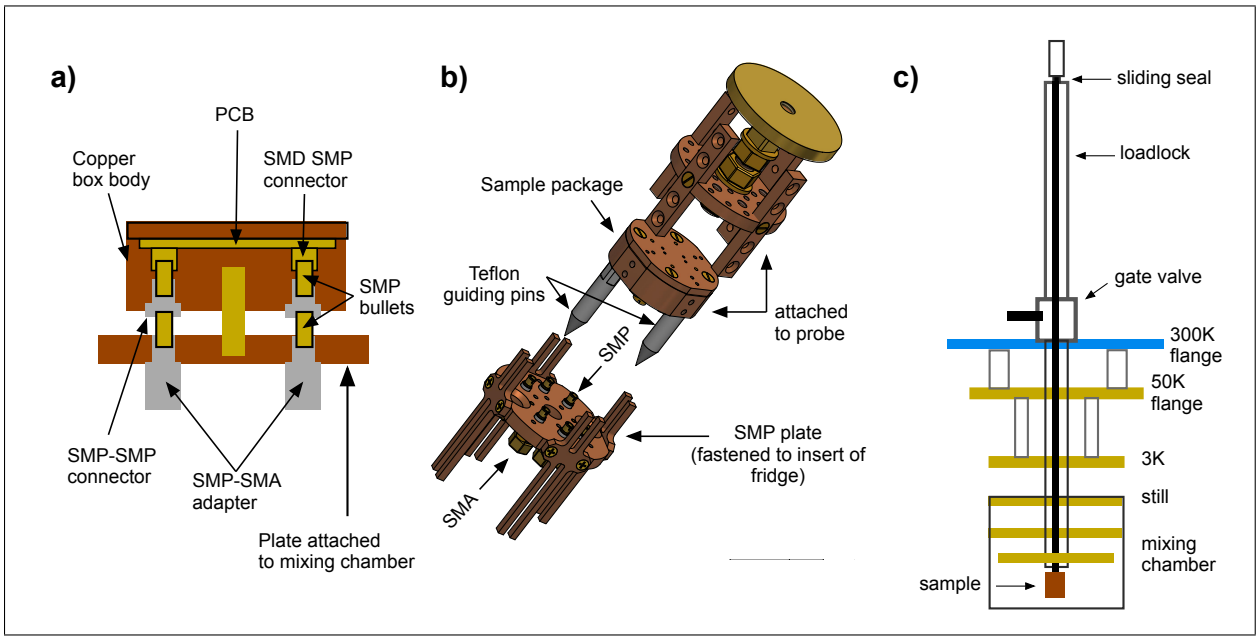

Figure 3.11: Schematic of insertable RF probe (adapted from reference [57]). a) Cross-sectional view of the microwave connection mechanism between the sample box attached to the probe and the coaxial lines leading to the mixing chamber stage from the experimental setup. b) 3D CAD of the sample box, its attachment to the insertable probe and the SMP plate at the mixing chamber stage. c) Illustration of complete probe inserted into the dilution fridge. The probe passes through a 50mm clearance hole extending from room temperature flange to the mixing chamber stage. The load lock allows for the insertion and retraction of the probe while keeping the system cold and under vacuum. When fully inserted, the probe is "tightened" by twisting the knob at the top to extend the contact pads and establish thermal contact with the thermal plates inside the dilution refrigerator.

The probe is mounted at the top of the dilution refrigerator using a load-lock vacuum chamber which is coupled to the inner vacuum chamber (IVC) by a gate valve. At the top of the load-lock there is a sliding seal which allows for the insertion downwards into the IVC. As the probe is lowered, it passes through a 50 mm clear shot opening from the room temperature 300 K flange to the mixing chamber stage. When fully inserted, the SMP connectors on the microwave package make contact with the connectors permanently anchored to the main insert of the fridge. The SMP bullets and connectors have minimal disengagement force for when the probe is lifted out of the fridge. Once this connection is made the sample is connected to the microwave coaxial

lines of the experimental setup. At each thermal stage of the fridge, there are corresponding thermal contact pads which are tightened mechanically and press against the fridge to achieve thermal contact. Typical base temperature on the probe is 20 mK, which is made possible by careful thermal anchoring and radiation shielding inside the dilution refrigerator. The probe also is equipped with DC leads for thermometry and coils for experiments requiring small magnetic fields.

3.4.4 Microwave measurement setup

Quality factor measurements of the resonator are made using an Agilent E-series vector network analyser (VNA) as illustrated schematically in Fig. 3.12. Port 1 of the VNA is connected to the input line of the device. The input line is strongly attenuated to achieve very low microwave powers at the sample. The attenuation of the input line from 300 K to the mixing chamber has a total attenuation of ~ 50 dB which was determined by a room temperature transmission measurement. This factor, A, is taken into account when the VNA excitation power P_{in}^{+} is converted to the RMS input voltage V_{in}^{+} at the level of the device. This conversion is made using the following formula [68].

$$\left(V_{in}^{+}\right)_{\mathrm{RMS}}[\mathrm{V}] = \sqrt{\frac{Z_0[\Omega]}{10^3[\mathrm{mW/W}]} 10^{\frac{P_{in}^{+}[\mathrm{dBm}]+A[\mathrm{dB}]}{10}}}, \tag{3.41}$$

where the Z_0 is 50 Ω. This factor is very important in the analysis of dielectric loss and will be characterized in further detail in the following chapter.

3.4.5 Temperature control

In this work, the temperature dependent properties of dielectric loss were of particular interest. As a result, care was taken in making reliable measurements of the temperature on the probe at the level of the sample. Measurements ranging from a base temperature of 40 mK up to 1 K were performed by heating the mixing chamber of the dilution refrigerator. This was performed by applying some heat to the mixing chamber which affects the properties of the Helium mixture. The temperature was measured using two low-temperature resistance thermometers. One was a Speer carbon resistor thermometer and the other a Ruthenium oxide (RuO) thermometer. A photograph of the probe showing the thermometers is presented below in Fig. 3.14.

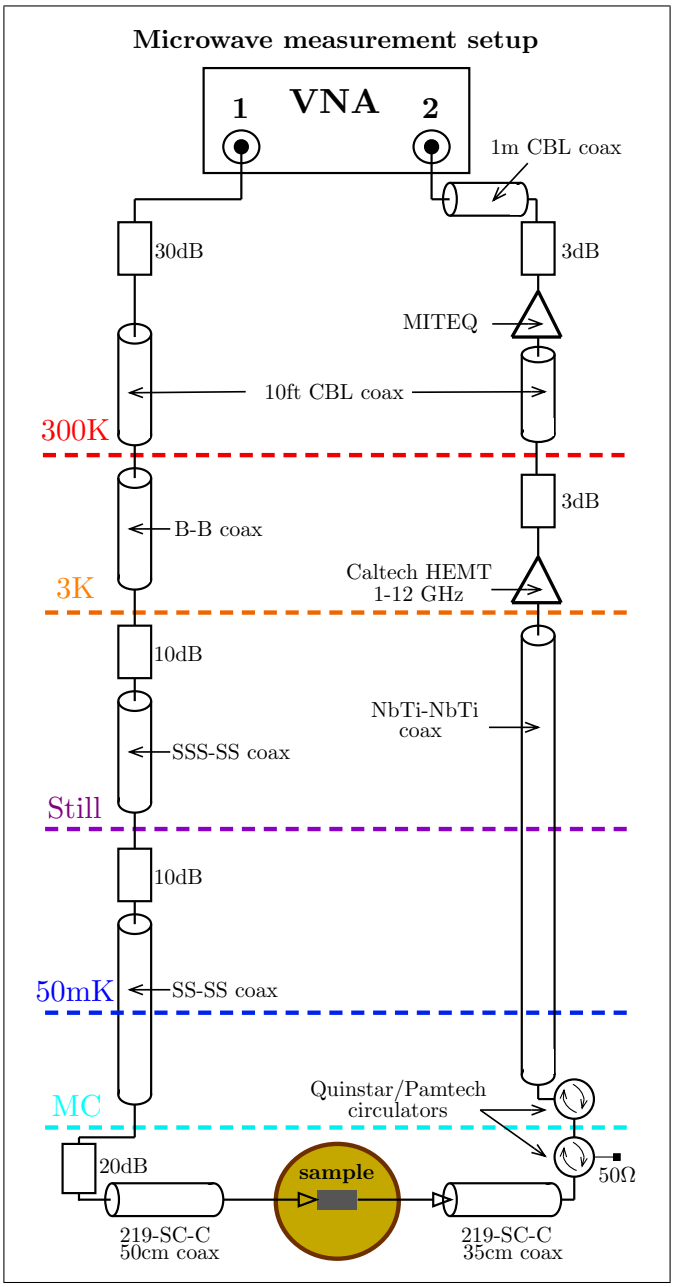

Figure 3.12: Schematic of the microwave setup used for dielectric loss measurements. The outer diameter of all coaxial cables is 219mm and they are semi-rigid "SC" cables. The specific cables are specified by the conductive materials used by the abbreviation:"outer conductor - inner conductor". C: copper, B: beryllium, SSS: high grade stainless steel, SS: medium grade stainless steel, NbTi: niobium-titanium

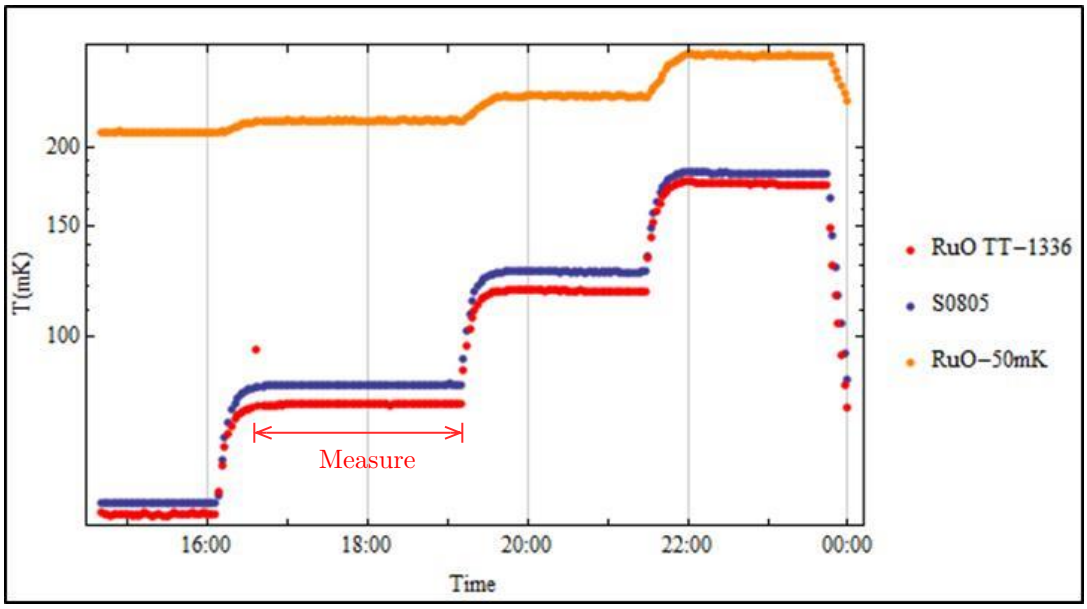

Figure 3.13: Plot of temperature vs time for a set of temperature dependence measurements. Measurements are performed after the system stabilizes at a given temperature when current is applied to the mixing chamber. The plot shows the measured temperatures of the two sensors at the mixing chamber level (RuO TT and Speer S0805) and also another which is mounted at the cold plate (50 mK plate) above the mixing chamber.

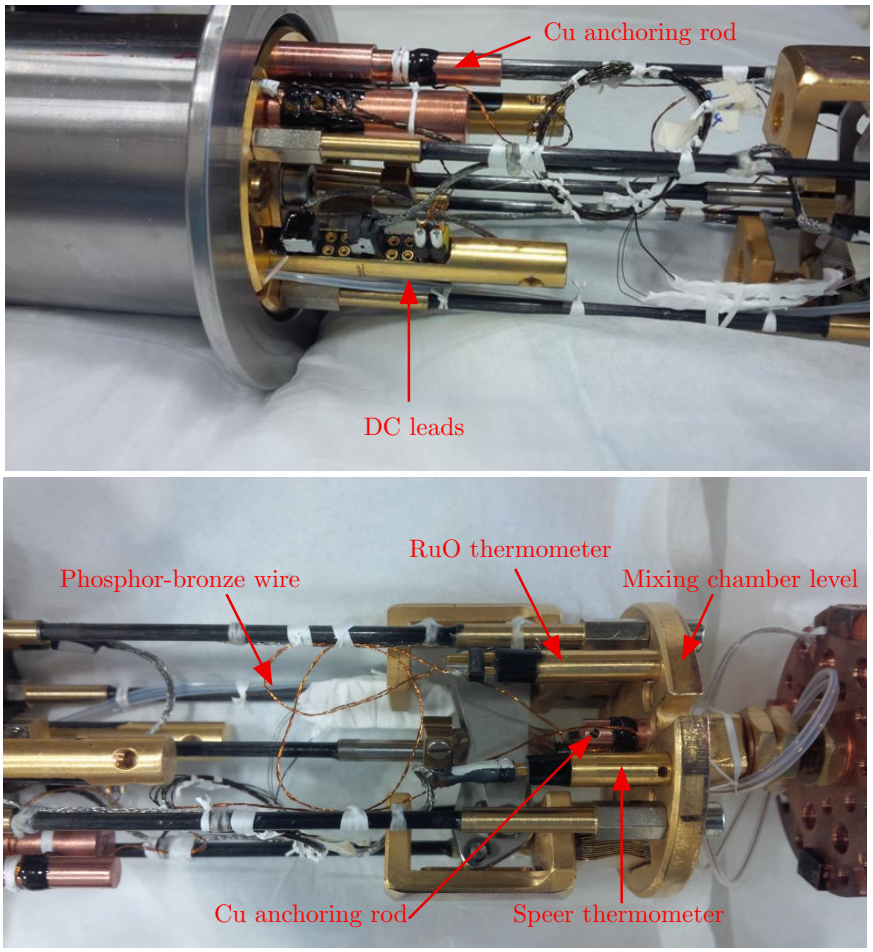

Figure 3.14: Photograph of the insertable probe showing the thermometry setup.

The thermometers are measured using an impedance bridge in a 4-point measurement configuration. The RuO thermometer was installed using OFHC copper anchoring rods at both the 50 mK and mixing chamber stages. The DC leads used were 50 cm Phosphor-bronze AWG 36 with a polymide insulation. The wires were made into two twisted pair sets and attached to the anchoring rods using stycast 2850 epoxy.

Figure 3.13 shows the behaviour of the mixing chamber temperatures when heating is applied. The system responds by increasing its temperature and eventually stabilizes at a new higher temperature. The stability of the temperature is excellent, rarely deviating by more than ~ 2 mK during one of the measurement plateaus below 300 mK. Measurements at higher temperatures, must be done by removing 3He from the mixture and putting it in the dumps in the gas handling system of the fridge. This effectively reduces the cooling power and stable temperature plateaus can also be achieved similar to what is presented in Fig. 3.13, but at temperatures greater than 300 mK. The behaviour of the mixing chamber at these higher temperatures is shown in Fig. 3.15.

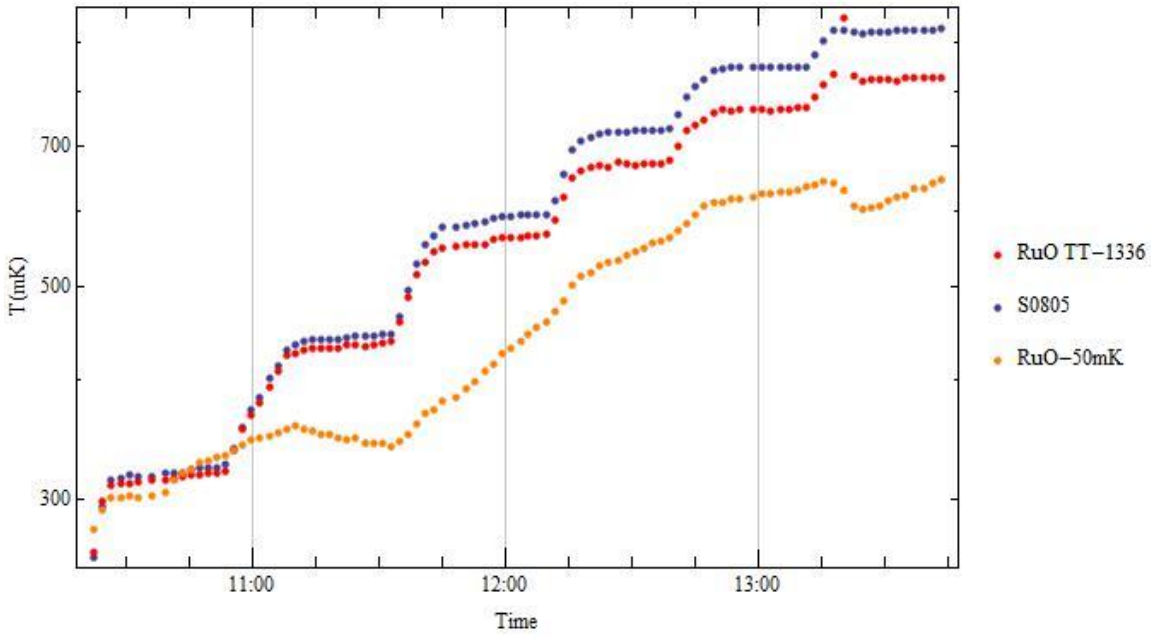

Figure 3.15: Plot of temperature vs time for a set of temperature dependence measurements above 300 mK. The plot shows the measured temperature of the two sensors at the mixing chamber level (RuO TT and Speer S0805) and also another which is mounted at the "50 mK" plate above the mixing chamber.

One of the sensors was also directly attached to the sample package during some of the

experiments to ensure that the sample was at the same temperature as the mixing chamber. A photograph of this is shown below in Fig. 3.16. It was found that there was no significant change in the measured temperature in this configuration.

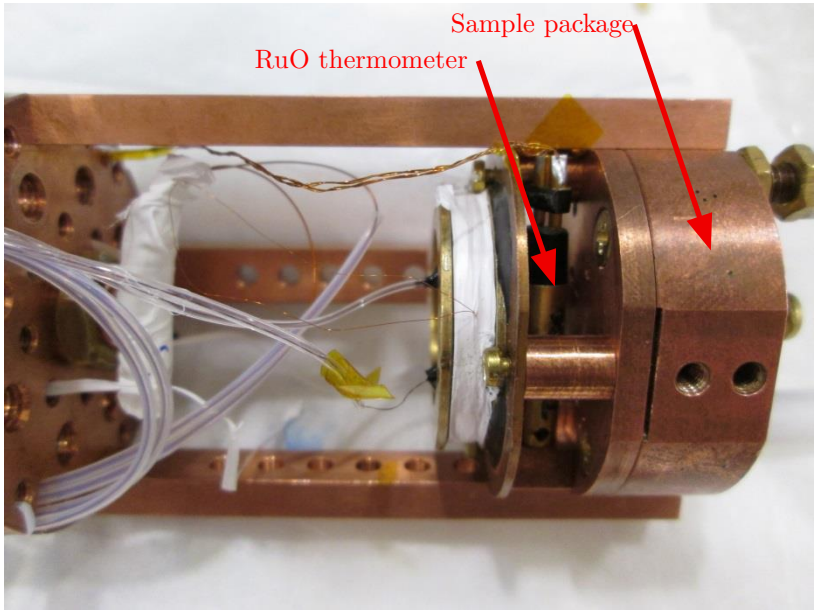

Figure 3.16: Image of RuO thermometer mounted directly to microwave sample package for temperature dependence experiments.

There is a difference in the measured temperatures between the two sensors which can be seen in Fig. 3.13 and Fig. 3.15. Despite this difference, the interpretation of the dielectric loss measurement data is not affected insofar as the agreement with the TLS model is altered. Therefore, we use the average values of the two measured temperatures in the analysis of the experimental data which will be presented in chapter 6.

Chapter 4

Characterization of the frequency dependence of the input line attenuation

The experimental setup used in this work was designed to be heavily attenuated (∼50 dB) in order to achieve low-power signals (single photon level) for experiments involving measurements of quantum bits. One of the key physical quantities of interest in this work is the behaviour of the critical electric field, which depends on the coherence properties of two-level systems according to equation (2.94). To solidify any claims concerning measurements of the critical field, we require a more thorough quantification of the experimental setup, in particular the frequency dependence of the attenuation of the input coaxial microwave lines shown in Fig. 3.12. This is important because the precise value of the critical field extracted from the measurements depends on this attenuation factor according to equation (3.37), which is itself a frequency-dependent quantity.

In this chapter, we present a characterization of this aspect of the experimental setup. Our first estimate of the frequency dependence is from a room temperature transmission measurement of the input line using a VNA. Using this information we apply some estimates of the change in attenuation which would arise at cryogenic temperatures using some values from literature. In the second approach, Rabi oscillations are driven in a superconducting flux qubit device. The measured Rabi frequency is directly proportional to the current felt by the qubit at the frequency of the driving signal. Using this measurement, the calibrated value of the input power and a

numerical simulation of the microwave transmission of the device, the frequency-dependence of the attenuation is determined. The important feature is the relative difference in attenuation across the frequency band of interest. The absolute value of the attenuation depends on the parameters of the flux qubit, in particular the degree to which it couples to the coplanar waveguide resonator.

4.1 Estimate of attenuation factor

4.1.1 Room temperature measurement

The coaxial lines in the experimental setup are made from beryllium and stainless steel materials each of which demonstrate different frequency dependent attenuation characteristics. Figure 4.1 shows a measurement of the attenuation of the input microwave line at room temperature. At "zero" frequency, the value of -40 dB is due to cryogenic attenuators which are installed inside the dilution refrigerator at various thermal stages.

4.1.2 Frequency dependence of stainless steel coaxial cables at cryogenic temperatures

In general, both the frequency and temperature dependence of the attenuation depends rather sensitively on the specific properties of the alloys from which the cables are manufactured. Furthermore, it is also difficult to characterize because the profile of the temperature gradient over the length of the cables of interest is unknown in many experimental configurations. In general the attenuation will decrease and become less frequency dependent as the cables are cooled. Figure 4.2 below uses data from reference [83] and shows the behaviour of the attenuation per unit length at various temperatures. (Note that the 4 K curve is an estimate from the behaviour of the other 3 curves).

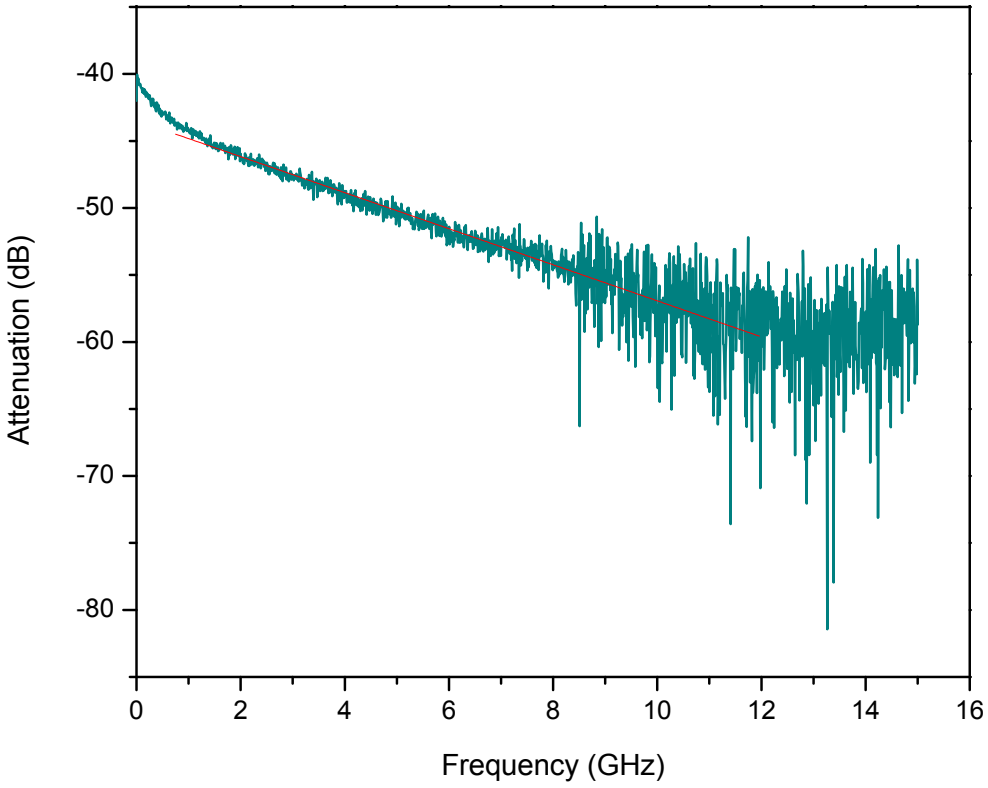

Figure 4.1: Room temperature measurement of the input line attenuation using a vector network analyzer. The red line is a linear fit to the data.

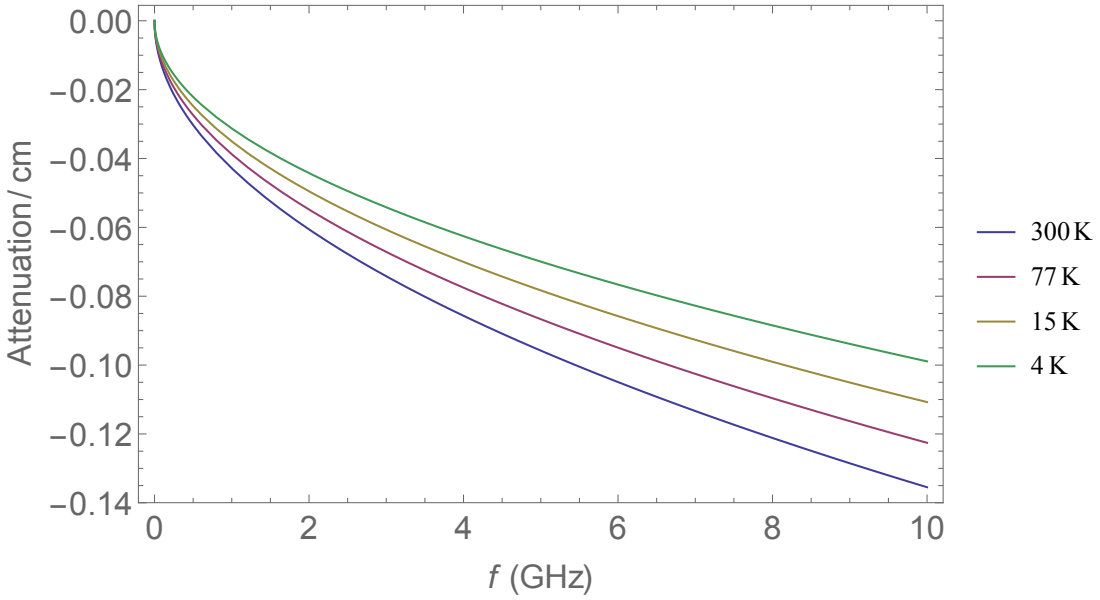

Figure 4.2: Estimate attenuation per unit length in SS-SS stainless steel coaxial cables at various temperatures. Plots are adapted from data presented in [83].

From this plot, and using the approximate lengths of the coaxial cables we can estimate the attenuation of the input line at a given frequency.

4.2 Characterization of input line attenuation using a flux qubit

The device used in this analysis was a flux qubit in a circuit quantum electrodynamics setup as shown schematically in Fig. 1.3. The resonator is a coplanar waveguide resonator with a resonance frequency of 6.641 GHz. The qubit frequency is tuned by threading external magnetic flux through the loop which forms the qubit. The qubit frequency is tuned from $3 - 9$ GHz and pulsed with resonant microwave tones through the input of the resonator to induce Rabi oscillations which are then measured using homodyne voltage quadratures via the output of the resonator.

4.2.1 Physical description

We consider a quantum bit with a time-independent Hamiltonian given by H_0 subject to a time-dependent drive $V(t)$ [47, 71]. It is useful to use the transformation between states in the Schrödinger picture, $|\Psi_S\rangle$ to states the interaction picture, $|\Psi_I\rangle$, given by

$$|\Psi_I(t)\rangle = e^{iH_0 t/\hbar}|\Psi_S(t)\rangle. \tag{4.1}$$

The Schrödinger equation in the interaction picture is given by

$$i\hbar\frac{\partial}{\partial t}|\Psi_I(t)\rangle = \tilde{V}(t)|\Psi_I(t)\rangle, \tag{4.2}$$

where $\tilde{V}(t) = e^{-iH_0 t/\hbar}V(t)e^{-iH_0 t/\hbar}$ is the time-dependent drive in the interaction picture. At $t = 0$ the initial state of the system in the Schrödinger picture is

$$|\Psi_S(t=0)\rangle = \sum_{n=1,2} a_n(0)|n\rangle, \tag{4.3}$$

where $|n\rangle$ are the eigenstates of H_0 and $a_n(0)$ specifies the initial state probabilities. When the time-dependent driving field is turned on, for $t > 0$ the state evolves according to the following

$$|\Psi_S(t)\rangle = \sum_{n=1,2} a_n(t)e^{-iE_n t/\hbar}|n\rangle. \tag{4.4}$$

In the interaction picture, the evolution becomes

$$|\Psi_I(t)\rangle = \sum_{n=1,2} a_n(t)|n\rangle. \tag{4.5}$$

Inserting equation (4.5) into the Schrödinger equation in the interaction picture, we obtain the following coupled equations:

$$\dot{a}_n(t) = \frac{1}{i\hbar}\sum_m V_{nm}(t)e^{i\omega_{nm}t}a_m(t), \tag{4.6}$$

where $V_{nm}(t) = \langle n|V(t)|m\rangle$ and we have introduced $\omega_{nm} = (E_n - E_m)/\hbar$, where E_n and E_n are the eigenenergies of H_0. We now consider the simple case of transverse driving of the qubit at a

frequency ω such that $V_{12} = \mathcal{A}e^{i\omega t}$, $V_{21} = V_{12}^*$ and $V_{11} = V_{22} = 0$. The amplitude of the driving field $\mathcal{A}$ is taken to be real. The system of coupled equations given in (4.6) is reduced to

$$\dot{a}_1 = \frac{1}{i\hbar}\mathcal{A}e^{i\Delta t}a_2, \tag{4.7}$$

$$\dot{a}_2 = \frac{1}{i\hbar}\mathcal{A}e^{-i\Delta t}a_1, \tag{4.8}$$

where $\Delta = \omega - \omega_{21}$ is the *detuning* from resonance. Differentiating (4.7) and then substituting (4.8) yields

$$\ddot{a}_1 = \frac{\mathcal{A}}{i\hbar}\left(i\Delta a_2 + \frac{\mathcal{A}}{i\hbar}e^{-i\Delta t}a_1\right)e^{i\Delta t} = i\Delta\dot{a}_1 - \frac{\mathcal{A}^2}{\hbar^2}a_1. \tag{4.9}$$

The roots of the characteristic polynomial for this second order differential equation are given by

$$\gamma_{1,2} = i\left(\frac{\Delta}{2} \pm \sqrt{\frac{\Delta^2}{4} + \frac{\mathcal{A}^2}{\hbar^2}}\right) = i\left(\frac{\Delta}{2} \pm \Omega_R\right). \tag{4.10}$$

where Ω_R is the Rabi frequency. Using (4.10), the general solution to $a_1(t)$ is given by

$$a_1(t) = e^{i\Delta t/2}\left(Ae^{i\Omega_R t} + Be^{-i\Omega_R t}\right), \tag{4.11}$$

where A and B are arbitrary coefficients. The solution for $a_2(t)$ is found by differentiating (4.11) which allows (4.7) to be expressed as

$$a_2(t) = \frac{\hbar}{\mathcal{A}}e^{-i\Delta t/2}\left(A\left(-\Omega_R - \frac{\Delta}{2}\right)e^{i\Omega_R t} + B\left(\Omega_R - \frac{\Delta}{2}\right)e^{-i\Omega_R t}\right). \tag{4.12}$$

Applying the initial conditions we find that

$$A = \frac{1}{2}\left(1 - \frac{\Delta}{2\Omega_R}\right), \tag{4.13}$$

$$B = \frac{1}{2}\left(1 + \frac{\Delta}{2\Omega_R}\right). \tag{4.14}$$

For driving on-resonance ($\Delta = 0$), we obtain the simple results:

$$a_1(t) = \cos(\Omega_R t), \tag{4.15}$$

$$a_2(t) = \sin(\Omega_R t), \tag{4.16}$$

which demonstrates the oscillation between eigenstates of the system as a result of the driving.

For a flux qubit, the Rabi frequency for on-resonance driving at the frequency of the qubit ν_{qb} in terms of the qubit parameters, is given by [23]

$$\Omega_R = \frac{MI_p\delta}{h\nu_{qb}} I_{qb}, \tag{4.17}$$

where M is the mutual inductance of the qubit loop, I_p is the persistent current of the qubit and δ is the qubit gap energy. All of these parameters are intrinsic parameters of the qubit design. The coupling scales proportionally to the current which couples to the qubit, I_{qb}. This quantity is of interest to us in particular as it depends on the transmission of the cavity at a particular frequency. For the qubit used in this analysis, $\delta/\hbar = 2.23$ GHz, $I_p = 690$ nA and $M = 18$ pH.

4.2.2 A simple transmission model

The quantity of interest is the magnitude of the transmission between the external setup which outputs a known voltage V^+_{out} and the input of the device which will have some attenuated voltage V^+_{cav}. The S_{21} transmission function is the ratio of these voltages,

$$S_{21}(f) = \frac{\text{cavity input}}{\text{setup output}} = \frac{V^+_{cav}}{V^+_{out}}. \tag{4.18}$$

V^+_{cav} can be determined by measuring the Rabi frequency of the qubit, and using a simulated model of resonator to which the qubit is coupled. In the simulation, carried out in SONNET$^{\text{TM}}$ [4], the qubit-resonator device is simulated at various frequencies with a constant input voltage of $V^+_{in} = 1$ V. The value of the current at the position of the qubit is extracted from a map of the current density, J_{xy}, and the following function is determined for all frequencies of interest,

$$v_i(f) = \frac{V^+_{in}}{I_{qb}(f)}. \tag{4.19}$$

Using this relation, which holds at any voltage of interest, the transmission becomes

$$S_{21}(f) = \frac{V^+_{cav}}{V^+_{out}} = \frac{\Omega_R(f) \times \frac{h}{I_p} \times \frac{\nu_{qb}}{\delta} \times \frac{v_i(f)}{M}}{V^+_{out}}. \tag{4.20}$$

An example of the current density generated in the resonator at 5 GHz near the qubit is shown in Fig. 4.3 below. The resolution of the simulation is sufficient for our aims, since the simulated device was modelled to have the same losses and resonant frequency as the measured device. The frequency of the resonator is 6.641 GHz, with a total quality factor of $\sim 3 \times 10^4$. In Fig. 4.4, the current density along a line which intersects the qubit is shown. The current profile similar to that shown in Fig. 4.3 is integrated numerically at all relevant frequencies to obtain the value of the current as a function of frequency, as shown in Fig. 4.5.

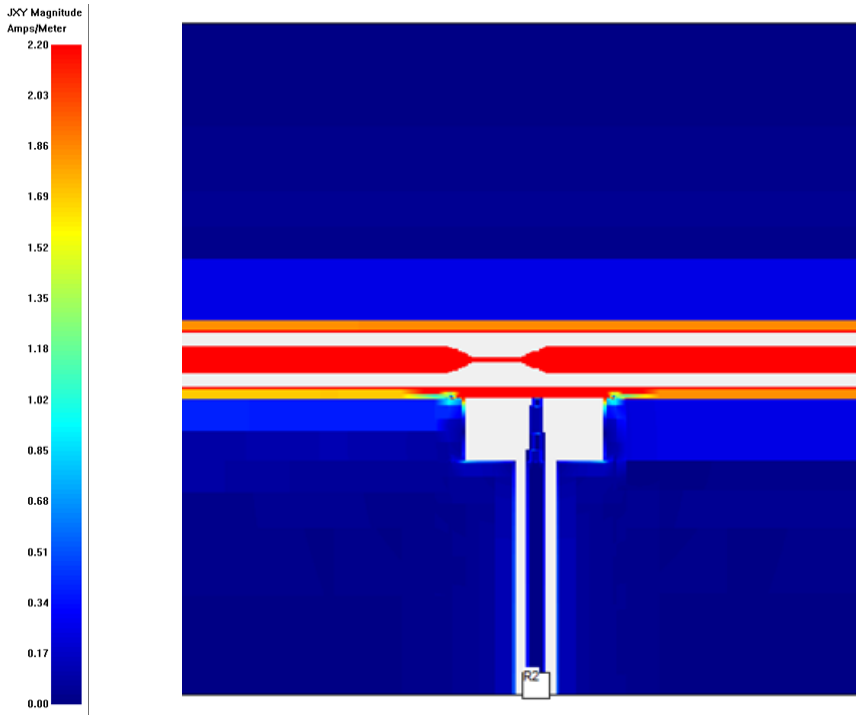

Figure 4.3: Sonnet simulation of current density in the vicinity of the qubit at 5 GHz

As can be seen in Fig. 4.3, the simulation includes the "fastline" which is used for control in other experiments. The coplanar waveguide resonator features the tapered profile where the qubit would be positioned in the real device. The detailed geometry of the qubit is omitted since it makes the simulation more tedious computationally.

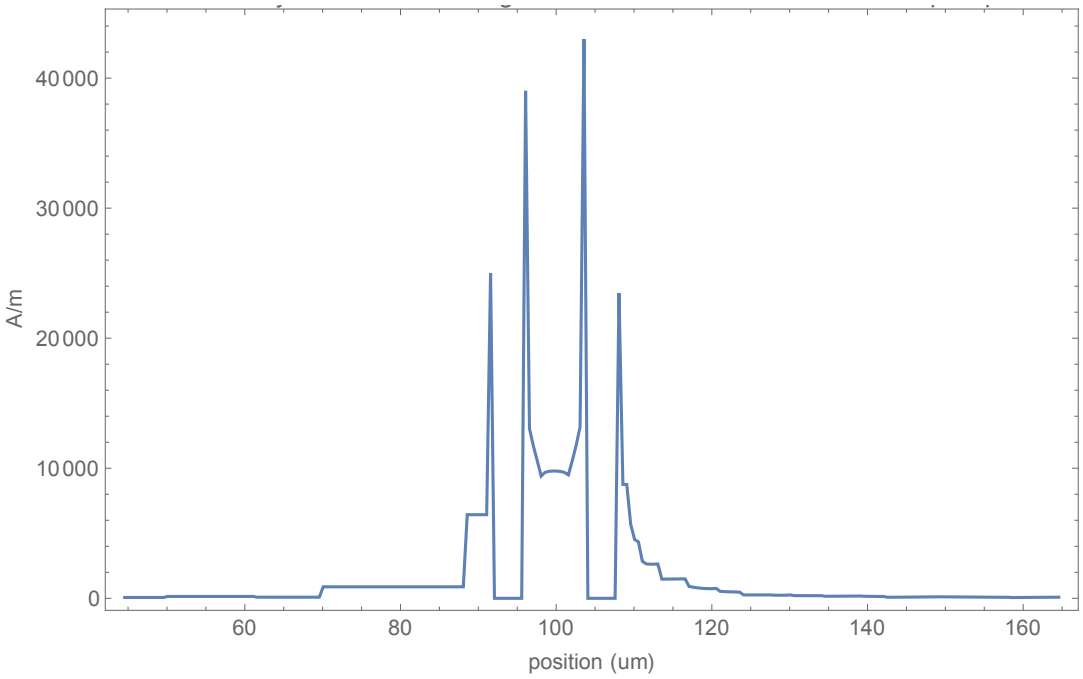

Figure 4.4: Simulated current density at 6.64 GHz along a line intersecting the coplanar waveguide resonator at the position of the qubit.

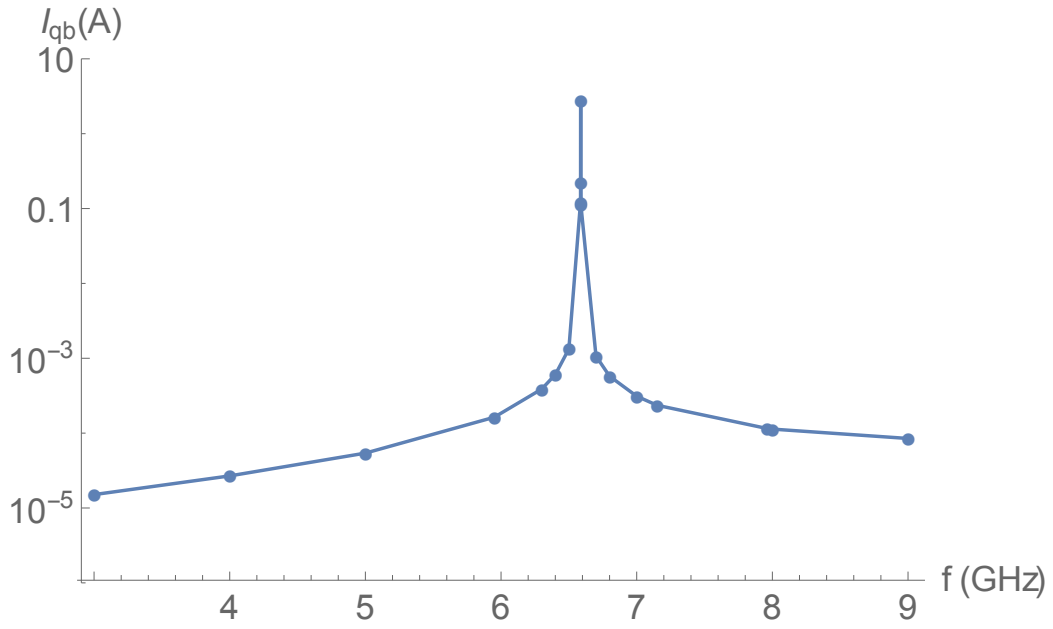

Figure 4.5: Computed current at the qubit position as a function of frequency for 1 V input port voltage. Values are determined by integrating the current density obtained from numerical simulations at various frequencies.

Figure 4.5 shows the expected result of a Lorentzian peaked at the frequency of the coplanar waveguide resonator. The resonator behaves as a microwave filter and correspondingly most of the signal, and therefore current, is transmitted near resonance. Conversely, away from resonance most of the incident microwaves are reflected at the input and do not enter the cavity.

4.2.3 Rabi Oscillations

In Fig. 4.6, we present measurements of Rabi oscillations at four different frequencies as an example of the measurements. Depending on the frequency of the qubit relative to the resonance of the cavity, the power delivered from the experimental setup must be adjusted accordingly such that oscillations may be detected. For this analysis, only the value of the Rabi frequency and the calibrated power from the output of the setup must be known to determine the attenuation of

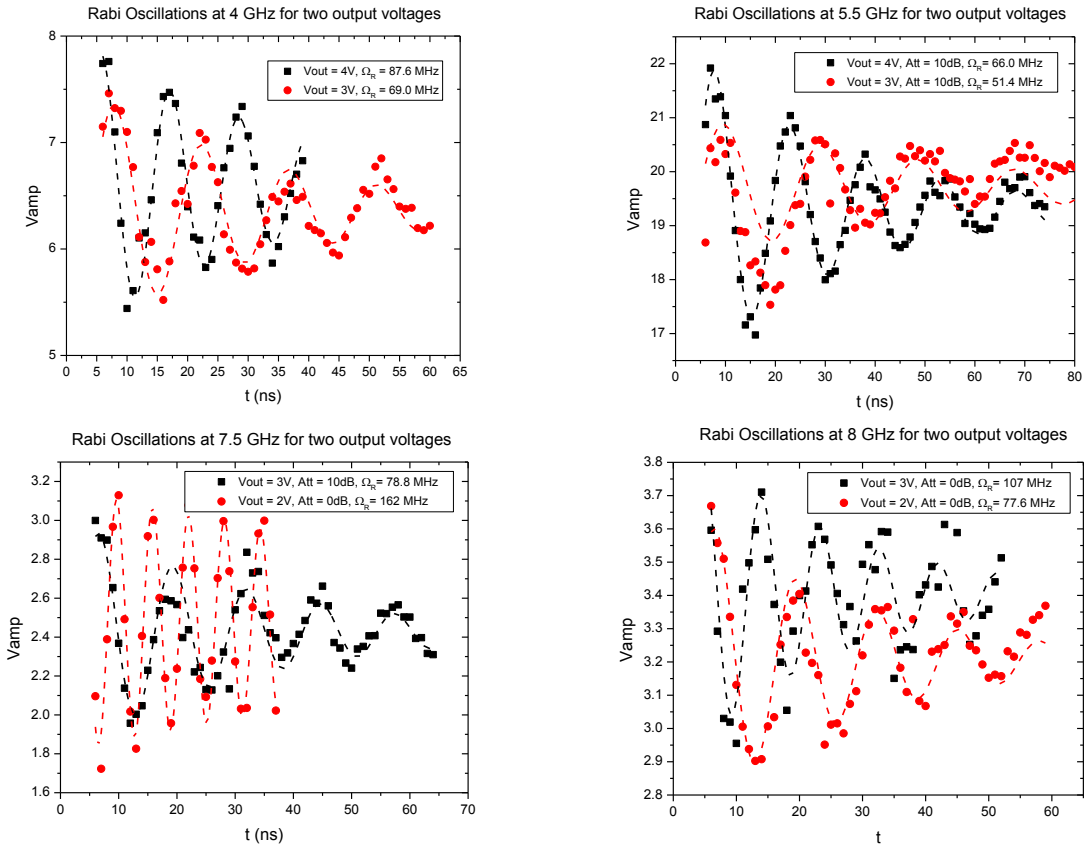

Figure 4.6: Measurements of Rabi oscillations at 4, 5.5, 7.5 and 8 GHz. At each frequency, at least two different output voltages were used. The Rabi frequency obtained from fitting to equation (4.21) is proportional to the current in the resonator at the qubit location.

the input line. The experimental data is fit to the following expression,

$$y = y_0 + A \exp\left(-t/t_0\right) \cos\left(2\pi(\Omega_R t + \phi)\right), \tag{4.21}$$

where y_0 is an arbitrary voltage of the amplified signal, t_0 is the decay time of oscillation envelope and ϕ is an arbitrary phase factor. Using equation (4.17) and the qubit parameters given in section 4.2.1, the $S_{21}(f)$ transmission function of the input line may be calculated for all frequencies at which Rabi oscillations were measured. This is shown in Fig. 4.7. It is important to mention that the qubit frequency spectrum is actually an approximation, and in fact the real spectrum is a dressed-strate of the coupled qubit-resonator system, and the deviations observed in Fig. 4.7 are a result of this.

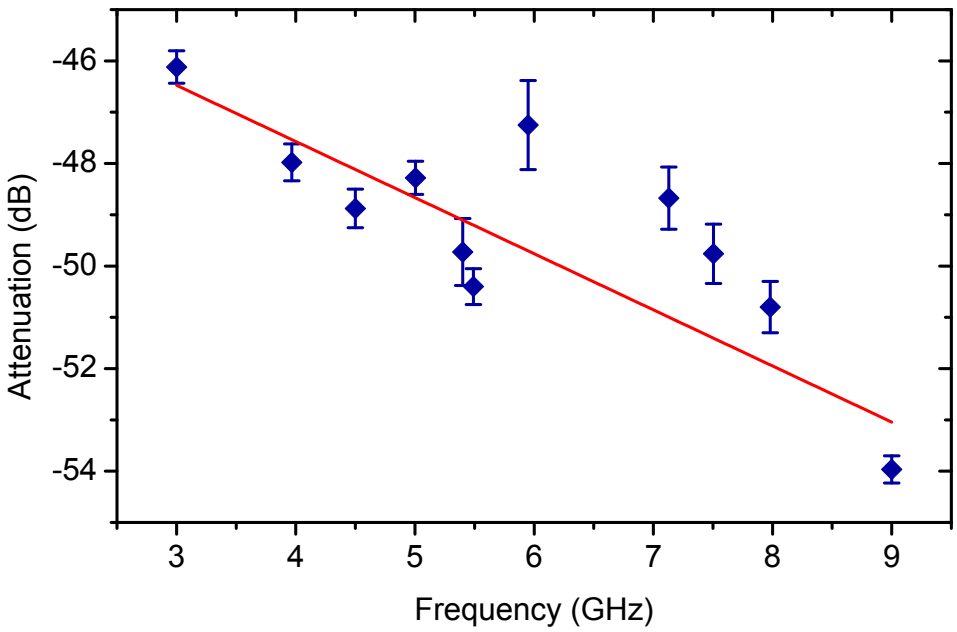

Figure 4.7: Calculated input line attenuation using measured Rabi frequencies and simulation of device transmission. Linear fit is in good agreement with the estimate from the room temperature attenuation measurement.

The data in Fig. 4.7 describes the attenuation of the input line used in all previous experiments

of dielectric loss. The data was fit to a linear expression which was in turn used to calculate values of the critical field at the frequencies of interest. Below we present a comparison of the critical field data for both our estimated attenuation and calibrated attenuation for the case of one device, W79-E4a, 4 interdigital aluminum resonators with 100 nm of ALD Aluminum oxide. The difference between the two data sets is not significant, but this step was a crucial verification for the critical field measurements.

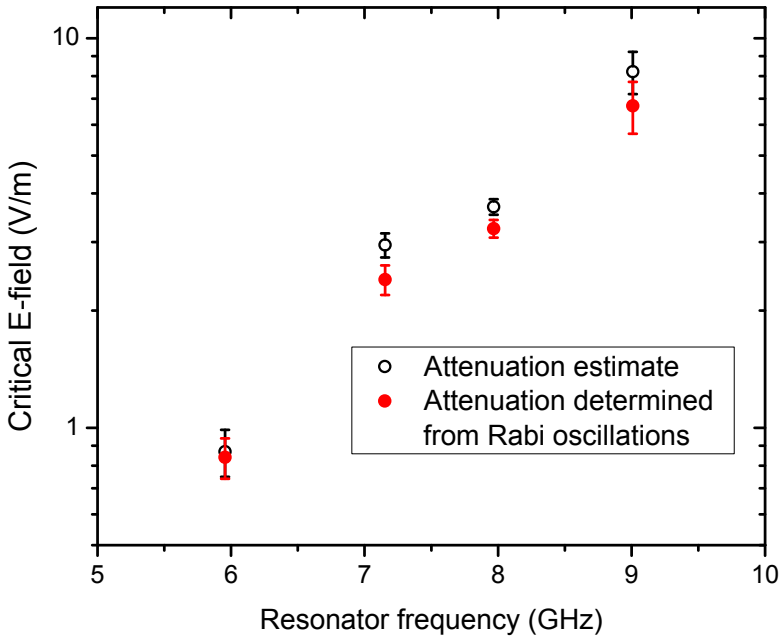

Figure 4.8: Comparison of extracted critical field values using an estimate from a room temperature measurement for the input line attenuation and also the measured attenuation from Rabi oscillations and device simulation.

To conclude this chapter, we have quantified the frequency dependence of the attenuation for the input microwave line in the experimental setup using a superconducting flux qubit. We find the attenuation factor decreased by 7 dB from 3 to 9 GHz, which is roughly consistent with estimates from the room-temperature measurement. Using this result we may more reliably account for measurements made at different frequencies and any frequency-dependent properties

of dielectric loss measurements can be claimed more assertively.

Chapter 5

Effect of an inhomogeneous electric field

In section 2.3, it was shown that an electric field couples to a TLS by a photon absorption excitation. When the excitation rate exceeds the relaxation rate due to phonon emission, TLSs start to become saturated, and the TLS density of states is suppressed. The assumption of a spatially homogeneous field implies that TLS saturation characteristics are identical throughout the volume of the host material. When the electric field is *inhomogeneous,* its strength, and therefore the TLS excitation rates, vary in space. In several types of superconducting resonators, the electric field of the superconducting resonator is inhomogeneous. This is certainly the case for half and quarter-wavelength coplanar waveguide resonators, and also for lumped element devices depending on the geometry of the capacitor. It is very important to take into account the inhomogeneity of the electric field in the resonator, for the purpose of reliably identifying the underlying behaviour of the TLSs. Many experiments on dielectric loss have been performed and interpreted by fitting the loss as a function of voltage at a constant temperature to the following "adjusted" formula

$$Q^{-1}(V) = Q_0^{-1}(\omega, T) \Big/ \sqrt{1 + (V/V_c)^{2-\delta}}, \tag{5.1}$$

where δ is a free fitting parameter and V_c is the critical voltage. As mentioned at the beginning of chapter 3, $\delta = 0$ is predicted by the TLS model for the case of a homogeneous electric field. Intuitively, one may see how a value of δ can arise in the case of an inhomogeneous electric

field. For a particular value of the capacitor voltage V, there will be a spatial distribution of the electric field across the oxide region. In the vicinity of TLS saturation, there will be a particular voltage value at which TLS start becoming saturated, and, as the voltage increases, eventually all TLS in the oxide region will be saturated. To quantify this effect, we investigate resonators with interdigital capacitors which have a lossy dielectric layer deposited on the surface. This type of capacitor is formed by an array of interlocking "fingers" as shown in Fig. 5.1. The capacitor fingers have a width w and the gap between them is g. The pitch between the centres of adjacent fingers is kept constant at 10 μm. The effect of the inhomogeneous electric field may be accounted for by simulating the electric field and constructing a probability distribution by sampling values of the field in the region defined by a given dielectric layer. Some experiments have attributed non-zero delta to arise from both other sources of loss and the geometry of the resonator [43, 26, 52, 70, 59, 7]. Others have also explicitly considered the profile of the field for the purpose of calculating the expected value of δ [82, 72]. In this chapter we pursue this further in a systematic study of the effect of geometry. We establish that the functional form of equation (4.1) involving δ arises from the inhomogeneity. Furthermore, this method consistently allows for the extraction of the critical electric field for resonators of different geometries.

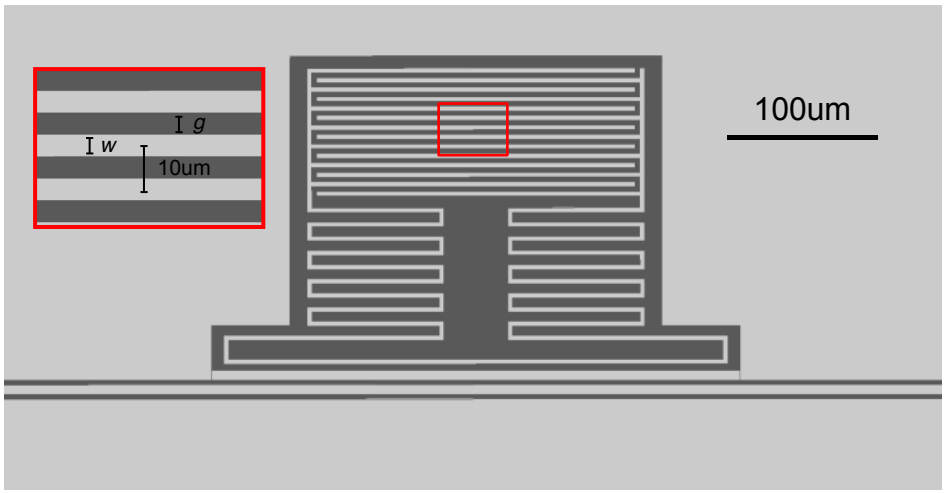

Figure 5.1: Image of a lumped element superconducting resonator consisting of an interdigital capacitor and meander inductor. Light grey regions are aluminum and the dark grey is the silicon substrate. The capacitor fingers have a width w, gap g and a constant pitch of 10 μm.

The physical resonator structure is 3D, but there is translational symmetry in the field profile along the direction of fingers, so we need only consider a 2D cross-section. We recall that the spatial profile of the electric field inside the lossy regions of the oxide layer is of interest. It is useful to construct a spatial grid where the spacing between points is much less than the thickness of the oxide layer and the metal film. In most devices, the thickness of the amorphous dielectric is 30-100 nm and the superconducting thin film is deposited with a thickness of 100 nm. The value of the electric field E_j at each point j of the 2D grid is extracted from numerical simulations and organized into a normalized histogram. A schematic of this scenario is illustrated in Fig. 5.2.

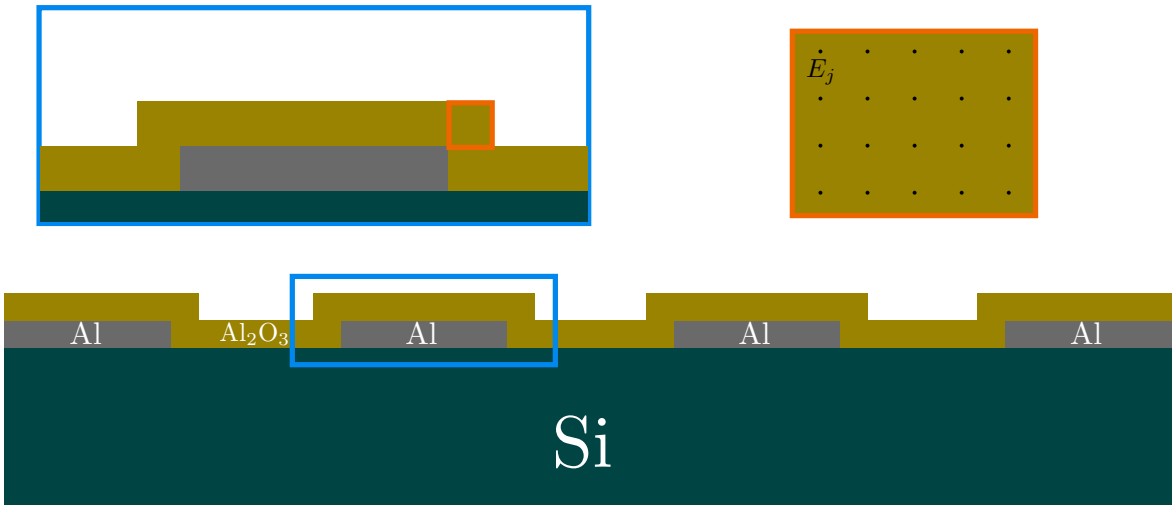

Figure 5.2: Diagram of capacitor cross section (not to scale). Values of the electric field E_j in the oxide layer are extracted from numerical simulations of the capacitor from a 2D spatial.

The histogram provides the probability $\mathcal{P}_j(E_j)$ of finding a particular value of the field E_j in the oxide region. The values are simulated for a specific voltage which is assigned to the capacitor. The magnitude of the electric field scales proportionally to the voltage on the capacitor. In terms of the electric field in the resonator, the loss can be expressed as a sum over bins in the histogram:

$$Q^{-1} = p_0 Q_0^{-1} \sum_j \mathcal{P}_j(E_j) \Big/ \sqrt{1 + (E_j/E_c)^2}, \tag{5.2}$$

where p_0 is the participation ratio of the layer. This can be viewed as simply a sum of TLS-like

terms for each different value of the electric field throughout the material, weighted appropriately by $\mathcal{P}_j(E_j)$. This form is not very convenient for experiments since voltage is naturally measured by a VNA, not the electric field. Equation (5.2) can be modified by introducing a factor which scales the value of the electric field determined from simulations to that which would be generated from a given capacitor voltage V. We have,

$$Q^{-1}(V) = p_0 Q_0^{-1} \sum_j \mathcal{P}_j(E_j) \Bigg/ \sqrt{1 + \left(\frac{V}{V_{\text{sim}}} \frac{E_j}{E_c}\right)^2}, \tag{5.3}$$

where V_{sim} is the voltage value used in simulations and E_j is the corresponding electric field.

5.1 Simulations of electric field in the capacitor

The geometry of the capacitor was simulated by two different methods. First, the electrostatic case was performed using COMSOL multiphysics AC/DC module where boundary conditions are specified and the electric field is computed by solving Poisson's equation. Second, a full microwave simulation was carried out using HFSS. In this case, the cross-sectional area of the capacitor was constrained to have a fine mesh in order to yield a smooth electric field profile at the level of a few 10s of nanometers. Imposing this resolution in 3D in HFSS results in a colossal amount of memory consumption, and is therefore not feasible given the resources at hand. The surface impedance boundary condition was also applied in HFSS to verify if it has any drastic effect on the field and the probability histograms. This condition did not yield a significant difference versus the case of a perfect electrical conductor. Furthermore, we find consistent agreement between COMSOL and HFSS for the various geometric variations considered in this work. Below we will present some examples for the relevant cases.

5.1.1 COMSOL simulations of the electric field distribution

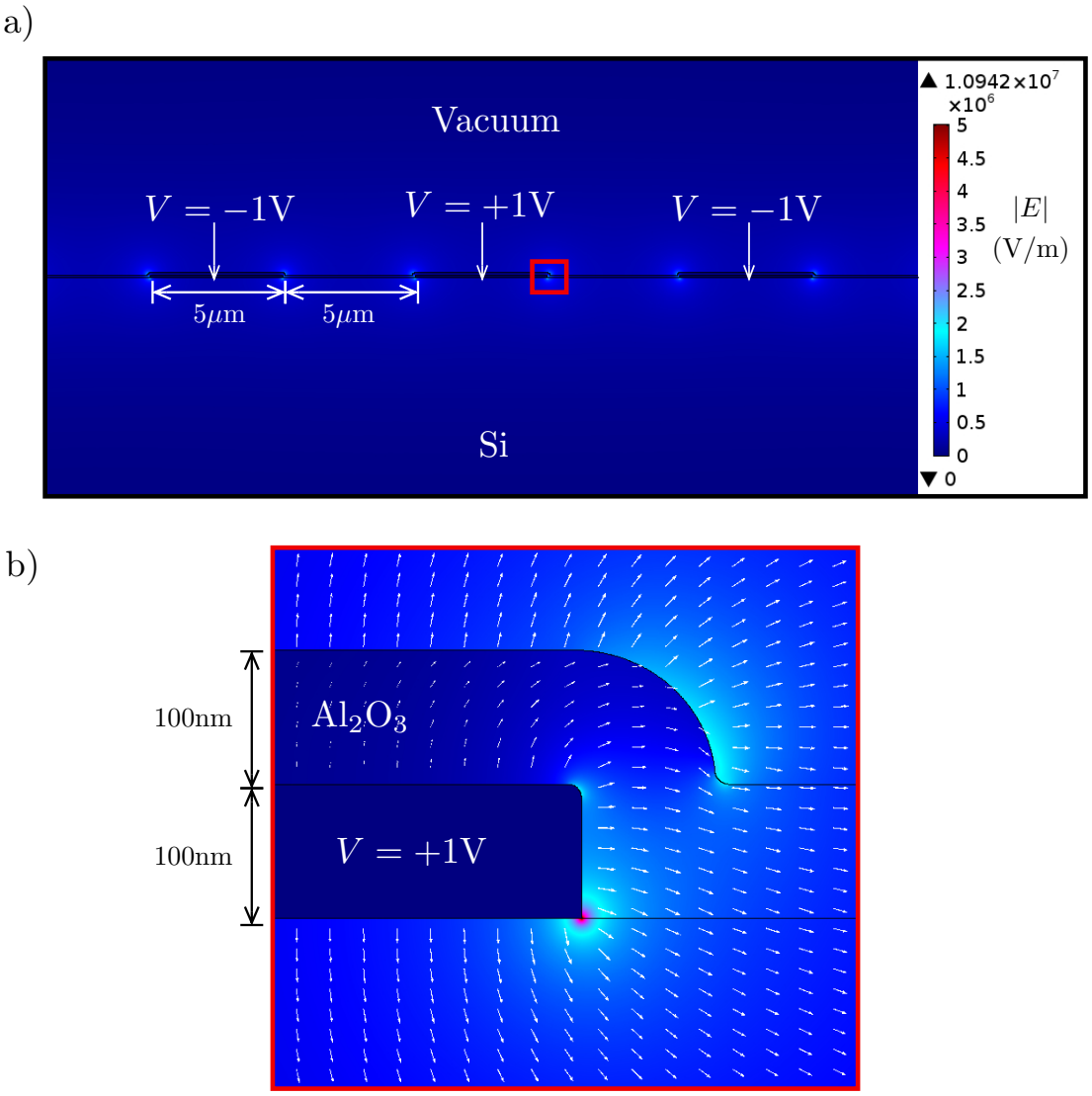

Figure 5.3: a) 2D plot of the electric field magnitude generated from a COMSOL simulation of the interdigital capacitor cross-section. b) Zoom of the region highlighted in a) illustrating the dielectric layer of Al_2O_3 and the spatial character of the field.

Figure 5.3 above shows the profile of the field for a capacitor with a 5 μm finger width and 5 μm gap. The field scales with the value of the voltage assigned to the capacitor finger. Figure 5.4 shows the normalized 1000-bin histograms for various capacitor geometries computed by sampling the value of the electric field over a 2 nm by 2 nm grid within the lossy oxide region.

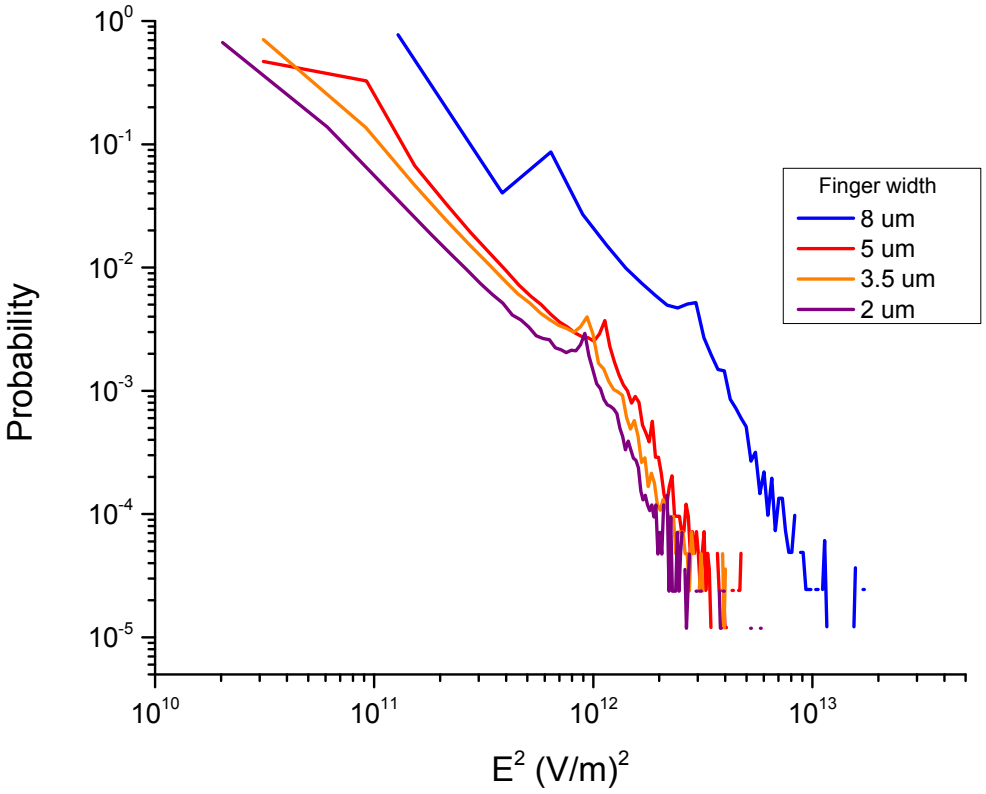

Figure 5.4: 1000-bin probability histograms of the electric field value for various capacitor geometries from COMSOL electrostatic simulations.

5.1.2 HFSS Results

3D microwave simulations are carried out in HFSS by constructing a capacitor with the same 2D geometric profile as that from the resonator. For the resonators considered, we only require a simulation of the field produced by a capacitor of the same characteristic geometry in 2D since we have assumed symmetry along the direction of the fingers. It is possible to simulate the full resonator, as discussed in chapter 3, however the resolution of the field at the level of the capacitor fingers ends up being rather coarse, due to the size of the model and limited computational resources. By simulating a smaller capacitor, it is possible to constrain the meshing to be fine near the surface of the capacitor as seen in Fig. 5.5.

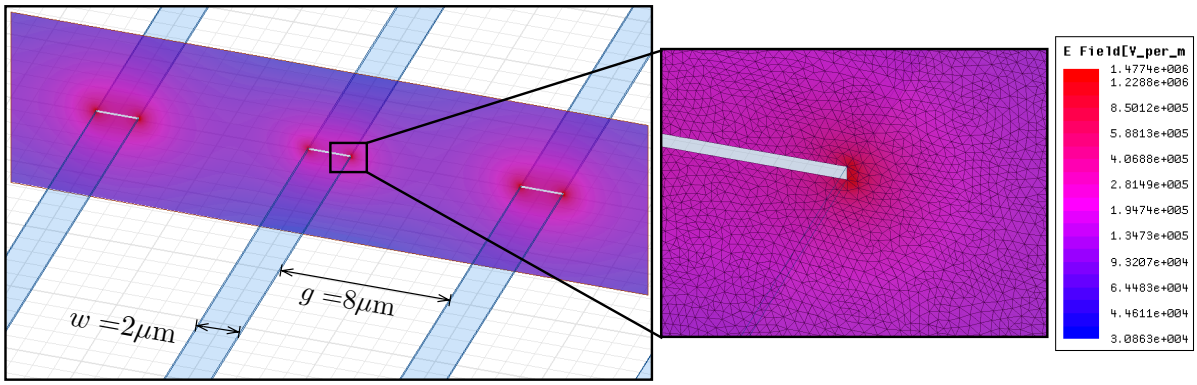

Figure 5.5: 3D view of HFSS capacitor model in which a 2-dimensional surface plot of the simulated electric field is shown. Also shown is a zoom of the highlighted region showing the fine surface mesh on the capacitor cross section to yield a smooth electric field profile over the regions of interest.

In HFSS, the oxide is also defined as a layered impedance boundary (see section 3.2) and is conformal to the metal and substrate surfaces. The field is then extracted from the 2D spatial grid and organized into a probability histogram. The electric field histograms for the HFSS results are presented below in Fig. 5.6 for various capacitor geometries and also with and without a superconducting surface impedance condition. By increasing the number of bins in the histogram, the resolution of the electric field probability improved, but creates more terms in equation 4.3 making the fitting procedure more tedious.

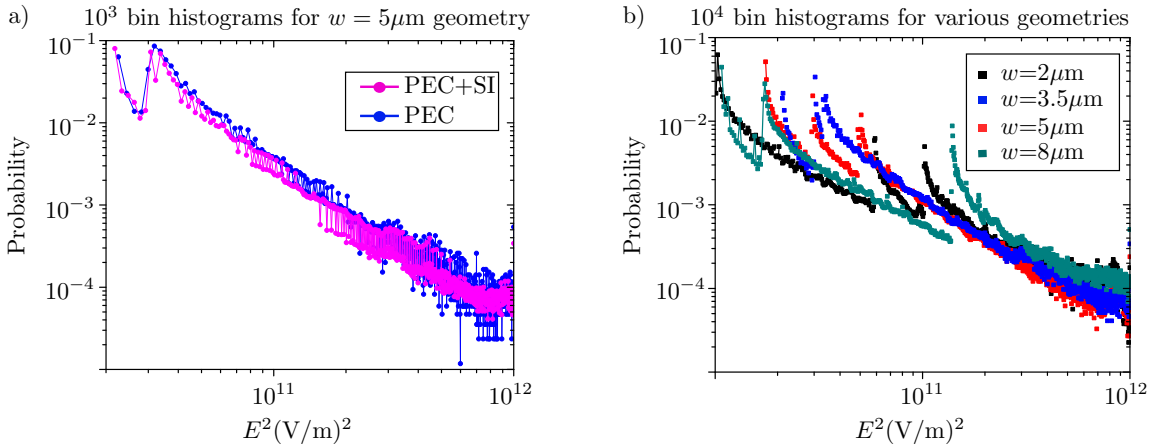

Figure 5.6: Plots of probability histograms from fields simulated in HFSS. a) 1000-bin histograms for 5 μm capacitor geometry comparing the case of a perfect electrical conductor with and without a surface impedance condition. b) Comparison of 10^4-bin histograms for different capacitor geometries.

5.1.3 Comparison between COMSOL and HFSS

To have confidence in the numerical results we compare the results for COMSOL and HFSS over a fixed bin range (upper and lower bounds of E). We find good agreement between the two types of simulations as seen in Fig. 5.7. Based on this COMSOL simulations results were used in the majority of the data analysis because model variations in geometry and oxide thickness are easier to implement than in HFSS. Also, when considering the effect of thin oxide layers, such as native oxides, meshing at the level of 1 nm is feasible in COMSOL. This will be discussed further in section 5.3.

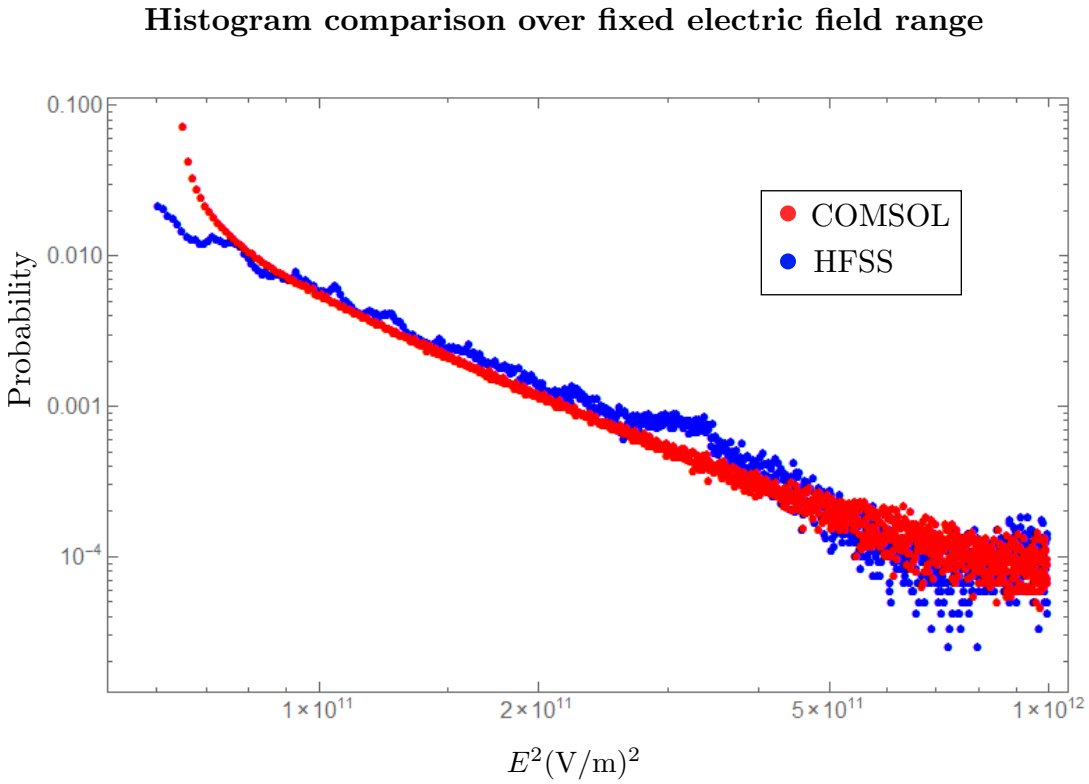

Figure 5.7: Comparison of COMSOL and HFSS 1000-bin histograms.

In order to obtain a good fit of equation (5.3) to experimental data, electric field histograms with at least 1000 bins were required. This made the fitting procedure tedious and the fitting parameters less accurate. This problem could be solved by requiring that the bins in the histogram each have equal probability. This means that all the terms in equation (5.3) would have equal weighting and the probability scales $(\#\text{ of bins})^{-1}$. This makes the fitting routine carried out in *Mathematica* [85] converge quicker for a smaller histogram. This slight modification does not change systematically the extracted values of Q_0^{-1} and E_c, and yields a better fit and reduces the standard error.

5.2 Dependence of dielectric loss on capacitor geometry

In this section, we apply the inhomogeneous field model to analyze loss measurements in ALD Al_2O_3. The oxide layer is 100 nm thick and was deposited on the surface of the device.

5.2.1 Measurements of W79-E4a

In this section, measurements and analysis of dielectric loss from device W79-E4a are presented. This device features four resonators, each with a geometric variation of the design given in Fig. 5.1. The superconducting material is aluminum and is 100 nm in thickness. By design, the variation in the capacitor geometry results in both a different total capacitance and resonance frequency, which allows for multiple resonators to be measured in our 2-port microwave setup. The coupling parameter λ is calculated using the approach presented in section 3.2.4. The circuit parameters are presented below in Table 5.1.

Resonator	ω_0 (GHz)	L (nH)	C (pF)	C_c (fF)	M (pH)	λ	Input Attenuation (dB)
LC1	5.955	1.25	0.57	2.4	10	0.0135	-76
LC2	7.154	1.25	0.45	2.4	10	0.0162	-78
LC3	7.967	1.25	0.32	2.4	10	0.0180	-81
LC4	9.009	1.25	0.25	2.4	10	0.0204	-84

Table 5.1: Design parameters for W79-E4a device: The four resonators LC1, LC2, LC3 and LC4 have a resonance frequency ω_0, geometric inductance L, intrinsic and coupling capacitances C and C_c respectively, mutual inductance M and coupling parameter λ. (see section 3.2.4) The input attenuation was determined experimentally for the setup at each frequency.

In the experimental setup, the input line attenuation is frequency dependent due to the material of the coaxial cables. Calculation of input line attenuation factor was presented in chapter 4 and the values in Table 5.1 are those determined therein. We now compare fitting the data with the two approaches outlined in this chapter. In the first, method 1, the data is fit to equation (5.1) where δ is a free fit parameter. In method 2, The electric field histograms from COMSOL simulations are used in conjunction with equation (5.3) to fit the data. The data is fit with a high-power loss factor Q_{hp}^{-1} which is due to non-equilibrium quasi-particles as discussed in chapter 3. Figure 5.8 shows the fits for method 2. We find the quality of the fits to be excellent, and furthermore, no additional fitting parameters are needed, which strengthens

the agreement with the TLS model. The values of the critical electric field E_c extracted from method 2 show a strong frequency dependence, which will be discussed in chapter 6 in context with measurements from other devices and its physical origin in terms of the TLS model. The product of the participation ratio and the intrinsic loss, $p_m Q_0^{-1}$, shows a slight dependence on frequency. This is a result of the variations in the capacitor geometry affecting the value of the participation ratio for the oxide layer. Once this factor is taken into account, Q_0^{-1} is found to be independent of frequency and given numerically by $\sim 2.0 \times 10^{-3}$ for ALD Al_2O_3.

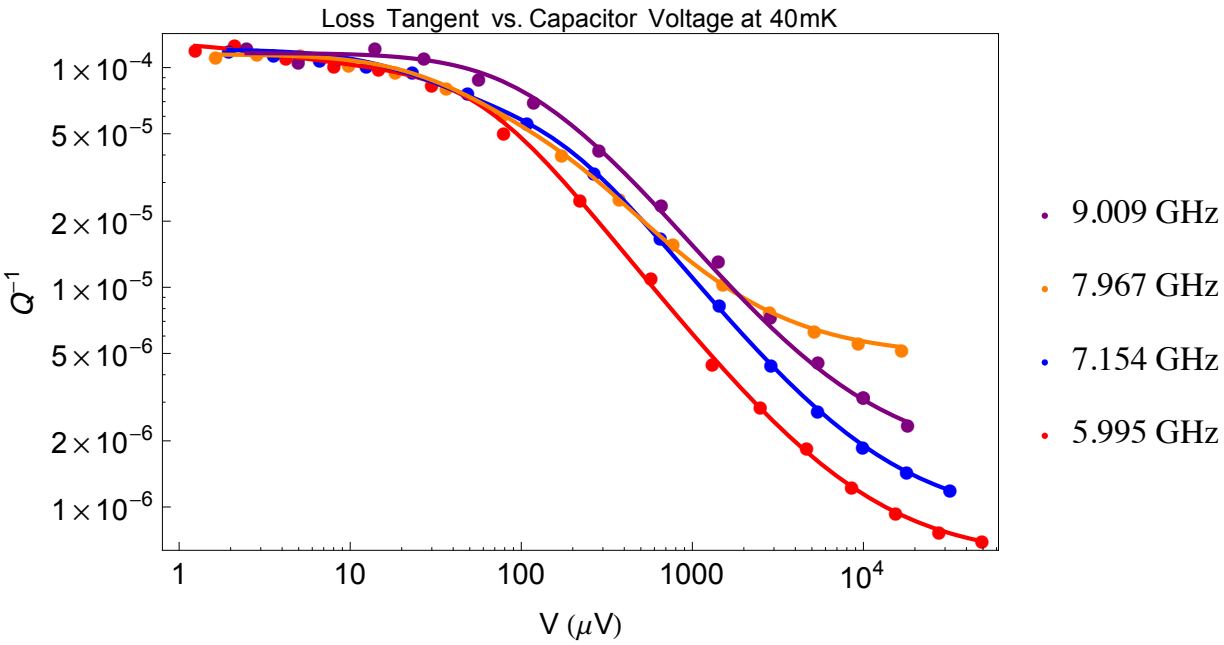

Figure 5.8: Loss ($Q^{-1} = p_0 Q_0^{-1}$) versus capacitor voltage for four resonators in device W79-E4a with contains 100 nm of aluminum oxide grown by atomic layer depositions. The intrinsic loss factor and the critical saturation field are extracted from the data by fitting with method 2 (equation (5.3)).

5.2.2 Comparison of fitting parameters

Here we present a complete comparison of the fitting parameters extracted from both methods. Analysis of the data using method 1 shows that δ depends on the geometry of the capacitor. We should not exclude the possibility that δ could depend on frequency, however this feature is

not a prediction of the TLS model. At the beginning of the chapter, it was established that a complete understanding of dielectric loss in a superconducting resonator must involve an account of the spatial profile of the field. By showing this for a set of similar resonators, we eliminated the need for δ, as can be seen by the quality of the fits in Fig. 5.8. This result demonstrates, unambiguously, strong agreement with the TLS model and, in turn, provides a sound method by which to determine the value of the critical field E_c. The high-power loss factor, Q_{hp}^{-1}, is also a free fitting parameter. For aluminum we find this factor to be constant for temperatures less than 300 mK, and quickly increasing at higher temperatures, characteristic of non-equilibrium quasiparticles [8].

Resonator	ω_0 (GHz)	w (μm)	g (μm)	δ	$p_m Q_0^{-1}$	Q_{hp}^{-1}
LC1	5.955	8	2	0.10	1.27×10^{-4}	5.66×10^{-7}
LC2	7.154	5	5	0.18	1.21×10^{-4}	9.02×10^{-7}
LC3	7.967	3.5	6.5	0.35	1.10×10^{-4}	5.05×10^{-6}
LC4	9.009	2	8	0.44	1.12×10^{-4}	1.79×10^{-6}

Table 5.2: Fitting parameters from method 1 (equation (5.1)) as discussed in the text. The resonance frequency is ω_0, the capacitor has a finger width w and spacing g, δ is the free parameter from equation 4.1, p_m is the participation ratio of the oxide layer with intrinsic loss Q_0^{-1} and Q_{hp}^{-1} is the high-power loss factor due to non-equilibrium quasiparticles.

Resonator	ω_0 (GHz)	w (μm)	g (μm)	E_c (V/m)	$p_m Q_0^{-1}$	Q_{hp}^{-1}
LC1	5.955	8	2	1.29	1.30×10^{-4}	5.85×10^{-7}
LC2	7.154	5	5	4.14	1.20×10^{-4}	8.68×10^{-7}
LC3	7.967	3.5	6.5	4.85	1.10×10^{-4}	4.86×10^{-6}
LC4	9.009	2	8	11.40	1.14×10^{-4}	1.65×10^{-6}

Table 5.3: Fitting parameters from method 2 (equation (5.3)) as discussed in the text. The resonance frequency is ω_0, the capacitor has a finger width w and spacing g, E_c is the critical electric field from equation 4.3, p_m is the participation ratio of the oxide layer with intrinsic loss Q_0^{-1} and Q_{hp}^{-1} is the high-power loss factor due to non-equilibrium quasiparticles.

5.3 Subtraction of baseline losses in niobium devices

Our consistent account of the inhomogeneous electric field profile may be applied to any type of resonator containing one or more dielectric layers, provided that the thickness and dielectric constant are known. For the purposes of measuring the temperature dependence of dielectric loss in ALD Al_2O_3 over a large temperature range, niobium based devices were used because of their larger transition temperature ($T_c \simeq 9$ K). Because of the larger value of T_c, dielectric losses in niobium devices remain the dominant source of loss for temperatures up to 1K. In the case of aluminum ($T_c \simeq 1.2$ K), however, superconducting loss begins to dominate around 300 mK, and the extraction of dielectric loss behaviour becomes less reliable. The difficulty with Niobium, in terms of dielectric losses, is that the films grown by sputtering are slightly lower in quality and the native oxide (usually Nb_2O_5) is thicker and perhaps lossier than native AlO_x. Also, it is much different chemically than our material of interest ALD Al_2O_3. Therefore, this native oxide will presumably have both a different intrinsic loss Q_0^{-1} and critical saturation field E_c. Since the measured internal quality factor includes contributions from all sources of loss, weighted appropriately by their participation factors, the loss due to a particular layer can only be quantified if the loss properties of the other layers are known. Therefore, to better understand the behaviour of dielectric loss in ALD Al_2O_3 layers deposited on niobium, we first measure the baseline losses due to native niobium oxide and analyze the results in terms of the inhomogeneous field model. This data is then used in the analysis of devices with ALD layers as a "baseline loss" factor.

5.3.1 Native oxide at the surface of niobium and silicon

Some assumptions must inevitably be made regarding the nature of the native oxides present on the device. In practice it is very challenging to measure the actual thickness, due to its very small value. It is important to have a good estimate, since the thickness will define the region over which the electric field probability will be considered. Literature [32] suggests that native niobium oxide will saturate at a thickness of ∼5 nm and native silicon will have a thickness of 2-5 nm [55]. We can assume both native niobium oxide and silicon oxide will be present on the device prior to deposition of any additional oxide which is to be characterized. It is also reasonable to assume each material is amorphous and will therefore host a distribution of two-level systems. It follows that we can model the loss in the resonator due to two different materials and consider

the electric field distributions for each. We can then write equation (5.3) for each material and fit the experimental data to

$$Q^{-1}(V) = \sum_{\substack{k=\mathrm{Nb_2O_5},\\ \mathrm{SiO_2}}} p_k Q_{0,k}^{-1} \sum_j \mathcal{P}_j(E_{j,k}) \Bigg/ \sqrt{1 + \left(\frac{V}{V_{\mathrm{sim}}} \frac{E_{j,k}}{E_{c,k}}\right)^2}, \tag{5.4}$$

where $Q_{0,k}^{-1}$ and $E_{c,k}$ are the loss factor and critical field for the k^{th} material. The histograms are generated from the simulation of the capacitor cross section shown below in Fig. 5.10. The electric field histograms are shown in Fig. 5.9 below.

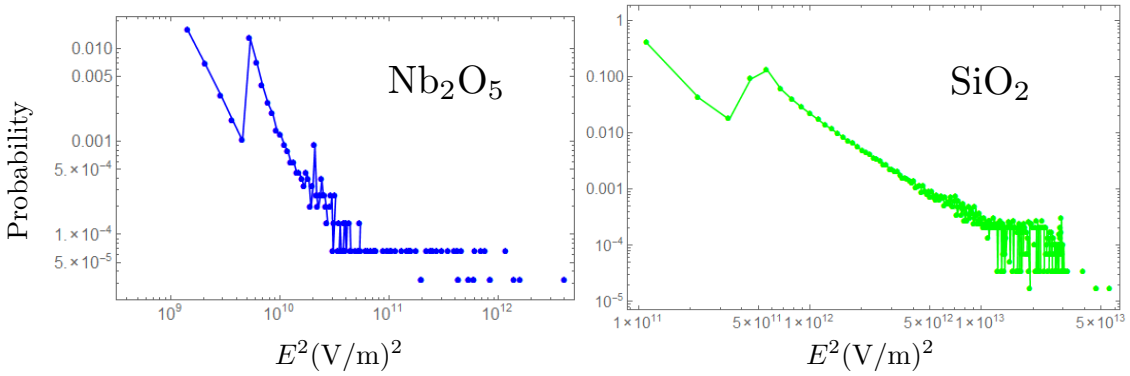

Figure 5.9: Electric field probability histograms for native oxides present in niobium based superconducting resonators. See figure 5.10 for simulation setup. The distributions are used in equation (5.4) to fit power dependent loss of baseline resonators.

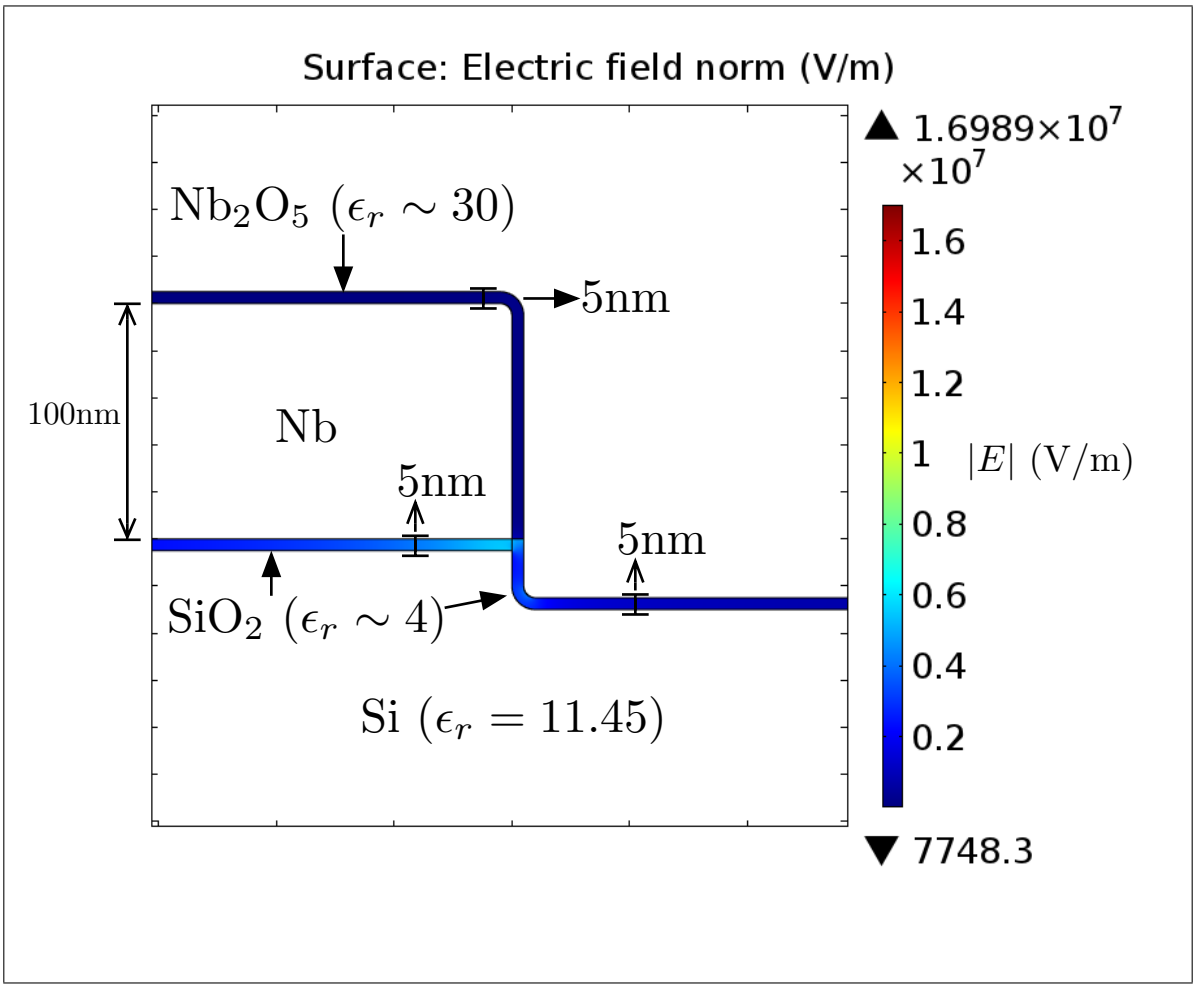

Figure 5.10: COMSOL native oxide simulation setup. Model includes over-etching into Si substrate resulting from reactive ion etching during fabrication. Silicon and niobium surfaces are assumed to have 5nm of SiO_2 and Nb_2O_5 respectively.

5.3.2 Voltage dependent loss in a baseline Nb resonator

The voltage dependent loss is fit to equation (5.4) with a high-power loss factor for the resonators of interest. It is worth mentioning that the data could not be fit to the TLS model by assuming only one native oxide. The weaker power dependence of the loss which was observed in the baseline devices is assumed to arise from the fact that the critical field of SiO_2 is quite large compared

to other oxides which have been characterized. This effectively weakens the power dependence because TLS present in SiO_2 are saturated at much higher fields than those in Nb_2O_5. The fitting of the data is presented below in Fig. 5.11.

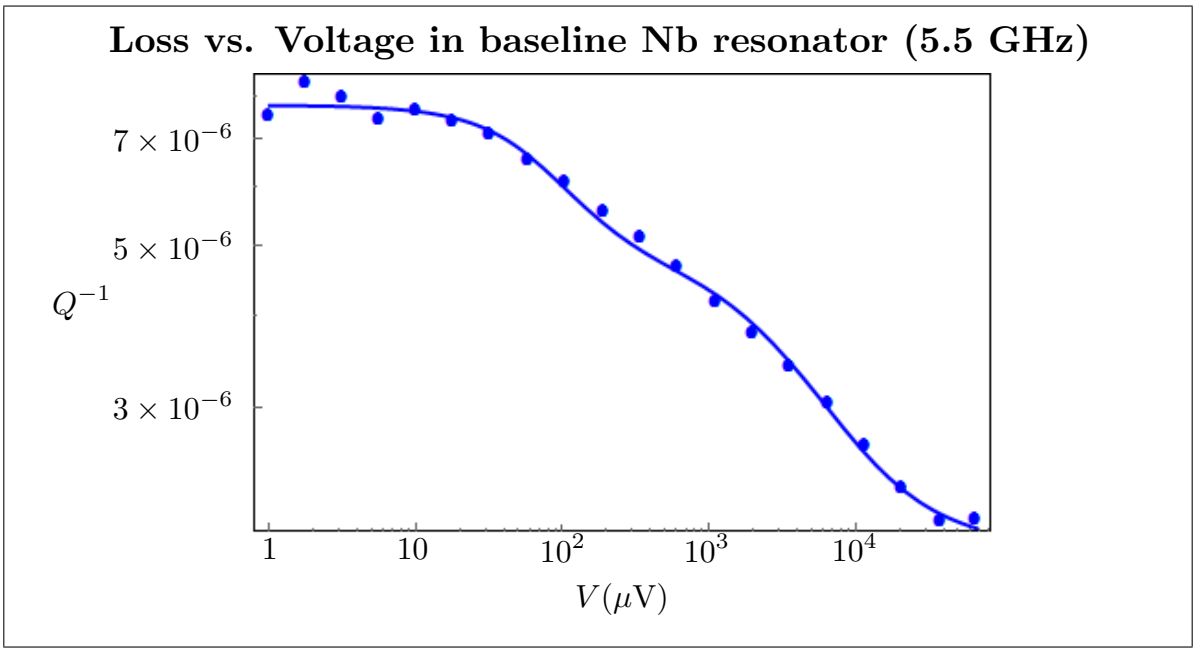

Figure 5.11: Loss versus resonator voltage in a bare 5.5 GHz Niobium resonator. Fitting model assumes two dielectric materials, Nb_2O_5 and SiO_2, each of which has their own TLS loss parameters.

The fitting parameters are presented below in Table 5.4. The values are those extracted from the best fit. We can see that the fit is by no means perfect, but it is sufficient for our purposes since it accounts for both the magnitude of the loss and the weak voltage dependence of the measurement to be understood in terms of two-level system loss. We note that, without the assumption of two different oxide materials, the inhomogeneous field model does not yield a good fit with the data.

The losses from devices which have additional thick amorphous layers are typically 1-2 orders of magnitude greater than that which is measured in the baseline line resonators. ($Q^{-1} \sim 10^{-4}$ for a device with a thick layer and $Q^{-1} \sim 10^{-6}$ for the device with no ALD layer.) Nonetheless, the small correction which is made by accounting for these native oxide surfaces affects the

extraction of the intrinsic loss and critical field in ALD Al_2O_3. This correction is significant for thin layers (∼30 nm) and small for thick layers (∼100 nm). We modestly point out that our COMSOL model is, of course, a simplification. In reality we do not know exactly the thickness, chemical composition and surface-morphological nature of the lossy surfaces. There could be some interfacial species between Nb and Si produced during the sputtering process which contributes to the loss. We assume that the O_2 plasma cleaning step in the ALD reactor produces thin, nearly uniform oxide layers on the surface which are similar chemically to the native oxides. What matters for the purpose of this work, is to account for the magnitude of the loss in a consistent manner.

Table 5.4: Fitting parameters for W60-C4d-LC1 (5.5 GHz)

Fit parameter	Nb_2O_5	SiO_2
Q_0^{-1}	3.34×10^{-6}	2.50×10^{-6}
E_c (V/m)	0.30	753
Q_{hp}^{-1}	1.93×10^{-6}	–

5.3.3 Corrected extraction of loss due to an additional thick oxide layer

The procedure for extracting loss in devices with additional thick oxide layers proceeds in the following way: For a given resonator design, the baseline loss is fit with equation (5.4) and the extracted fit parameters, $p_k Q_0^{-1}$ and $E_{c,k}$, are then taken as fixed quantities when fitting the data of a resonator containing an additional thick layer. Mathematically, we fit the data to the following expression

$$Q^{-1}(V) = \overbrace{\sum_{\substack{k=\mathrm{Nb_2O_5},\\ \mathrm{SiO_2}}} p_k Q_{0,k}^{-1} \sum_j \mathcal{P}_j(E_{j,k}) \Big/ \sqrt{1+\left(\frac{V}{V_{\mathrm{sim}}}\frac{E_{j,k}}{E_{c,k}}\right)^2}}^{p_k Q_0^{-1} \text{ and } E_{c,k} \text{ fixed from baseline resonator fitting}} + \ldots \quad (5.5)$$

$$+ \underbrace{p_0 Q_0^{-1} \sum_j \mathcal{P}_j(E_j) \Big/ \sqrt{1+\left(\frac{V}{V_{\mathrm{sim}}}\frac{E_j}{E_c}\right)^2}}_{\text{fitting expression for } Al_2O_3 \text{ loss}}.$$

The first term is the correction factor which accounts for native oxide layers, and the second term pertains to loss in the additional layer. As an example, Fig. 5.12 shows the fitting of loss vs. voltage data for a resonator which includes 60 nm of ALD Al_2O_3. The $\mathcal{P}_j(E_j)$'s are given by the histogram below in Fig. 5.13. The resonator is identical in design to the baseline resonator discussed earlier and is therefore very close in frequency. It is important to note that, without including the native oxide surfaces in the baseline loss model, the inhomogeneous field model fails to provide a good fit of the data. Therefore, convincing agreement with the TLS model cannot be so easily claimed. In other words, the presence of these lossy layers in addition to the thick layer of interest imposes additional inhomogeneity in the electric field, and therefore affects the voltage dependent loss. The high-power loss factor Q_{hp}^{-1} is always treated as a free fitting parameter for a given resonator.

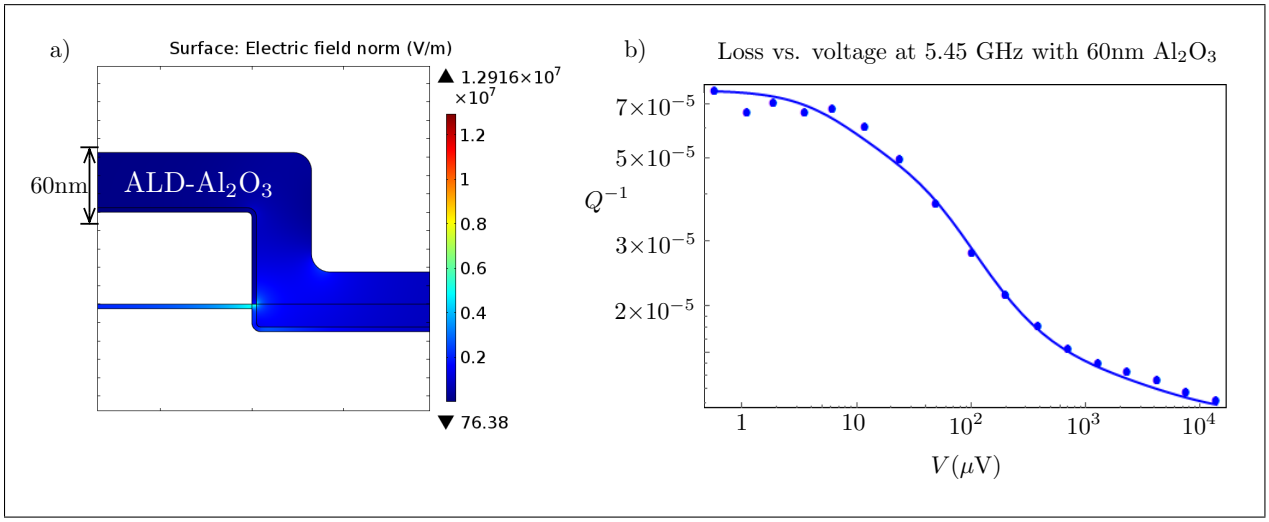

Figure 5.12: a) electric field profile from COMSOL simulations. Model includes native oxide surfaces and also 60 nm of ALD Al_2O_3. b) Voltage dependent loss in a 5.45 GHz resonator fit using equation 5.5 with fixed baseline parameters and free Al_2O_3 parameters given in 5.5.

Table 5.5: Fitting parameters for W60-C4f-LC1 (5.45 GHz)

Fit parameter	Al_2O_3
$p_0 Q_0^{-1}$	6.00×10^{-5}
E_c (V/m)	0.87
Q_{hp}^{-1}	1.01×10^{-5}

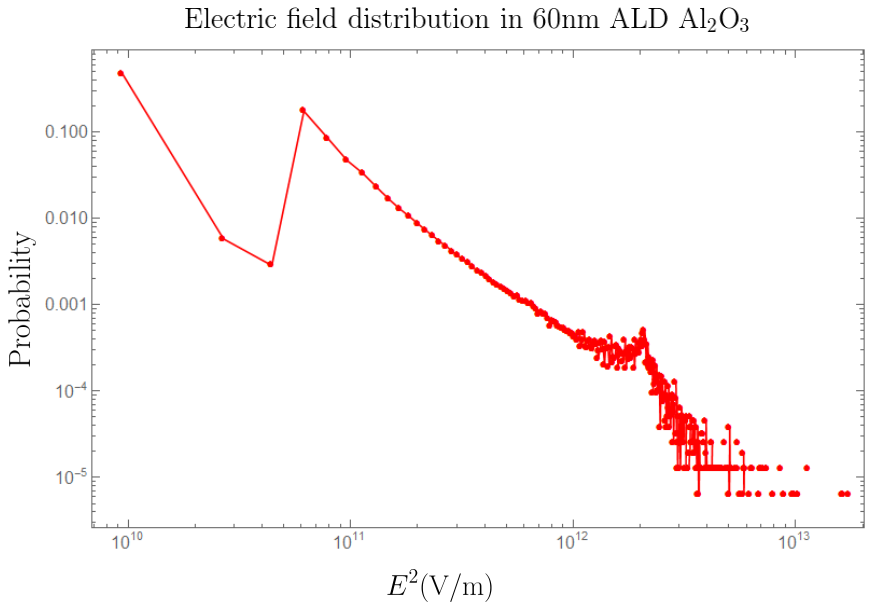

Figure 5.13: electric field probability distribution determined from COMSOL simulations.

Chapter 6

Temperature dependence measurements of dielectric loss in ALD aluminum oxide

6.1 Introduction

In this chapter, we present an extensive set of measurements of dielectric loss in aluminum oxide grown by atomic layer deposition. Aluminum oxide is currently one of if not *the* most important material used in superconducting circuits as it forms the tunnel oxide barrier of the most extensively used type of Josephson junction, namely, a superconductor-insulator-superconductor (SIS) junction, consisting of an Al/AlO_x/Al tri-layer. This type of junction is commonly used because it can be fabricated using a double-angle evaporation recipe with an intermediate *in-situ* oxidation step. This recipe allows for the sample to remain under vacuum during the deposition and oxidation which in turn yields a high-quality oxide barrier and large critical current, key parameters in the fabrication of superconducting qubits. Therefore, knowledge of the properties of this amorphous oxide is of great interest both in terms of improving device designs and fabrication methods. The measurements are performed over the temperature range of tens of mK to 1 K, thus providing a large domain over which the central predictions of the TLS model are tested. The richest features of the TLS model reside in the behaviour of the low-power loss tangent and the critical electric field, which reflect specifically the two-level character of the

tunnelling systems and the environmental mechanisms contributing to decoherence, respectively. The second property in particular, for the case of aluminum oxide, has not been characterized over an extensive temperature range.

The study is based on many resonators, varying in design, dielectric oxide layer thickness and resonance frequency. For this reason, it was essential to have a consistent analysis method which allowed for reliable extraction of the relevant loss parameters for resonators with varying characteristics and microwave properties. In chapter 3, a systematic analysis method for fitting the microwave response of an arbitrary lumped element resonator was presented. The method provided a way to determine the capacitor voltage on resonance, by combining estimates of the coupling to the transmission line with parameters obtained directly from fitting the microwave transmission data acquired from a vector network analyzer. Using this estimate of the capacitor voltage, the model presented in chapter 5 is applied to analyze the dielectric loss measurements and determine the value of the critical electric field.

Two different types of resonators were studied in this work. Interdigital resonators, which were discussed at length in the previous chapter, and also resonators consisting of an overlap parallel plate capacitor. Interdigital resonators can easily be fabricated completely out of niobium, which is ideal for measurements at higher temperatures. Furthermore, due to the geometry of the capacitor and the small participation ratio of the amorphous oxide layers, loss measurements are faster to conduct in terms of total measurement time. This is due to the fact that the high internal quality factors result in an improved signal-to-noise ratio (SNR) for microwave measurements. This feature allows for fewer averages per measurement and is essential for experiments above 300 mK. This is because the temperature may be easily kept constant over the duration of a measurement ($\sim$12 minutes) in which a VNA trace is acquired at each microwave power. However, the low participation ratio makes the effect of dielectric loss smaller, and therefore more difficult to distinguish from other sources of loss such as loss due to quasiparticles.

On a typical device, 3 or 4 resonators of varying geometry and resonance frequency are coupled to the signal line, which allows loss at various frequencies to be compared. The second type of resonator, the "overlap" type, consists of a simple parallel-plate capacitor where the aluminum oxide layer has been deposited between the plates. These resonators were studied because the capacitor produces a homogeneous electric field, and also the participation ratio of the dielectric is very close to 1, thus ensuring a reliable loss measurement. The large dielectric participation factor of the oxide yields a lower internal quality factor and in turn a lower SNR

which increases the duration of a measurement. Due to limitations in fabrication, the top plate of the capacitor needed to be made of aluminum, by metal evaporation and lift-off steps in the fabrication process. Therefore, loss measurements with overlap resonators were limited to lower temperatures to reduce the impact of superconducting loss in aluminum.

Table 6.1 shows a summary of the different devices which were measured in this work. Extensive measurements using different types of resonators are important both in verifying the reproducibility of our results and also ruling out systematic features of the measurements. In section 6.2, we will outline in detail the analysis procedure for a set of resonators in a single device, emphasizing the relevant methods, physics and results of interest. In section 6.3 a summary of the results from other devices will be presented to illustrate the reproducibility of the results. In section 6.4, we will discuss the results in full and present a unique characterization of the intrinsic loss factor and critical saturation field due to two-level systems in amorphous dielectrics. We will compare our results for ALD aluminum oxide with those for another type of aluminum oxide grown by plasma oxidation. Based on the data for the critical field, we analyze the intrinsic properties of TLS coherence in comparison with other measurements made using quantum bits.

Table 6.1: Measurement summary for dielectric loss in Al_2O_3 grown by atomic layer deposition

Device	# Resonators	Type	Al_2O_3 thickness (nm)	Metal	Temperatures (mK)
W60-C4d	3	Interdigital	none	Nb	40 - 925
W60-C4h	3	Interdigital	30	Nb	40 - 800
W60-C4f	3	Interdigital	60	Nb	46 - 990
W60-C5b	3	Interdigital	100	Nb	50 - 820
W79-E4a	4	Interdigital	100	Al	40 - 280
W60-A2d	3	Overlap	30	Al/Nb	50 - 590
W60-B2h	3	Overlap	60	Al/Nb	47 - 180

6.2 Characterization of dielectric loss in 100 nm ALD Al_2O_3

In this section we present a detailed analysis of device W60-C5b for the purpose of demonstrating the analysis method which was used for all devices considered in this work. The oxide layer is 100 nm in thickness and the superconducting material is niobium with a thickness of 100 nm. The device consists of three interdigital resonators which have frequencies at 5.47, 6.01 and 7.14 GHz.

6.2.1 Voltage dependent loss measurements

The internal quality factor is extracted from fitting the traces acquired using a VNA with equation 3.19. Figure 6.1 shows an example of the amplitude and phase of the microwave response measurement at low and high-power to illustrate the quality of the fits to equation 3.19. At each power, the microwave response is fit and the internal Q-factor is determined. The inverse internal Q-factor is equal to the intrinsic loss tangent for the aluminum oxide times the participation ratio, $p_0 Q_0^{-1}$ which is plotted as a function of capacitor voltage for various temperature in Fig. 6.2. Figure 6.2 illustrates a typical set of temperature dependence measurements of the internal quality factor of a superconducting resonator in a dielectric loss experiment. At each temperature, the resonator is measured at 14−17 different microwave powers corresponding to a capacitor voltage range of 1 μV to 4×10^4 μV determined using the method presented in section 3.1.2.

6.2.2 Subtraction of baseline losses

In section 5.3, we addressed the issue that, for most planar superconducting resonators, there are additional dielectric layers in the form of native oxides at the surface of the substrate and superconducting material. In this device consisting of niobium on a silicon substrate, there are NbO_x and SiO_x layers contributing to the total loss in the resonator. To account for these sources of loss, we measure the temperature dependence of the loss for a device which has no additional aluminum oxide layer (device: W60-C4d, see Table 6.1). At each temperature, the

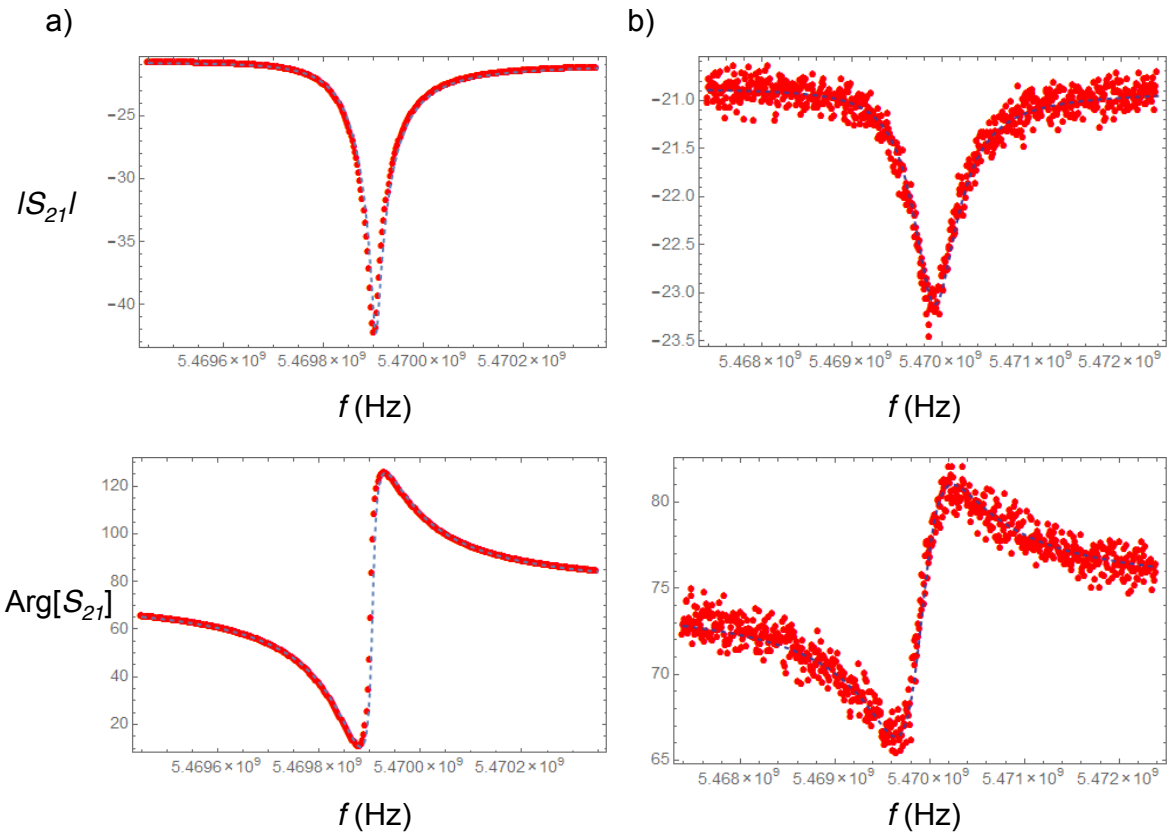

Figure 6.1: Amplitude (top) and phase (bottom) of a microwave transmission measurement of a superconducting resonator at high (right) and low (left) powers. The data is acquired using a 2-port vector network analyzer and fit to equation 3.19. a) Amplitude and phase of the microwave response at -85 dBm. b) Amplitude and phase of the microwave response at -130 dBm.

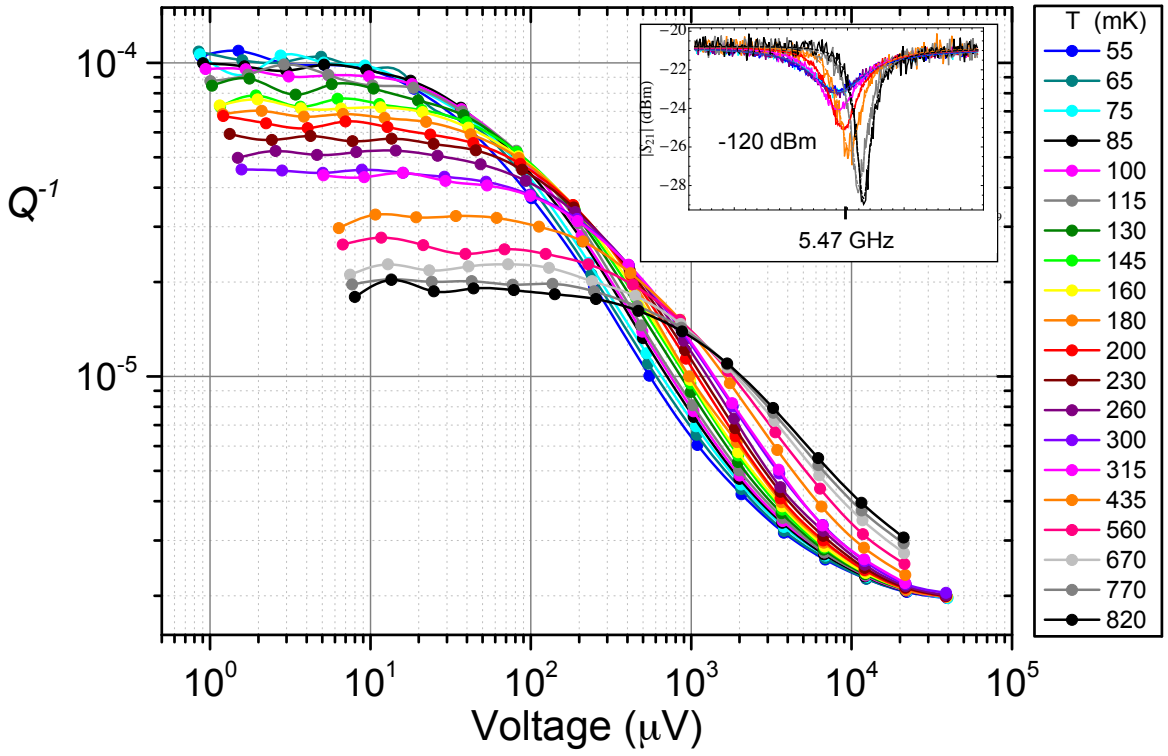

Figure 6.2: Dielectric loss vs capacitor voltage at various temperatures in a 5.47 GHz interdigital resonator with 100 nm of ALD Al_2O_3. Inset: microwave response at a fixed low power (-120dBm) at various temperatures illustrating the temperature dependence of the internal-Q and resonance frequency.

voltage dependent loss data is fit to the following expression

$$Q^{-1}(V,T) = \sum_{k=\substack{\mathrm{Nb_2O_5},\\ \mathrm{SiO_2}}} p_k Q_{i,k}^{-1}(\omega,T) \sum_j \mathcal{P}_j(E_{j,k}) \Bigg/ \sqrt{1+\left(\frac{V}{V_{\mathrm{sim}}}\frac{E_{j,k}}{E_{c,k}(T)}\right)^2} + Q_{hp}^{-1}, \tag{6.1}$$

where $Q_{i,k}^{-1}$ is the intrinsic loss, p_k is the dielectric participation ratio, $\mathcal{P}_j(E_{j,k})$ is the probability for the value of the electric field $E_{j,k}$ to be found in the volume of the k^{th} material, V_{sim} is the reference voltage value from numerical simulations, $E_{c,k}$ is the critical electric field and Q_{hp}^{-1} is a high-power constant loss term. From fitting the internal loss versus voltage data for the corresponding resonator to the model, we obtain values for the loss tangents and critical fields over a broad temperature range shown in Fig. 6.3. The behaviour of the loss tangents were analyzed by fitting to the prediction from the TLS model

$$Q_{i,k}^{-1}(\omega,T) = p_k Q_{0,k}^{-1} \tanh(\hbar\omega/2k_BT), \tag{6.2}$$

where $\omega = 2\pi f$ is the angular frequency. We find good agreement with this temperature dependent form of the loss. In our analysis, we also consider an alternative model [80] for a disordered solid which predicts a temperature dependence for the intrinsic loss given by

$$Q_{i,k}^{-1}(\omega,T) = p_k Q_{0,k}^{-1} \left(1 - \exp(-\hbar\omega/k_BT)\right). \tag{6.3}$$

This model was developed by Vural and Leggett to explain the universal behaviour of the acoustic version of Q_0^{-1} which has been observed in many materials [67]. The model makes no explicit assumption about the "two-level" nature of the tunnelling system. Vural and Leggett modestly assume that the "extra" degrees of freedom in an amorphous material are described by a generic many-body density of states, and that elastic phonons mediate a mutual interaction between tunnelling systems.

Table 6.2: Fitting parameters for baseline losses in W60-C4d at $T = 40$ mK

Resonator	f_r (GHz)	$p_{\mathrm{Nb_2O_5}} Q_{0,\mathrm{Nb_2O_5}}^{-1}$	$p_{\mathrm{SiO_2}} Q_{0,\mathrm{SiO_2}}^{-1}$
LC1	5.58	3.25×10^{-6}	2.53×10^{-6}
LC2	7.26	3.31×10^{-6}	2.68×10^{-6}

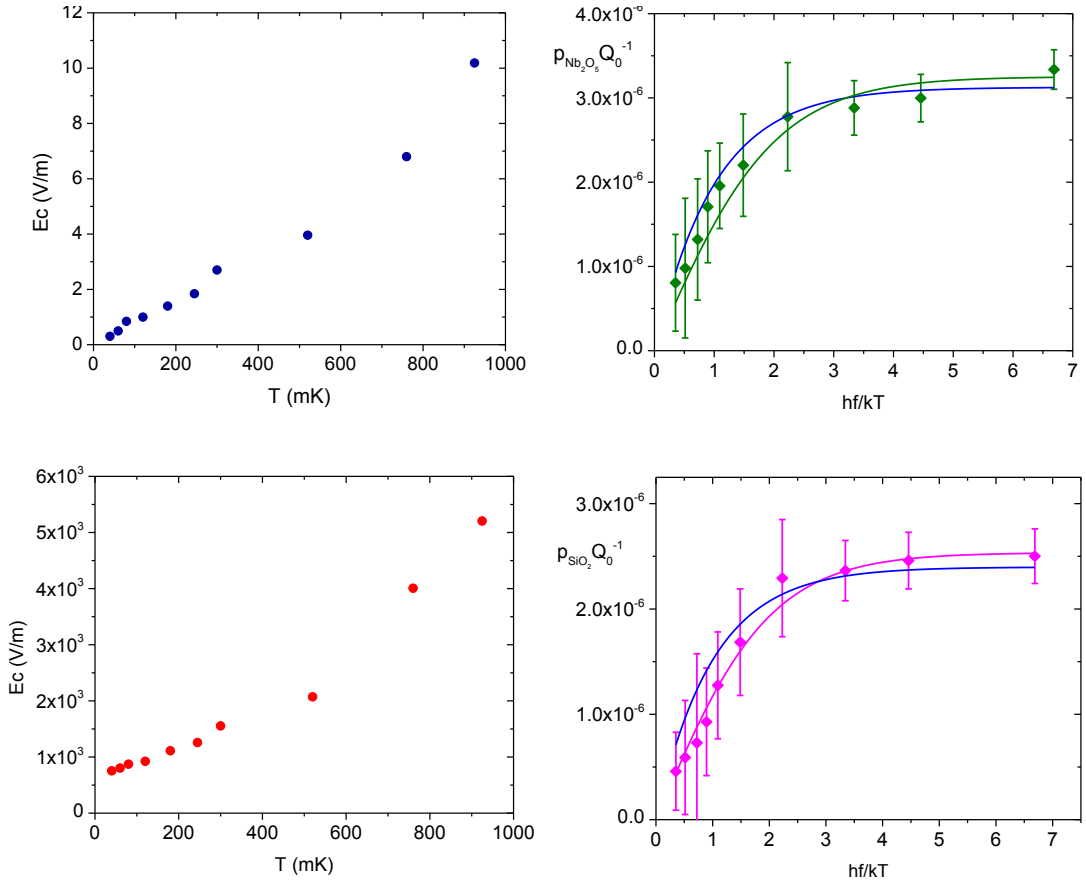

Figure 6.3: Critical electric field data (left) and intrinsic losses (right) from native Nb_2O_5 (top) and SiO_2 (bottom) layers at 5.58 GHz. Values are extracted using the inhomogeneous field model assuming 5 nm Nb_2O_5 on metal surfaces and 5 nm SiO_2 on substrate surfaces. On the right side of the figure, the solid line which matches the colour of the data points is the fit to the TLS model (equation (6.2)) and the blue solid line is the fit to the disordered solid model (equation (6.3)).

The relevant loss parameters are presented in Table 6.2. We find good agreement in the numerical values of the extracted fitting parameters between the two resonators at different frequencies. It is important to note that, since we do not know precisely the participation ratio of the niobium oxide and silicon oxide layers, we can only determine the magnitude of the loss, i.e, the products $p_{\mathrm{Nb_2O_5}} Q^{-1}_{0,\mathrm{Nb_2O_5}}$ and $p_{\mathrm{SiO_2}} Q^{-1}_{0,\mathrm{SiO_2}}$ respectively. This is sufficient since we only need to know the magnitude of these losses, not their intrinsic loss tangents for each material, so that they may be accounted for in a measurement involving additional thicker layers.

The set of values for the losses and critical fields at each temperature are interpolated to give approximate functions of temperature. This is important because in different experiments involving temperature dependence measurements, it is difficult to achieve the same set of temperatures. By using interpolated functions for the losses and critical fields, we can approximately determine the correct values for any temperature at which a later measurement is performed to determine the loss due to an additional layer of aluminum oxide.

6.2.3 Extraction of loss due to aluminum oxide

Using the data presented in the previous section describing the loss from native oxides, we are equipped to determine the intrinsic loss in aluminum oxide by following the procedure presented in section 5.3.3. We fit the loss data presented in Fig. 6.2 to the following equation

$$\begin{aligned} Q^{-1}(V,T) &= \sum_{k=\substack{\mathrm{Nb_2O_5},\\ \mathrm{SiO_2}}} p_k Q^{-1}_{i,k}(\omega,T) \sum_j \mathcal{P}_j(E_{j,k}) \Bigg/ \sqrt{1+\left(\frac{V}{V_{\mathrm{sim}}}\frac{E_{j,k}}{E_{c,k}(T)}\right)^2} + \dots \\ &+ p_0 Q_i^{-1}(\omega,T) \sum_j \mathcal{P}_j(E_j) \Bigg/ \sqrt{1+\left(\frac{V}{V_{\mathrm{sim}}}\frac{E_j}{E_c(T)}\right)^2} + Q^{-1}_{hp}, \end{aligned} \tag{6.4}$$

where the first term accounts for losses from native oxides and the second term describes the loss from the aluminum oxide layer. The terms $p_k Q^{-1}_{i,k}(\omega,T))$ and $E_{c,k}(T)$ are specified by the interpolated values determined from the native oxide losses of the baseline resonator.

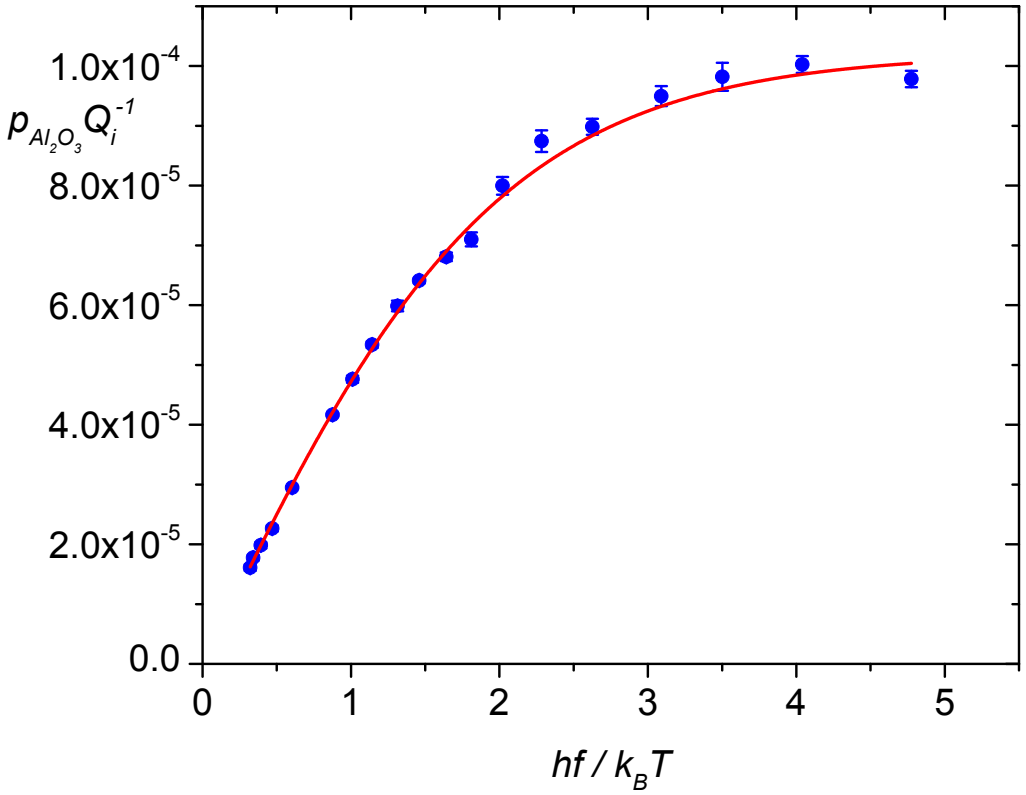

Figure 6.4: Intrinsic low power loss in Al_2O_3 grown by atomic layer deposition determined using a niobium interdigital resonator with a resonance frequency of $f = 5.47$ GHz. The solid line represents the fit to the TLS model prediction.

6.2.4 Low-power loss

Figure 6.4 shows the temperature dependence of the low-power intrinsic loss. The data is obtained from fitting the voltage dependent data to equation (6.4), extracting $p_0 Q_i^{-1}$ and fitting the expression to equation (6.2). Table 6.3 shows the values of the intrinsic loss Q_0^{-1} determined using two different resonators. The agreement we find with the TLS model is outstanding. Other works have conducted loss measurements in aluminum oxide [52] and silicon oxide [49] over a similar temperature range. However, their measurements were for thin oxide layers for which they do not calculate the participation ratio and therefore do not determine the intrinsic loss tangent. Furthermore, they address neither the effect of an inhomogeneous electric field nor the losses from native oxide surfaces. Measurements of dielectric loss in ALD aluminum oxide have been made [42], but no data on the temperature dependence is presented.

Table 6.3: Fitting parameters for loss and critical field in 100nm Al_2O_3

Resonator	f_r (GHz)	Q_0^{-1}
LC1	5.47	2.12×10^{-3}
LC2	7.14	2.05×10^{-3}

6.2.5 Frequency shift

Another way to extract the intrinsic loss factor is by measuring the shift in the resonance frequency as a function of temperature (see section 2.4). Data for the resonance frequency as a function of temperature is presented below in Fig. 6.5 and the relevant fit parameters in Table 6.4. We find excellent agreement with the TLS model over the temperature range which was characterized. The frequency as a function of temperature is fit to the following equation derived from section 2.4

$$\frac{f_r(T)}{f_r(T=0)} = 1 + 2\left(\sum_k p_k Q_{0,k}^{-1} + p_0 Q_0^{-1}\right)\left(\mathrm{Re}\mathcal{D}\left(\frac{1}{2} - \frac{\hbar\omega}{2\pi i k_B T}\right) - \ln\left(\frac{\hbar\omega}{2\pi k_B T}\right)\right), \tag{6.5}$$

where $\mathcal{D}$ is the complex digamma function and $f_r(T=0)$ is a fitting parameter corresponding to the expected frequency at zero temperature. The values for $p_k Q_{0,k}^{-1}$ are those determined from the baseline devices with losses due to niobium oxide and silicon oxide. The inclusion of these

factors gives rise to a small change in the value of Q_0^{-1}, since its participation ratio is much larger. The fits are in excellent agreement with the TLS model prediction, over a significant temperature range.

Table 6.4: Fitting parameters for temperature dependent frequency shift in W60-C5b

Resonator	$f_r(T=0)$ (GHz)	Q_0^{-1}
LC1	5.47030	2.73×10^{-3}
LC2	7.13785	2.65×10^{-3}

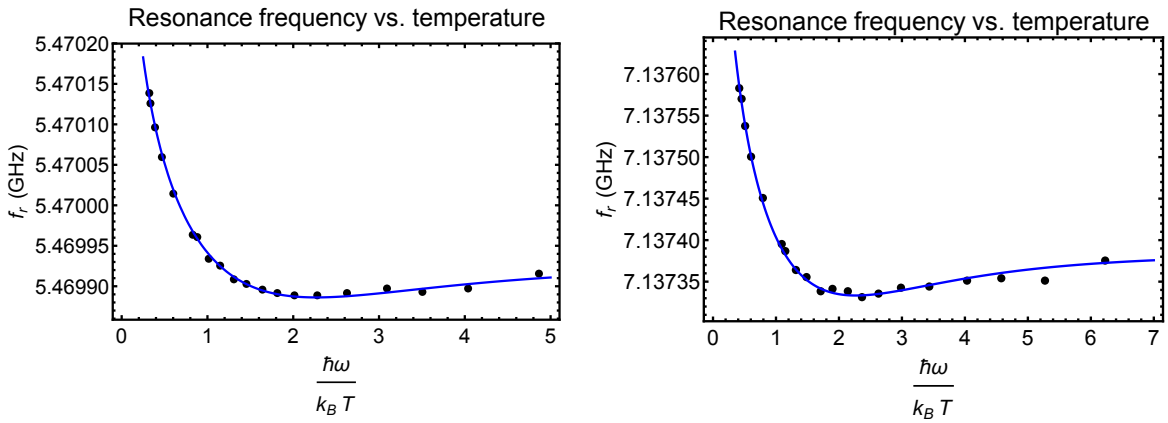

Figure 6.5: Resonance frequency versus temperature for two niobium interdigital resonators with 100 nm of ALD aluminum oxide at frequencies of 5.47 anf 7.14 GHz. The data points are fit to the prediction of the TLS model given by equation (6.5).

By averaging the results for the loss obtained from both methods, we find a loss tangent of $Q_0^{-1} = 2.39 \pm 0.35 \times 10^{-3}$ for Al_2O_3 grown by atomic layer deposition. A further discussion of this value will be conducted in section 6.4 when all measurements are considered.

6.2.6 Analysis of the critical electric field

The analysis of the voltage dependent loss using equation (6.4) provides the temperature dependent behaviour of E_c, the critical electric field in aluminum oxide. To understand the behaviour

of the critical field, we recall the form of equation (2.94) given by the TLS model

$$E_c(T) = \frac{\sqrt{3}\hbar}{2qd_0\sqrt{T_{1,m}(T)T_2(T)}}, \tag{6.6}$$

where $T_{1,m}$ is the mininum TLS lifetime limited by single phonon emission, and T_2 is the TLS dephasing time. Both $T_{1,m}$ and T_2 are assumed to depend upon temperature. Using $T_1^{-1} = \Gamma_1, T_2^{-1} = \Gamma_2 = \frac{1}{2}\Gamma_1 + \Gamma_\phi$ we have

$$E_c = \frac{\sqrt{3}\hbar}{2qd_0}\sqrt{\Gamma_{1,m}\Gamma_2} = \frac{\sqrt{3}\hbar}{2qd_0}\sqrt{\Gamma_{1,m}\left(\frac{1}{2}\Gamma_{1,m} + \Gamma_\phi\right)}, \tag{6.7}$$

where qd_0 is the average dipole moment of the TLS. We assume $q = e$ and $d_0 = 0.1$ nm, and that Γ_1 is given by the expression for single phonon relaxation process (equation (2.49)). The behaviour of Γ_ϕ reflects the dephasing of the TLS, and is believed to arise as a result of TLS-TLS interactions [65]. The temperature dependent behaviour of Γ_ϕ has not been characterized for an ensemble of TLSs using measurements of the critical field determined using a superconducting resonator. We may assume Γ_ϕ has a general temperature dependent form given by $\Gamma_\phi = aT^\mu$. Equation (6.7) then reads

$$E_c(T) = \frac{\sqrt{3}\hbar}{2qd_0}\sqrt{\Gamma^0_{1,m}(\omega)\coth\left(\frac{\hbar\omega}{2k_BT}\right)\left(\frac{1}{2}\Gamma^0_{1,m}(\omega)\coth\left(\frac{\hbar\omega}{2k_BT}\right) + aT^\mu\right)}, \tag{6.8}$$

where $\Gamma^0_{1,m}(\omega)$ is the maximum relaxation rate at $T = 0$. It is given by

$$\Gamma^0_{1,m}(\omega) = \left(\sum_{\alpha=\ell,t}\frac{\gamma_\alpha^2}{v_\alpha^5}\right)\frac{\omega^3}{2\pi\rho\hbar}, \tag{6.9}$$

where γ_α is the TLS-phonon coupling energy, v_α is phonon velocity and the sum over $\alpha = \ell, t$ accounts for relaxation via both longitudinal (ℓ) and transverse (t) phonons. In Fig. 6.6 we fit the critical field data in Al_2O_3 obtained for the two resonators considered in this device. From the fitting, we determined the fitting parameters which are tabulated in Table 6.5. The critical field data provides a way to indirectly measure the coherence properties of two-level systems in amorphous materials. By fitting the temperature dependent data, one infers the *ensemble averaged* coherence properties of the two-level systems. This provides an important

f_r (GHz)	$\Gamma^0_{1,m}$ (kHz)	a (MHz/K$^\mu$)	μ
5.47	45.3	6.86	2.68
7.14	81.1	17.5	2.15

Table 6.5: Fitting parameters for the critical field in 100 nm Al_2O_3 for two different resonators with resonance frequency f_r. $\Gamma^0_{1,m}$ is the intrinsic "zero-temperature" maximum relaxation rate, a is the coefficient of the temperature dependent form for a pure dephasing process given by $\Gamma_\phi = aT^\mu$.

comparison to experiments conducted on single two-level systems using qubits [76, 50]. Following the presentation of the full experimental data set from all devices, the details of the TLS coherence properties will be discussed.

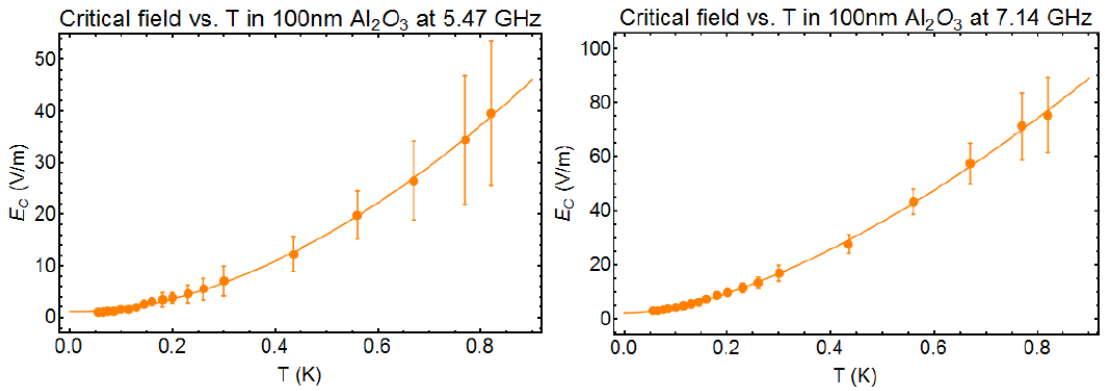

Figure 6.6: Critical electric field versus temperature in 100nm of aluminum oxide grown by atomic layer deposition determined by measurements of niobium interdigital resonators with resonance frequencies of 5.47 and 7.14 GHz. Values of the critical field are extracted by fitting voltage dependent loss data to equation (6.4), and fit to equation (6.8).

6.3 Results from all measured resonators

Here we summarize the results from all measured devices by presenting the results obtained by the methods outlined in the previous section.

6.3.1 Device W60-C4h: 30nm Al_2O_3

These measurements were made using niobium interdigital resonators at 5.42 and 7.08 GHz which have an ALD Al_2O_3 dielectric layer 30 nm in thickness.

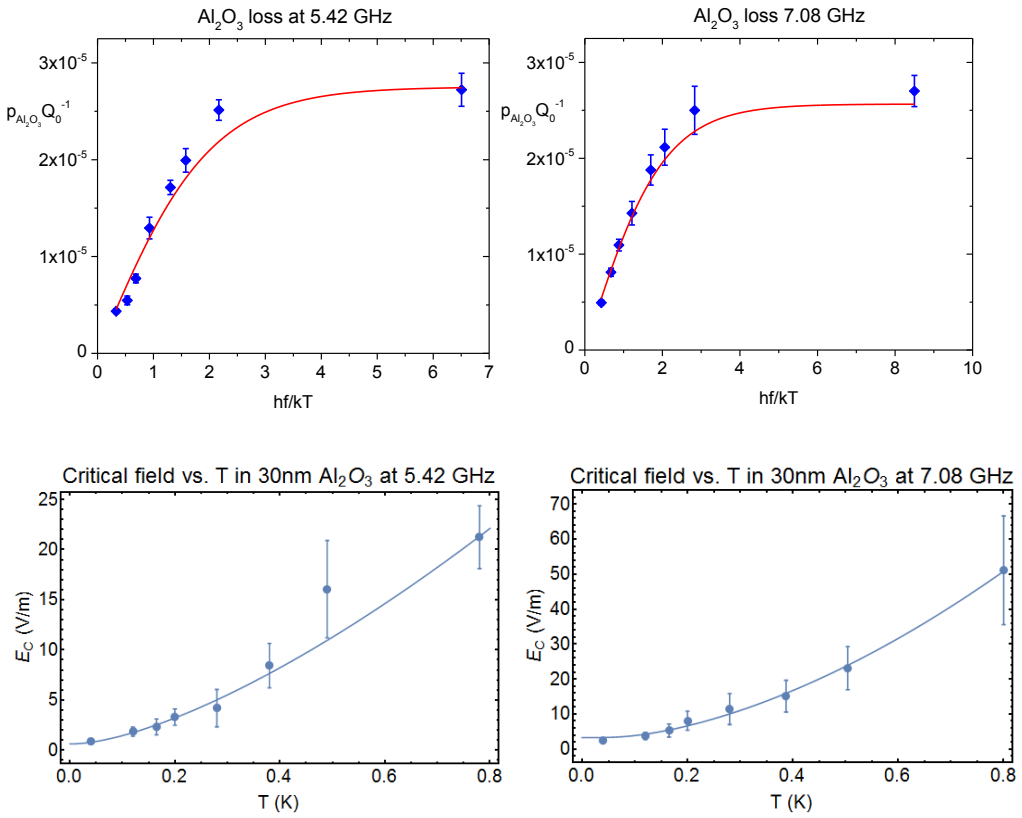

Figure 6.7: Measurements of Intrinsic loss (top) and critical field (bottom) in 30 nm ALD aluminum oxide using niobium interdigital resonators with frequencies of 5.42 and 7.08 GHz. The intrinsic loss is fit to equation (6.2) and the critical field is fit to equation (6.8).

Figure 6.7 shows the intrinsic loss measured in the two resonators and the temperature dependence of the critical field. The relevant fitting parameters are tabulated below in Table 6.6. We find good agreement with the TLS model and with the form of E_c given by equation (6.4).

Table 6.6: Fitting parameters for loss and critical field in 30nm Al_2O_3

f_r (GHz)	Q^{-1}_{0,Al_2O_3}	$\Gamma^0_{1,m}$ (kHz)	a (MHz/K$^\mu$)	μ
5.42	2.25×10^{-3}	24.7	3.74	1.93
7.08	1.98×10^{-3}	128	5.25	2.51

6.3.2 Device W60-C4f: 60nm Al_2O_3

These measurements were made using niobium interdigital resonators at 5.37 and 7.01 GHz which have an ALD Al_2O_3 dielectric layer 60 nm in thickness.

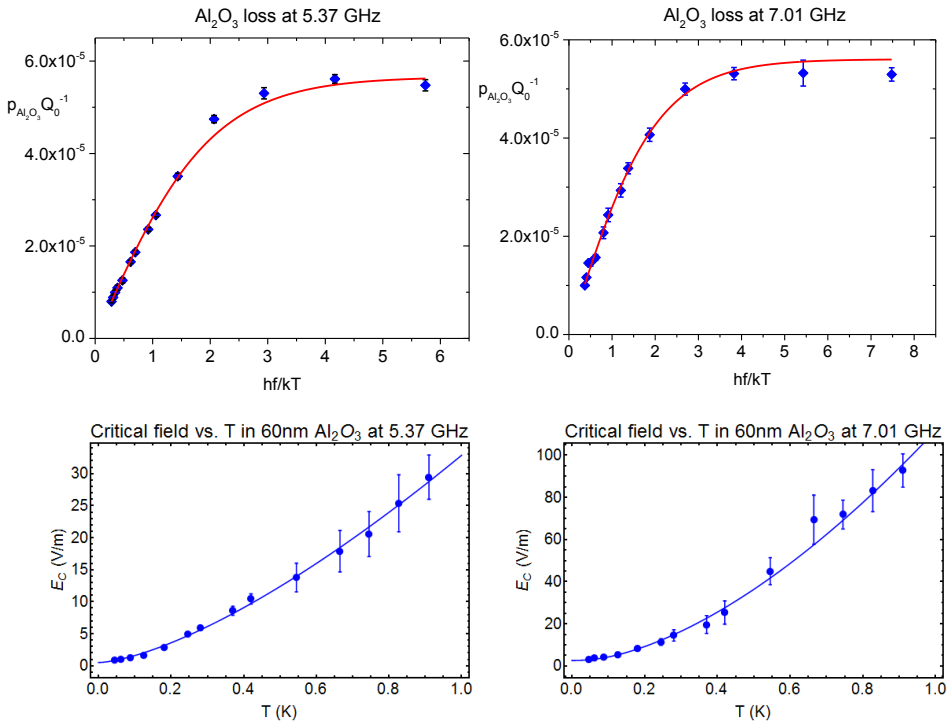

Figure 6.8: Measurements of Intrinsic loss (top) and critical field (bottom) in 60 nm ALD aluminum oxide using niobium interdigital resonators with frequencies of 5.37 and 7.01 GHz. The intrinsic loss is fit to equation (6.2) and the critical field is fit to equation (6.8).

Table 6.7: Fitting parameters for loss and critical field in 60nm Al_2O_3

f_r (GHz)	Q^{-1}_{0,Al_2O_3}	$\Gamma^0_{1,m}$ (kHz)	a (MHz/K$^\mu$)	μ
5.37	2.27×10^{-3}	20.1	5.33	1.86
7.01	2.24×10^{-3}	106	15.2	2.32

Figure 6.8 shows the intrinsic loss for measured in the two resonators and the temperature dependence of the critical field. The relevant fitting parameters are tabulated in Table 6.7. Again, we find good agreement with the TLS model and with the form of E_c given by equation (6.4).

Data for the resonance frequency as a function of temperature is presented below in Fig. 6.9 and the relevant fit parameters in Table 6.8. We find excellent agreement with the TLS model over the temperature range which was characterized.

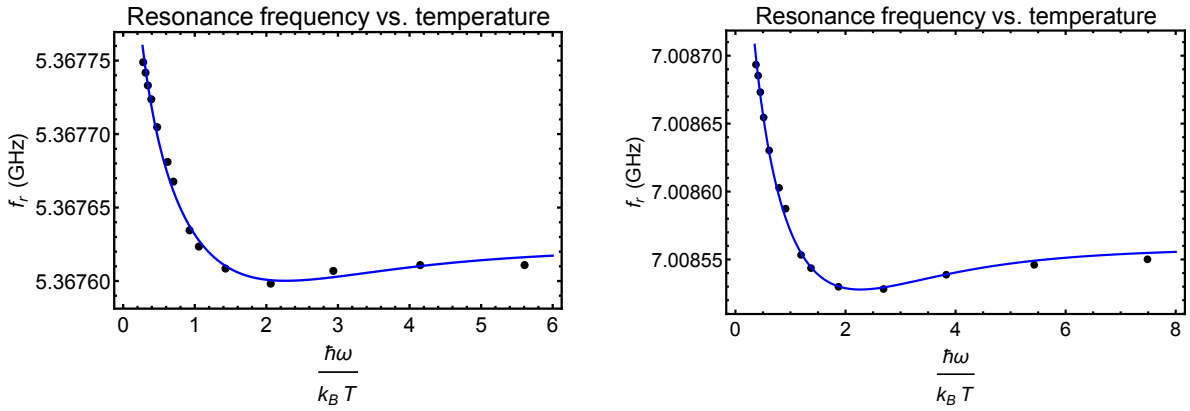

Figure 6.9: Resonance frequency versus temperature for two niobium interdigital resonators with 60 nm of ALD aluminum oxide at frequencies of 5.37 anf 7.01 GHz. The data points are fit to the prediction of the TLS model given by equation (6.5).

Table 6.8: Fitting parameters for temperature dependent frequency shift

Resonator	$f_r(T=0)$ (GHz)	Q_0^{-1}
LC1	5.36783	2.68×10^{-3}
LC2	7.00885	2.25×10^{-3}

6.3.3 Device W79-E4a: 100 nm Al_2O_3

The superconducting material of this device is aluminum. There are four resonators at 5.96, 7.15, 7.97 and 9.01 GHz with 100 nm of Al_2O_3.

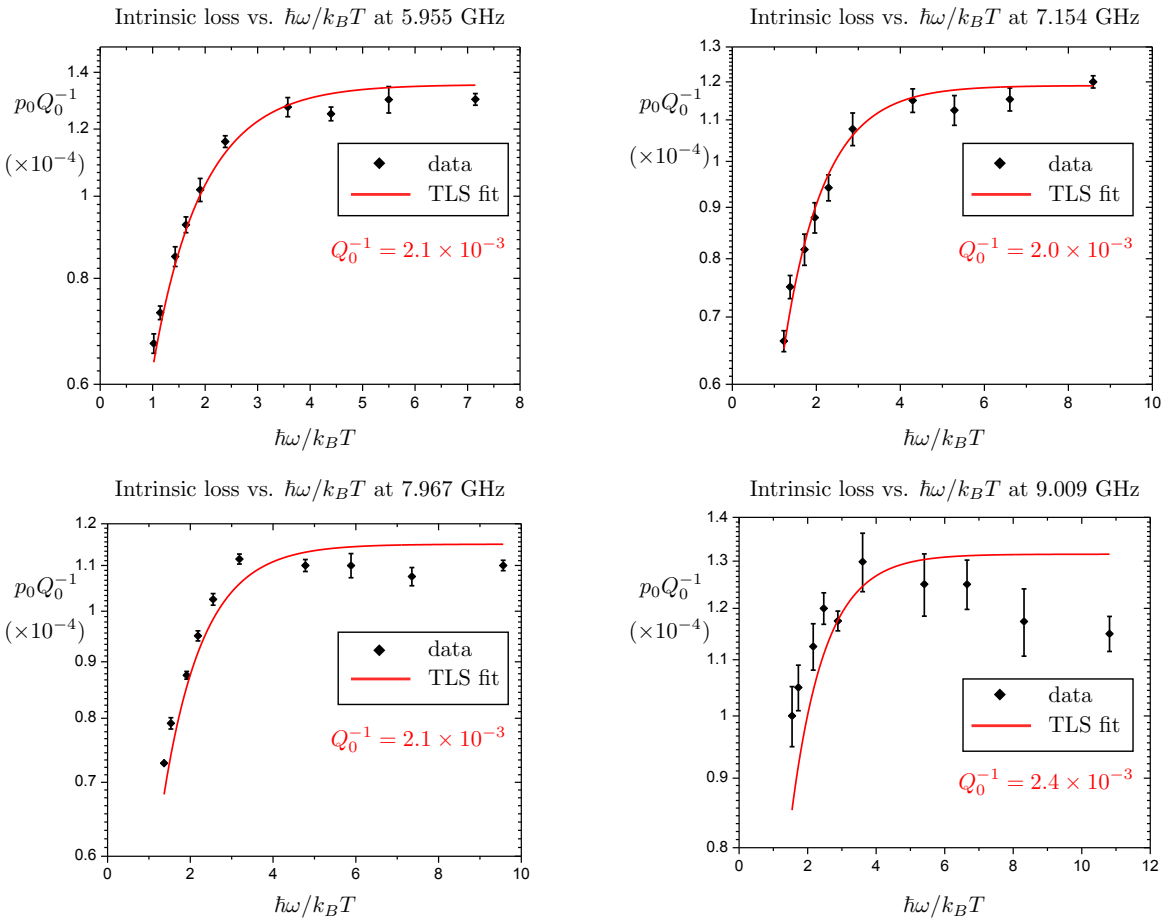

Figure 6.10: Plot of the intrinsic dielectric loss as a function of $\hbar\omega/k_BT$ obtained by fitting the loss vs voltage data to equation (5.4). The plots scale by the participation ratio, p_0, which in this case is slightly different for each resonator due to geometric variations in the capacitor. Taking this into account we find that $Q^{-1}_{0,Al_2O_3} = 2.15 \pm 0.17 \times 10^{-3}$.

The loss parameters obtained from fitting are given in Table 6.9. The critical field data determined from the voltage dependent loss is provided in Fig. 6.11 and the fitting parameters are presented in Table 6.10. The data of the temperature dependent frequency shift is given in Fig. 6.12.

Table 6.9: Fitting parameters for W79-E4a

Resonator	$f_r(T=0)$ (GHz)	Q_0^{-1}
LC1	5.95842	1.68×10^{-3}
LC2	7.15205	1.93×10^{-3}
LC3	7.96841	2.79×10^{-3}
LC4	9.02131	1.43×10^{-3}

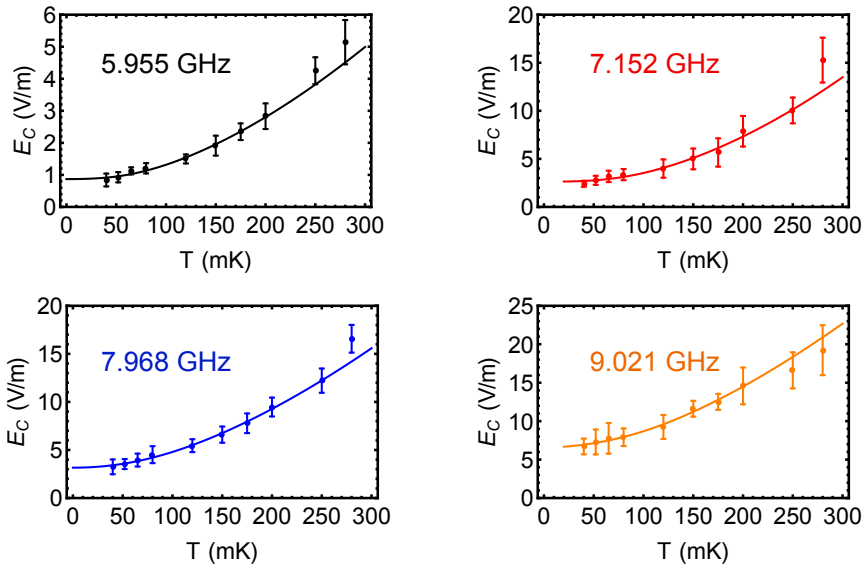

Figure 6.11: Critical electric field data in four aluminum interdigital resonators with various resonant frequencies. The superconducting material is aluminum so to reduce the effect of superconducting loss mechanisms data points for the critical field for $T < 200$ mK are fit to the model for E_c given by equation (6.8) where $\Gamma_\phi = aT^\mu$.

Table 6.10: Fitting parameters for the critical field in W79-E4a

Resonator	f_r (GHz)	$\Gamma^0_{1,m}$ (kHz)	a (MHz/K$^\mu$)	μ
LC1	5.955	34 ± 3 ± 2.5	3.68 ± 2.08	2.36
LC2	7.152	104 ± 10 ± 0.9	15.1 ± 8.06	2.67
LC3	7.968	125 ± 11 ± 0.1	9.60 ± 3.96	2.12
LC4	9.021	261 ± 16	7.81 ± 3.77	1.95

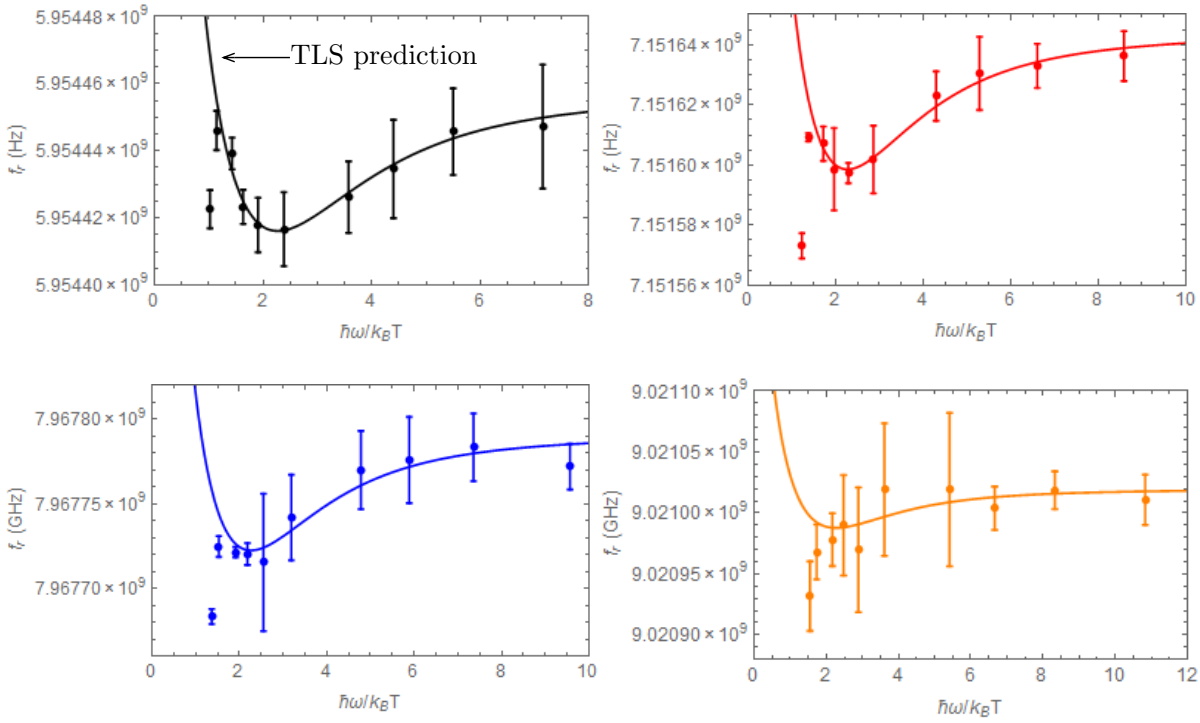

Figure 6.12: Plots of the frequency shift due to two-level systems as a function of temperature averaged at low microwave powers. The data is fit to equation (6.5) for temperatures > 200 mK because superconducting loss results in an increase in the kinetic inductance and causes the resonance frequency to decrease contrary to the TLS prediction. The error in the data points is the standard deviation in points which are averaged at low-power.

Measurements of the intrinsic loss tangent determined from the frequency shift in various

resonators do not show any systematic dependence on frequency. By averaging the extracted values of the intrinsic loss determined from the frequency shift we find that $Q^{-1}_{0,Al_2O_3} = 1.96 \pm 0.59 \times 10^{-3}$, in good agreement with the loss determined from direct low-power measurements of the unsaturated internal Q-factor.

6.3.4 Overlap Al/Nb resonators

We now present measurements of resonators which feature an overlap parallel plate capacitor where the dielectric material of interest is sandwiched between the plates. This makes the participation ratio of the loss tangent very close to unity since the electric field is totally confined within the lossy oxide between the capacitor plates, rather than distributed over other regions such as the substrate and free space. Despite the parallel plate geometry, the electric field inside the capacitor still experiences some inhomogeneity which is reflected in the voltage dependent loss measurements. This arises from the fact that the bottom metal layer of the device is niobium and therefore has some native oxide on its surface which formed during the fabrication process. The dielectric constant of niobium oxide (Nb_2O_5, the most abundant form of niobium oxide known to form under ambient conditions) is $\epsilon_r \sim 30$ compared to Al_2O_3 ($\epsilon_r \sim 8$), so the magnitude of the electric field in the resonator varies accordingly between these two volumes according to the continuity equation of electrodynamics. The top plate is necessarily made of aluminum, since a lift-off fabrication process for niobium had not been developed, but is possible in principle. In Fig. 6.13, we present data for two overlap capacitor resonators, with frequencies of 5.14 and 9.53 GHz. We find excellent agreement in the temperature dependence of the intrinsic loss with the prediction from TLS theory. Furthermore we find a strong temperature dependence in the critical electric field in agreement with measurements from other resonators. Table 6.11 below summarizes the fitting parameters and relevant physical quantities extracted for these resonators.

Table 6.11: Loss and critical field in 30nm Al_2O_3 extracted using overlap resonators

$f_r(T=0)$ (GHz)	Q^{-1}_{0,Al_2O_3}	$\Gamma^0_{1,m}$ (kHz)	a (MHz/K$^\mu$)	μ
5.144	2.49×10^{-3}	59.4	3.81	2.31
9.530	3.10×10^{-3}	324	22.4	2.00

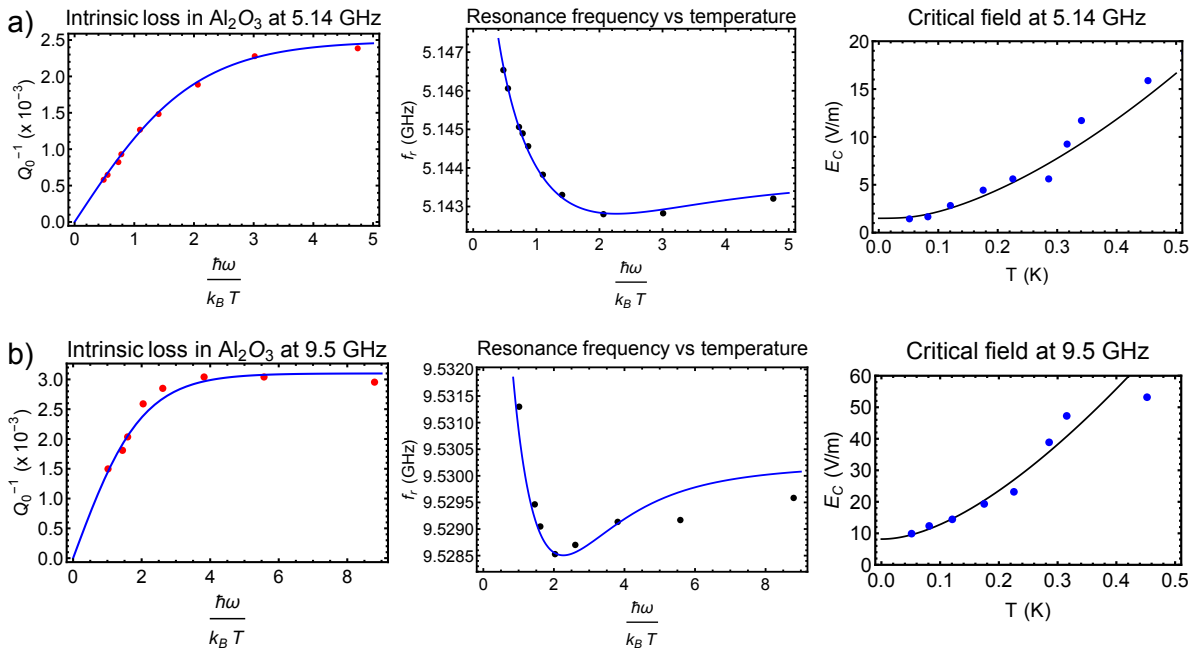

Figure 6.13: Temperature dependence of the intrinsic loss tangent (left), resonance frequency (middle) and critical field (right) for two superconducting resonators consisting of an overlap capacitor. The intrinsic loss and frequency shift are fit to the predictions of the TLS model given by equations (6.2) and (6.5) respectively, and the critical field is fit to equation (6.8) a) Temperature dependent data for a 5.14 GHz resonator. b) Temperature dependent data for 9.53 GHz resonator.

6.4 Discussion

We have presented an extensive set of measurements of temperature dependent dielectric loss in Al_2O_3 using superconducting microwave resonators. Here we discuss the results in a more general context by comparing our measurements with those from another type of aluminum oxide grown by plasma oxidation. We then discuss the measurements of the critical electric field which reflects the coherence of two-level system ensembles in the amorphous material. These measurements provide an important comparison to measurements which have measured coherence properties of a single two-level system using superconducting qubits [76, 50].

6.4.1 Intrinsic dielectric loss tangent

Table 6.12 shows the value of the loss tangent determined from each device by averaging the values determined from each resonator on a device. Using the average value of the intrinsic loss

Table 6.12: Summary of intrinsic dielectric loss tangent in Al_2O_3 grown by atomic layer deposition

Device	Type	Al_2O_3 thickness (nm)	Metal	Temperatures (mK)	$Q_0^{-1}(\times 10^{-3})$
W60-C4h	Interdigital	30	Nb	40 - 800	2.12 $\pm$0.19
W60-C4f	Interdigital	60	Nb	46 - 990	2.46 $\pm$0.24
W60-C5b	Interdigital	100	Nb	50 - 820	2.39 $\pm$0.35
W79-E4a	Interdigital	100	Al	40 - 280	1.96 $\pm$0.51
W60-A2d	Overlap	30	Al/Nb	50 - 590	2.80 $\pm$0.43
W60-B2h	Overlap	60	Al/Nb	47 - 180	2.45 $\pm$0.25

tangent Q_0^{-1} and its definition according to the TLS model (see section 2.3)

$$Q_0^{-1} = \frac{\pi (q d_0)^2 P_0}{3\epsilon_0 \epsilon_r}, \tag{6.10}$$

where qd_0 is the average TLS dipole moment, P_0 is the density of states per unit energy and volume, and $\epsilon_r = 8.5$ for ALD aluminum oxide, the number of TLS per unit volume at a given frequency can be calculated. Complementary experiments [53, 76, 44] on TLSs using single qubits have extracted a dipole size of $d_0 \simeq 0.1$ nm and a coupling energy of 1 eV, which is found to be consistent with an electron tunnelling roughly the distance of an atomic bond length in aluminum oxide. Using these results we assume the tunnelling of a single electron, over a distance of 0.1 nm,

and we calculate $P_0 = 6.6 \times 10^{38}$ J^{-1}cm^{-3}. Evaluating at an energy of 6 GHz gives 2.2×10^{15} TLS $\times$ cm^{-3} or about 2200 per μm^3. This number is consistent with other work on aluminum oxide [42, 52, 19, 62].

6.4.2 Comparison with plasma AlOx

We compare the behaviour of dielectric loss in ALD Al_2O_3 with another form of aluminum oxide grown by high-power plasma oxidation (PO) of aluminum [19]. This method is done in-situ following evaporation of aluminum and yields a thin layer of aluminum oxide approximately 5 nm thick. This type of oxide layer is very similar to the aluminum oxide layer in SIS Josephson junctions, as it is grown in a nearly identical manner. The temperature dependence of the loss is shown in Fig. 6.14. For this device, the intrinsic loss factor was determined to be $Q_0^{-1} = 2.0 \times 10^{-3}$, very similar to the value obtained for ALD aluminum oxide. However, in PO aluminum oxide, we find that the value of the critical field is roughly an order of magnitude larger ($E_c^{\mathrm{PO}} \simeq$ 40 V/m). While both materials are forms of aluminum oxide, spectroscopy measurements using X-ray photoelectron spectroscopy (XPS) revealed differences in the proportion of chemical species present in each material. XPS measurements revealed an Al-O ratio of 1.52 in the ALD film, while for the PO film it was found to be 1.69. Further measurements also indicated that each material has carbon impurity defects. When bound to oxygen, the O-C ratio is 1.39 for the ALD film and 1.45 for the PO film. It is very interesting that differences in both stoichiometry and impurity content do not significantly affect the properties of the loss, yet, the saturation characteristics of the two-level systems are clearly different. This would suggest that the chemical differences play a role in mediating relaxation and dephasing mechanisms of TLSs in amorphous solids, but not necessarily in defining their intrinsic density of states. Further experiments which systematically address chemical differences between different types of films would provide further insight into this result.

Some have attributed the origin of two-level systems in amorphous aluminum oxide as hydrogen tunnelling defects [42], however we do not find the presence of OH (hydroxide) to be abundant in our samples. From this comparison and chemical analysis, it is difficult to correlate two-level systems with a particular type of chemical defect in the material. It is more plausible to view their existence as a natural consequence of microscopic disorder, which chemical defects may contribute to.

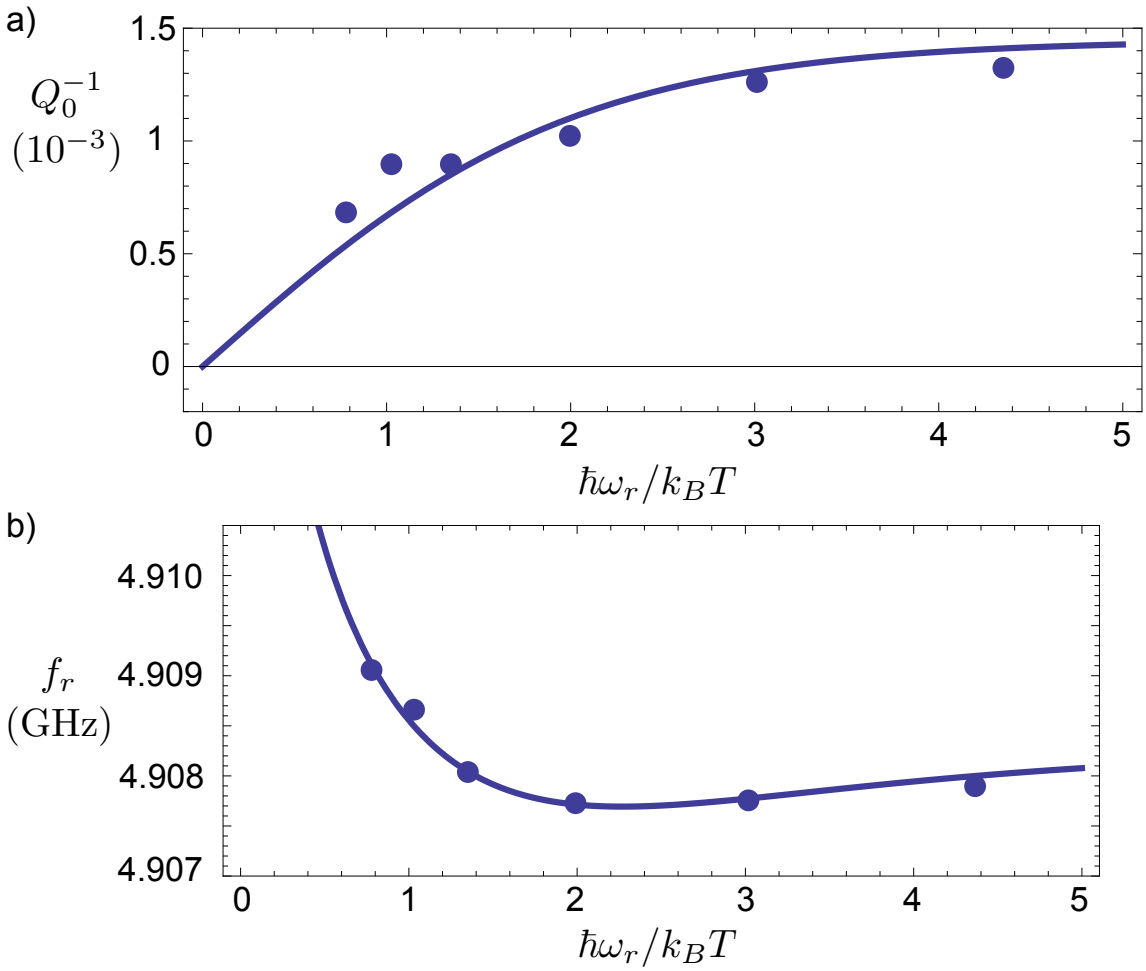

Figure 6.14: Temperature dependent loss data from reference [19]. Resonator is fabricated entirely from aluminum and is measured from 54 mK to 300 mK. The solid lines are the fits to the TLS model. a) Intrinsic loss tangent determined from direct measurements of the internal quality factor of an overlap capacitor resonator containing a 5 nm AlO_x film grown by plasma oxidation. b) Temperature dependence of the resonance frequency.

6.4.3 Temperature dependence of the critical saturation field

The measurements presented for the critical saturation field, E_c, demonstrate a strong temperature dependence in all measured devices (see Fig. 6.15). In particular we find that, in order to account for this, the coherence of the TLS cannot be limited by relaxation, i.e., $T_2 \neq 2T_1$, which has been reported in some cases for experiments on single TLSs using phase qubits [76, 50]. Our measurements differ from these fundamentally since they pertain to an ensemble averaged quantity of TLSs which are resonant with the microwave field in the resonator. They also have the added merit that a temperature range much larger than that which is accessible for qubit may be characterized. The theory of spectral diffusion [10, 45, 33], suggests that a temperature dependence of $T_\phi^{-1} \propto T^2$ arises from energy fluctuations of thermal two-level systems undergoing random transitions induced by their interaction with thermal phonons. The fluctuations of the thermal TLSs produce small energy changes in the local strain field which have the effect of shifting the energy of the TLS which are resonant with the microwave field. Over time, the energy uncertainty of the resonant two-level systems will increase as a result of the induced dephasing. In general, dephasing could be the result of other processes, but no evidence in literature has suggested mechanisms which arise independently of a mutual interaction.

We find consistently that both T_1 and T_2 are larger than the values measured using qubits. We find T_1 ranges from 3 to 40 μs and T_ϕ varies from 3 to 30 μs at the lowest measured temperatures. In the qubit experiments, the TLSs in the Josephson junctions are found to have 10 ns $< T_1 <$ 6 μs, $T_2 \sim$ 100 ns and 100 ns $< T_\phi <$ 3 μs [76, 50]. This difference between qubit measurements is quite intriguing. Despite the fact that both materials are aluminum oxide, the environment of the TLS could be quite different because of the small size and thickness of the oxide layer in the junctions. The discrete nature of the TLSs measured in qubit experiments makes the role of the mutual interaction more difficult to intepret. Certain TLSs could be subject a different degrees of relaxation and dephasing processes depending on their specific positions inside the junction [76]. In our experiments, we see less of a spread in the TLS properties as a result of measuring the ensemble. Among the different oxide thicknesses which were considered in this work, we find no systematic dependence on thickness which has been proposed recently [22].

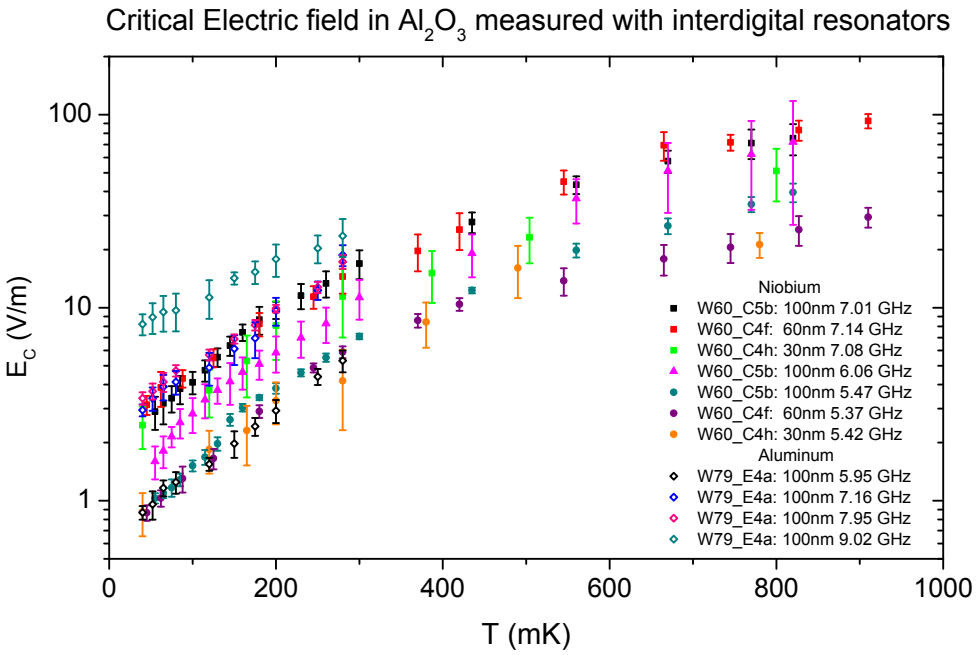

Figure 6.15: Summary of critical field measurements in various interdigital resonators. For niobium resonators, the measurements were made up to ~ 1 K, and for aluminum resonators, up to ~ 300 mK.

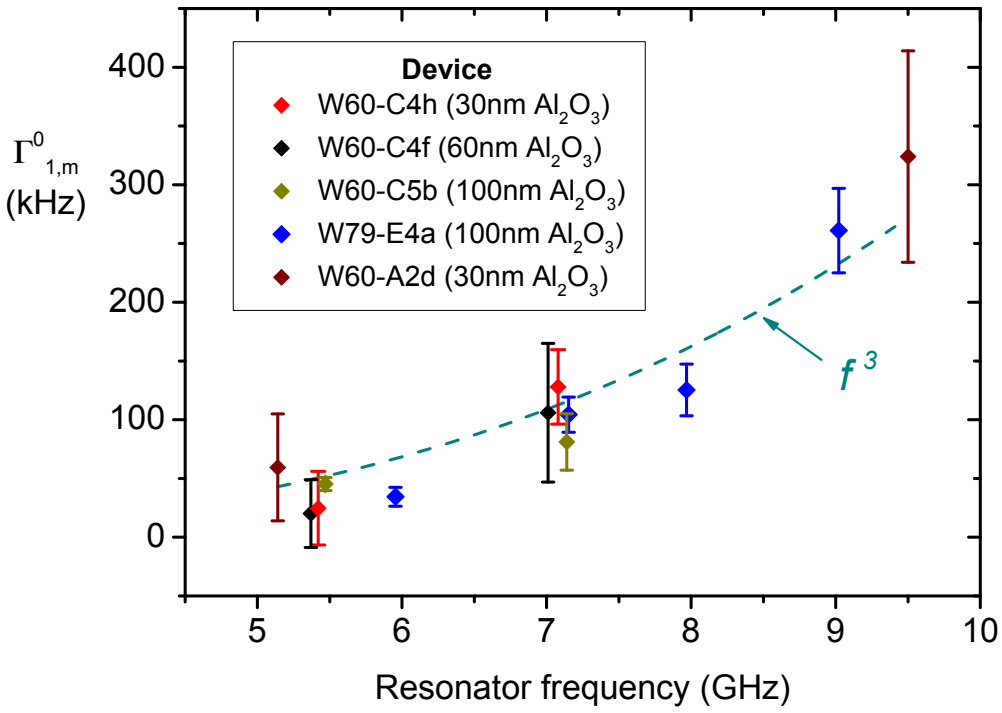

Figure 6.16: Summary of the zero-temperature intrinsic relaxation rate $\Gamma^0_{1,m}$ as a function of resonator frequency obtained from fitting the temperature dependence of the critical electric field. Data is fit to the prediction for the TLS model given by equation (6.9).

6.4.4 Frequency dependence of the intrinsic relaxation rate

The TLS model predicts that the maximum intrinsic relaxation rate of the TLS via phonons is given by equation (6.9). We find good agreement with this prediction and our results are the first to demonstrate this using superconducting resonators. Measurements across a larger frequency band and at lower temperatures would provide a better test of this prediction. By fitting the critical field data as a function of temperature to equation (6.8), we extract the value of $\Gamma^0_{1,m}$, the average intrinsic relaxation rate of the TLSs.

By using the results from resonators at different frequencies we plot the value of $\Gamma^0_{1,m}$ as a function of frequency in Fig. 6.16. We find that the data can be fit to a $\Gamma^0_{1,m} = a \times f^3$ without a constant offset term in agreement with equation (6.9). This re-affirms our agreement with the TLS model and is further evidence that T_1 is due to phonon relaxation.

6.4.5 Conclusions

In this chapter, we have presented detailed measurements of dielectric loss in aluminum oxide grown by atomic layer deposition. The intrinsic loss tangent, extracted directly from measurements of the internal quality factor and shift in resonance frequency, shows excellent agreement with the two-level system model over a large temperature range. We find the intrinsic loss tangent to be $Q_0^{-1} = 2.3 \times 10^{-3}$. This value is very similar to that obtained for aluminum oxide grown by plasma oxidation, which has different stoichiometry and chemical impurity content. This similarity suggests that TLS arise microscopically due to the amorphous structure at low temperatures and their density of states is not strongly affected by chemical defects.

Using a robust analysis method for a resonator with an inhomogeneous electric field, we presented measurements of the critical saturation field. These measurements provide information on the coherence properties of the TLS ensembles in an amorphous material over a temperature which is not achievable with single-TLS measurements using qubits. We characterized the temperature dependence of the critical electric field in amorphous Al_2O_3 using different types of superconducting resonators with frequencies in the range of 5-10 GHz. We find consistently that the data requires a strongly temperature dependent dephasing term $\Gamma_\phi (\sim T^2)$ where the exponent agrees roughly with the prediction from the theory of spectral diffusion. Our ensemble average measurements are therefore suggestive of a strong temperature-dependent dephasing process experienced by the TLSs which supports the presence of a mutual interaction between two-level systems in the amorphous material. Figure 6.15 shows the critical electric field data in all the interdigital resonators considered in this study. We find the frequency dependence of the intrinsic phonon relaxation to be in good agreement with the prediction of the TLS model. Our measurements indicate that the two-level systems experience a strong temperature dependent dephasing process which is suggestive of a strong mutual interaction. The temperature dependence can be accounted for by the theory of spectral diffusion in glasses, and our experimental results present the first evidence for this obtained from an ensemble measurement.

References

[1] Oxford instruments: Atomic layer deposition, 2010.

[2] Ansys electromagnetics inc. hfss 15.0, 2013.

[3] Commercial program comsol multiphysics 4.3b., 2013.

[4] Sonnet users manual release 13.54. liverpool, ny: Sonnet software, inc., 2013, 2013.

[5] P. W. Anderson, B. Halperin, and C. M. Varma. Anomalous low-temperature thermal properties of glasses and spin glasses. *Philosophical Magazine*, 25(1):1–9, 1972.

[6] J. Bardeen, L. Cooper, and J. Schrieffer. Theory of superconductivity. *Phys. Rev.*, 108:1175–1204, Dec 1957.

[7] R. Barends, H. L. Hortensius, T. Zijlstra, J. J. A. Baselmans, S. J. C. Yates, J. R. Gao, and T. M. Klapwijk. Contribution of dielectrics to frequency and noise of nbtin superconducting resonators. *Applied Physics Letters*, 92(22):–, 2008.

[8] R. Barends, J. Wenner, M. Lenander, Y. Chen, R. Bialczak, J. Kelly, E. Lucero, P. OMalley, M. Mariantoni, D. Sank, et al. Minimizing quasiparticle generation from stray infrared light in superconducting quantum circuits. *Applied Physics Letters*, 99(11):113507, 2011.

[9] M. A. Biondi and M. P. Garfunkel. Millimeter wave absorption in superconducting aluminum. i. temperature dependence of the energy gap. *Phys. Rev.*, 116:853–861, Nov 1959.

[10] J. Black and B. Halperin. Spectral diffusion, phonon echoes, and saturation recovery in glasses at low temperatures. *Phys. Rev. B*, 16:2879–2895, Sep 1977.

[11] A. Blais, J. Gambetta, A. Wallraff, D. Schuster, S. Girvin, M. Devoret, and R. Schoelkopf. Quantum-information processing with circuit quantum electrodynamics. *Physical Review A*, 75(3):032329, 2007.

[12] A. Blais, R.-S. Huang, A. Wallraff, S. Girvin, and R. J. Schoelkopf. Cavity quantum electrodynamics for superconducting electrical circuits: An architecture for quantum computation. *Physical Review A*, 69(6):062320, 2004.

[13] F. Bloch, W. Hansen, and M. Packard. Physical review. *Phys Rev*, 70:460–473, 1946.

[14] J. Burnett, T. Lindström, M. Oxborrow, Y. Harada, Y. Sekine, P. Meeson, and A. Y. Tzalenchuk. Slow noise processes in superconducting resonators. *Phys. Rev. B*, 87:140501, Apr 2013.

[15] G. Ciovati, G. Myneni, F. Stevie, P. Maheshwari, and D. Griffis. High field q slope and the baking effect: Review of recent experimental results and new data on nb heat treatments. *Phys. Rev. ST Accel. Beams*, 13:022002, Feb 2010.

[16] D. Cousins, S. Fisher, A. Gunault, R. Haley, I. Miller, G. Pickett, G. Plenderleith, P. Skyba, P. Thibault, and M. Ward. An advanced dilution refrigerator designed for the new lancaster microkelvin facility. *Journal of Low Temperature Physics*, 114(5-6):547–570, 1999.

[17] P. De Visser, J. Baselmans, J. Bueno, N. Llombart, and T. Klapwijk. Fluctuations in the electron system of a superconductor exposed to a photon flux. *Nature communications*, 5, 2014.

[18] C. Deng, M. Otto, and A. Lupascu. An analysis method for transmission measurements of superconducting resonators with applications to quantum-regime dielectric-loss measurements. *Journal of Applied Physics*, 114(5):054504, 2013.

[19] C. Deng, M. Otto, and A. Lupascu. Characterization of low-temperature microwave loss of thin aluminum oxide formed by plasma oxidation. *Applied Physics Letters*, 104(4):–, 2014.

[20] M. H. Devoret and R. J. Schoelkopf. Superconducting circuits for quantum information: An outlook. *Science*, 339(6124):1169–1174, 2013.

[21] C. Enss and S. Hunklinger. Tunneling systems. In *Low-Temperature Physics*, pages 283–341. Springer Berlin Heidelberg, 2005.

[22] L. Faoro and L. B. Ioffe. Generalized tunneling model for tls in amorphous materials and its predictions for their dephasing and the noise in superconducting microresonators. *arXiv preprint arXiv:1404.2410*, 2014.

[23] P. Forn-Díaz. *Superconducting Qubits and Quantum Resonators*. TU Delft, Delft University of Technology, 2010.

[24] J. Gao. *The physics of superconducting microwave resonators*. PhD thesis, California Institute of Technology, 2008.

[25] J. Gao, M. Daal, A. Vayonakis, S. Kumar, J. Zmuidzinas, B. Sadoulet, B. A. Mazin, P. K. Day, and H. G. Leduc. Experimental evidence for a surface distribution of two-level systems in superconducting lithographed microwave resonators. *Appl. Phys. Lett.*, 92(15):152505, January 2008.

[26] K. Geerlings, S. Shankar, E. Edwards, L. Frunzio, R. J. Schoelkopf, and M. H. Devoret. Improving the quality factor of microwave compact resonators by optimizing their geometrical parameters. *Applied Physics Letters*, 100(19):192601, 2012.

[27] S. M. George. Atomic layer deposition: an overview. *Chemical reviews*, 110(1):111–131, 2009.

[28] B. Golding, J. Graebner, B. Halperin, and R. Schutz. Nonlinear phonon propagation in fused silica below 1 k. *Phys. Rev. Lett.*, 30:223–226, Feb 1973.

[29] B. Golding and J. E. Graebner. Phonon echoes in glass. *Physical Review Letters*, 37(13):852, 1976.

[30] B. Golding and J. E. Graebner. Echo phenomena in disordered solids. In *Phonon Scattering in Condensed Matter*, pages 11–20. Springer, 1980.

[31] M. Goppl, A. Fragner, M. Baur, R. Bianchetti, S. Filipp, J. M. Fink, P. J. Leek, G. Puebla, L. Steffen, and A. Wallraff. Coplanar waveguide resonators for circuit quantum electrodynamics. *Journal of Applied Physics*, 104(11):–, 2008.

[32] M. Grundner and J. Halbritter. On the natural nb2o5 growth on nb at room temperature. *Surface Science*, 136(1):144 – 154, 1984.

[33] P. Hu and L. Walker. Spectral-diffusion decay in echo experiments. *Phys. Rev. B*, 18:1300–1305, Aug 1978.

[34] S. Hunklinger. *Physical Acoustics*, volume 12. New York Academic Press, 1976.

[35] S. Hunklinger. Acoustic and dielectric properties of glasses at low temperatures. In J. Treusch, editor, *Festkrperprobleme 17*, volume 17 of *Advances in Solid State Physics*, pages 1–11. Springer Berlin Heidelberg, 1977.

[36] S. Hunklinger, W. Arnold, R. Nava, K. Dransfeld, et al. Saturation of the ultrasonic absorption in vitreous silica at low temperatures. *Physics letters A*, 42(3):253–255, 1972.

[37] J. Jäckle. On the ultrasonic attenuation in glasses at low temperatures. *Zeitschrift für Physik*, 257(3):212–223, 1972.

[38] R. Jaklevic, J. Lambe, A. Silver, and J. Mercereau. Quantum interference effects in josephson tunneling. *Phys. Rev. Lett.*, 12:159–160, Feb 1964.

[39] E. Jaynes and F. Cummings. Comparison of quantum and semiclassical radiation theories with application to the beam maser. *Proceedings of the IEEE*, 51(1):89–109, Jan 1963.

[40] J. Joffrin and A. Levelut. Virtual phonon exchange in glasses. *Journal de Physique*, 36(9):811–822, 1975.

[41] B. Josephson. Possible new effects in superconductive tunnelling. *Physics Letters*, 1(7):251 – 253, 1962.

[42] M. Khalil, M. Stoutimore, S. Gladchenko, A. Holder, C. Musgrave, A. Kozen, G. Rubloff, Y. Liu, R. Gordon, J. Yum, S. Banerjee, C. Lobb, and K. Osborn. Evidence for hydrogen two-level systems in atomic layer deposition oxides. *Applied Physics Letters*, 103(16):162601–162601–4, Oct 2013.

[43] M. S. Khalil, F. Wellstood, and K. D. Osborn. Loss dependence on geometry and applied power in superconducting coplanar resonators. *Applied Superconductivity, IEEE Transactions on*, 21(3):879–882, 2011.

[44] L.-C. Ku and C. C. Yu. Decoherence of a josephson qubit due to coupling to two-level systems. *Phys. Rev. B*, 72:024526, Jul 2005.

[45] B. Laikhtman. General theory of spectral diffusion and echo decay in glasses. *Phys. Rev. B*, 31:490–504, Jan 1985.

[46] L. D. Landau and V. Ginzburg. On the theory of superconductivity. *Zh. Eksp. Teor. Fiz.*, 20:1064, 1950.

[47] L. D. Landau, L. D. Landau, L. D. Landau, E. M. Lifshitz, and E. M. Lifšic. *Course of theoretical physics: quantum mechanics*. Butterworth-Heinemann, 2000.

[48] A. J. Leggett and D. C. Vural. tunneling two-level systems model of the low-temperature properties of glasses: Are smoking-gun tests possible? *The Journal of Physical Chemistry B*, 117(42):12966–12971, 2013.

[49] T. Lindström, J. E. Healey, M. S. Colclough, C. M. Muirhead, and A. Y. Tzalenchuk. Properties of superconducting planar resonators at millikelvin temperatures. *Phys. Rev. B*, 80:132501, Oct 2009.

[50] J. Lisenfeld, C. Müller, J. H. Cole, P. Bushev, A. Lukashenko, A. Shnirman, and A. V. Ustinov. Measuring the temperature dependence of individual two-level systems by direct coherent control. *Phys. Rev. Lett.*, 105:230504, Dec 2010.

[51] F. London and H. London. The electromagnetic equations of the supraconductor. *Proceedings of the Royal Society of London A: Mathematical, Physical and Engineering Sciences*, 149(866):71–88, 1935.

[52] P. Macha, S. H. W. van der Ploeg, G. Oelsner, E. Ilichev, H.-G. Meyer, S. Wnsch, and M. Siegel. Losses in coplanar waveguide resonators at millikelvin temperatures. *Applied Physics Letters*, 96(6):–, 2010.

[53] J. M. Martinis, K. B. Cooper, R. McDermott, M. Steffen, M. Ansmann, K. D. Osborn, K. Cicak, S. Oh, D. P. Pappas, R. W. Simmonds, and C. C. Yu. Decoherence in josephson qubits from dielectric loss. *Phys. Rev. Lett.*, 95:210503, Nov 2005.

[54] A. Megrant, C. Neill, R. Barends, B. Chiaro, Y. Chen, L. Feigl, J. Kelly, E. Lucero, M. Mariantoni, P. J. J. O'Malley, D. Sank, A. Vainsencher, J. Wenner, T. C. White, Y. Yin, J. Zhao, C. J. P. m, J. M. Martinis, and A. N. Cleland. Planar superconducting resonators with internal quality factors above one million. *Applied Physics Letters*, 100(11):113510, 2012.

[55] M. Morita, T. Ohmi, E. Hasegawa, M. Kawakami, and M. Ohwada. Growth of native oxide on a silicon surface. *Journal of Applied Physics*, 68(3), 1990.

[56] S. Oh, K. Cicak, J. Kline, M. Sillanpää, K. Osborn, J. Whittaker, R. Simmonds, and D. Pappas. Elimination of two level fluctuators in superconducting quantum bits by an epitaxial tunnel barrier. *Phys. Rev. B*, 74:100502, Sep 2006.

[57] F. R. Ong, J.-L. Orgiazzi, A. de Waard, G. Frossati, and A. Lupascu. Insertable system for fast turnaround time microwave experiments in a dilution refrigerator. *Review of Scientific Instruments*, 83(9):–, 2012.

[58] A. D. OConnell, M. Ansmann, R. Bialczak, M. Hofheinz, N. Katz, E. Lucero, C. McKenney, M. Neeley, H. Wang, E. Weig, et al. Microwave dielectric loss at single photon energies and millikelvin temperatures. *Applied Physics Letters*, 92(11):112903, 2008.

[59] H. Paik and K. Osborn. Reducing quantum-regime dielectric loss of silicon nitride for superconducting quantum circuits. *Appl. Phys. Lett.*, 96(7):072505, January 2010.

[60] H. Paik, D. Schuster, L. Bishop, G. Kirchmair, G. Catelani, A. Sears, B. Johnson, M. Reagor, L. Frunzio, L. Glazman, S. Girvin, M. Devoret, and R. J. Schoelkopf. Observation of high coherence in josephson junction qubits measured in a three-dimensional circuit qed architecture. *Phys. Rev. Lett.*, 107:240501, Dec 2011.

[61] D. P. Pappas, M. R. Vissers, D. S. Wisbey, J. S. Kline, and J. Gao. Two level system loss in superconducting microwave resonators. *Applied Superconductivity, IEEE Transactions on*, 21(3):871–874, 2011.

[62] D. P. Pappas, M. R. Vissers, D. S. Wisbey, J. S. Kline, and J. Gao. Two level system loss in superconducting microwave resonators. *Applied Superconductivity, IEEE Transactions on*, 21(3):871–874, 2011.

[63] W. Phillips. Tunneling states in amorphous solids. *Journal of Low Temperature Physics*, 7(3-4):351–360, 1972.

[64] W. Phillips, A. Anderson, B. Golding, J. Graebner, S. Hunklinger, J. Jäckle, R. Pohl, v. Schickfus, and D. Weaire. *Amorphous Solids: Low-Temperature Properties*. Topics in Current Physics. Springer London, Limited, 2011.

[65] W. A. Phillips. Two-level states in glasses. *Reports on Progress in Physics*, 50(12):1657, 1987.

[66] L. Piché, R. Maynard, S. Hunklinger, and J. Jäckle. Anomalous sound velocity in vitreous silica at very low temperatures. *Phys. Rev. Lett.*, 32:1426–1429, Jun 1974.

[67] R. O. Pohl, X. Liu, and E. Thompson. Low-temperature thermal conductivity and acoustic attenuation in amorphous solids. *Rev. Mod. Phys.*, 74:991–1013, Oct 2002.

[68] D. Pozar. *Microwave Engineering*. Wiley, 2004.

[69] M. Reagor, H. Paik, G. Catelani, L. Sun, C. Axline, E. Holland, I. M. Pop, N. A. Masluk, T. Brecht, L. Frunzio, M. H. Devoret, L. Glazman, and R. J. Schoelkopf. Reaching 10ms single photon lifetimes for superconducting aluminum cavities. *Applied Physics Letters*, 102(19):–, 2013.

[70] J. M. Sage, V. Bolkhovsky, W. D. Oliver, B. Turek, and P. B. Welander. Study of loss in superconducting coplanar waveguide resonators. *Journal of Applied Physics*, 109(6):063915, 2011.

[71] J. J. Sakurai and J. Napolitano. *Modern quantum mechanics*. Addison-Wesley, 2011.

[72] M. Sandberg, M. R. Vissers, J. S. Kline, M. Weides, J. Gao, D. S. Wisbey, and D. P. Pappas. Etch induced microwave losses in titanium nitride superconducting resonators. *Applied Physics Letters*, 100(26):262605, 2012.

[73] M. V. Schickfus and S. Hunklinger. Saturation of the dielectric absorption of vitreous silica at low temperatures. *Physics Letters A*, 64(1):144 – 146, 1977. -.

[74] J. Schlaerth, A. Vayonakis, P. Day, J. Glenn, J. Gao, S. Golwala, S. Kumar, H. LeDuc, B. Mazin, J. Vaillancourt, et al. A millimeter and submillimeter kinetic inductance detector camera. *Journal of Low Temperature Physics*, 151(3-4):684–689, 2008.

[75] S. Schmidt and J. Koch. Circuit qed lattices: towards quantum simulation with superconducting circuits. *Annalen der Physik*, 525(6):395–412, 2013.

[76] Y. Shalibo, Y. Rofe, D. Shwa, F. Zeides, M. Neeley, J. M. Martinis, and N. Katz. Lifetime and coherence of two-level defects in a josephson junction. *Phys. Rev. Lett.*, 105:177001, Oct 2010.

[77] R. W. Simmonds, K. M. Lang, D. A. Hite, S. Nam, D. P. Pappas, and J. M. Martinis. Decoherence in josephson phase qubits from junction resonators. *Phys. Rev. Lett.*, 93:077003, Aug 2004.

[78] E. A. Tholen, A. Ergül, E. M. Doherty, F. M. Weber, F. Grégis, and D. B. Haviland. Nonlinearities and parametric amplification in superconducting coplanar waveguide resonators. *Applied physics letters*, 90(25):253509, 2007.

[79] P. Townsend and J. Sutton. Investigation by electron tunneling of the superconducting energy gaps in nb, ta, sn, and pb. *Phys. Rev.*, 128:591–595, Oct 1962.

[80] D. C. Vural and A. J. Leggett. Universal sound absorption in amorphous solids: A theory of elastically coupled generic blocks. *Journal of Non-Crystalline Solids*, 357(1920):3528 – 3537, 2011. -.

[81] A. Wallraff, D. I. Schuster, A. Blais, L. Frunzio, R.-S. Huang, J. Majer, S. Kumar, S. M. Girvin, and R. J. Schoelkopf. Strong coupling of a single photon to a superconducting qubit using circuit quantum electrodynamics. *Nature*, 431(7005):162–167, 2004.

[82] H. Wang, M. Hofheinz, J. Wenner, M. Ansmann, R. C. Bialczak, M. Lenander, E. Lucero, M. Neeley, A. D. OConnell, D. Sank, M. Weides, A. N. Cleland, and J. M. Martinis. Improving the coherence time of superconducting coplanar resonators. *Applied Physics Letters*, 95(23):–, 2009.

[83] S. Weinreb. Cryogenic performance of microwave terminations, attenuators, absorbers and coaxial cable. *NRAO Electronics Division Internal Report*, (223), 1982.

[84] J. Wenner, R. Barends, R. C. Bialczak, Y. Chen, J. Kelly, E. Lucero, M. Mariantoni, A. Megrant, P. J. J. OMalley, D. Sank, A. Vainsencher, H. Wang, T. C. White, Y. Yin, J. Zhao, A. N. Cleland, and J. M. Martinis. Surface loss simulations of superconducting coplanar waveguide resonators. *Applied Physics Letters*, 99(11):–, 2011.

[85] I. Wolfram Research. Mathematica.

[86] C.-J. Wu and T.-Y. Tseng. Microwave surface impedances of bcs superconducting thin films. *Applied Superconductivity, IEEE Transactions on*, 6(2):94–101, June 1996.

[87] R. Zeller and R. Pohl. Thermal conductivity and specific heat of noncrystalline solids. *Phys. Rev. B*, 4:2029–2041, Sep 1971.

[88] J. Zmuidzinas. Superconducting microresonators: Physics and applications. *Annual Review of Condensed Matter Physics*, 3(1):169–214, 2012.